Radiator Inlet Grille Modeling for Motorsport Applications

Master Thesis Aerospace Engineering

Filippo Cerbino

Delft University of Technology

TU Delft

Radiator Inlet Grille Modeling for Motorsport Applications

by

Filippo Cerbino

to obtain the degree of Master of Science

at the Delft University of Technology

Thesis Supervisors:	Dr.ir. A.H. van Zuijlen,	TU Delft
	Ing. A. Bongiovanni	Dallara
Project Duration:	June, 2025 - January, 2026	
Place:	Faculty of Aerospace Engineering, Delft	
	Dallara, Varano de Melegari (PR)	

TU Delft

Preface

This thesis represents the culmination of an intense, demanding, and very rewarding journey that would not have been possible without the guidance, support, and patience of many people. I am extremely grateful to Dallara for the opportunity to complete my Master's thesis in the world of motorsport, a field I have dreamed of working in since I was young. The central role of the company in top-tier competitions gave me a real taste of elite motorsport engineering.

First, and foremost, I express my deepest gratitude to my supervisor at Dallara, Andrea Bongiovanni, for sharing his expertise in motorsport aerodynamics and for the countless hours of technical discussions, feedback, and belief in my work, which have been crucial to the success of this research.

I am equally thankful to my academic supervisor at TU Delft, Dr. ir. Alexander van Zuijlen, for the unwavering support and consistent feedback that made this work academically solid.

Thanks also to the entire team at Dallara for the resources, facilities, and support I received throughout the simulation and experimental testing phases of the research.

To my friends, the ones who spent countless hours with me at university grinding through deadlines, and surviving the stressful, chaotic, rainy life in Delft, and all the others scattered around the world who still sent support even from thousands of kilometers away, thank you.

Finally, a huge gratitude to my family, for your unconditional support and patience through every doubt and decision made, which meant to me more than words can say.

Filippo Cerbino
Varano de Melegari (PR), January 2026

Abstract

In high-performance motorsport, the thermal management system is a critical component for ensuring optimal operating conditions of the vehicles. The system is vulnerable to the debris encountered on track; for this reason, protective grilles are commonly installed ahead of the radiator and other heat exchangers. However, those introduce static pressure losses due to their aerodynamic blockage effect. Accurate and cost-effective modeling of the grille effect is crucial to ensure enough cooling is provided while maximizing the aerodynamic performance.

The proposed objectives of this research project are to first identify the main pressure drop drivers and then find an accurate and cost-effective numerical model allowing for the simulation of any arbitrary grille geometry. The impact of the grille location and geometrical construction on the radiator was also analyzed to find an optimum in terms of cooling efficiency and aerodynamic performance. The investigation has been performed through Computational Fluid Dynamics (CFD) RANS simulations conducted with Ansys Fluent. Multiple attempts of validation of the numerical results were done in the radiator test bench available at Dallara, unfortunately, resulting in unsatisfactory reproducibility and coherence of the outcomes.

The investigation identified the hexagonal mesh pattern with a circular wire as the grille configuration that delivers the lowest static pressure losses while maintaining an equivalent level of debris protection. Pressure loss was found to be slightly more sensitive to changes in wire thickness than to variations in opening size. In both cases, the optimal configuration lies at the structural and functional limits of the grille: the wire should be as thin as structurally viable, and the openings as large as possible.
Although the pressure loss registered across the grille and radiator was independent of the distance between the two, the radiator showed an increased aerodynamic efficiency when the distance between the two was minimized, making this setup choice preferable whenever possible. The research also highlighted the potential benefits of using protective grilles to deflect the airflow and align it with the radiator's inlet face. However, the complexity of achieving an optimized grille design, combined with the additional costs associated with custom manufacturing, deemed the concept impractical.

The data collected from the numerical tests on various grille configurations served as the foundation for developing a mathematical model capable of predicting pressure losses for an arbitrary grille at a given incoming flow speed, within the range of 6 to 22 $\mathrm{m\,s^{-1}}$. This formulation was subsequently used to represent the grille as a porous medium. Validation was performed numerically, and the modeled grille in series with a radiator exhibited a total pressure loss only 0.5% higher than the configuration where the grille was modeled geometrically in series with the radiator, confirming the robustness and accuracy of the approach.

The research advanced the understanding of the aerodynamic impact of motorsport protective grilles, shedding light on the relative impact of their key geometrical parameters and positioning with respect to the radiator on the pressure losses. Looking ahead, the developed grille modeling provides a robust and accurate method for simulating its aerodynamic impact, paving the way for reducing safety margins in cooling system design and for further iterations and validation tests to ultimately implement it in full-scale car simulations.

Contents

List of Figures

List of Tables

Nomenclature

Abbreviations

Abbreviation	Definition
AKN	Abe Kondoh Negano
CAD	Computer Aided Design
CFD	Computational Fluid Dynamics
CRFM	Condenser, Radiator, and Fan Module
DES	Detached Eddy Simulation
LES	Large Eddy Simulation
PIV	Particle Image Velocimetry
RANS	Reynolds Averaged Navier Stokes
RMSE	Root Mean Squared Error
SST	Shear Stress Transport

Symbols

Symbol	Definition	Unit
A_0	Effective area	$[\mathrm{m}^2]$
AR	Aspect Ratio	[-]
C_F	Form-drag constant	[-]
$c_{p_{static}}$	Static pressure coefficient	[-]
D_h	Hydraulic diameter	$[\mathrm{m}]$
d	Grille wire diameter	$[\mathrm{m}]$
d_f	Fiber size	$[\mathrm{m}]$
d_p	Pore size	$[\mathrm{m}]$
d_{p_i}	i-th actual static pressure drop	$[\mathrm{Pa}]$
$\hat{d}_{p_i}$	i-th predicted static pressure drop	$[\mathrm{Pa}]$
K	Permeability	$[\mathrm{m}^2]$
k	Turbulent kinetic energy	$[\mathrm{m}^2\,\mathrm{s}^{-2}]$
l	Grille passage length	$[\mathrm{mm}]$
l_p	Radiator pipe length	$[\mathrm{mm}]$
$\dot{m}$	Mass flow	$[\mathrm{kg}\,\mathrm{s}^{-1}]$
n_1	empirical coefficient	[-]
n_2	empirical coefficient	[-]
n_3	empirical coefficient	[-]

Symbol	Definition	Unit
n_4	empirical coefficient	[-]
m_1	empirical coefficient	[-]
m_2	empirical coefficient	[-]
m_3	empirical coefficient	[-]
m_4	empirical coefficient	[-]
m_5	empirical coefficient	[-]
m_6	empirical coefficient	[-]
p	Pressure	$[\mathrm{Pa}]$
p_{static}	Static pressure	$[\mathrm{Pa}]$
p_∞	Freestream total pressure	$[\mathrm{Pa}]$
q_1	empirical coefficient	[-]
q_2	empirical coefficient	[-]
S	Shape factor	[-]
t	Grille mesh thickness	$[\mathrm{mm}]$
U_0	Discharge air velocity	$[\mathrm{m\,s^{-1}}]$
u_τ	friction velocity	$[\mathrm{m\,s^{-1}}]$
V	Airflow velocity	$[\mathrm{m\,s^{-1}}]$
y	Distance first control volume from the wall	$[\mathrm{m}]$
y^+	Dimensionless wall distance	[-]
α	Permeability	$[\mathrm{m^2}]$
β	Forchheimer coefficient	[-]
ϵ	Porosity	[-]
θ	Grille tilt angle	$[^\circ]$
μ	Dynamic viscosity	$[\mathrm{kg\,m^{-1}\,s^{-1}}]$
ν	Kinematic viscosity	$[\mathrm{m^2\,s^{-1}}]$
ρ	Density	$[\mathrm{kg\,m^{-3}}]$
ε	Turbulent dissipation rate	$[\mathrm{m^2\,s^{-3}}]$
ω	Specific rate of dissipation of turbulent kinetic energy	$[\mathrm{s^{-1}}]$

1

Introduction

Radiators are critical components in the thermal management system, with applications ranging from industrial to stationary and automotive. Their correct functioning directly impacts the system's overall reliability and ensures operational stability. Diving into the automotive world, despite their crucial role, radiators are vulnerable to the presence of debris encountered on the road, which might damage the fins, or even worse, the tubes containing the coolant fluid, reducing their efficiency or bringing it to a premature failure. This topic acquires even more importance in the context of motorsport applications, where the margins on the cooling requirements are reduced, and the cars are more exposed on track to the presence of harmful debris.

Radiator protective grilles are deceptively simple, but an essential solution to this problem. If properly designed, they block the majority of the debris collected during a race, which would otherwise hit the radiator, while preserving the airflow needed for the correct functioning of the radiator. However, their presence restricts the airflow and, in turn, also the cooling performance, introducing a fundamental engineering trade-off: between increasing protection and maximizing the airflow. The aim of this report is therefore to analyze the static pressure drop driver parameters alongside their relative importance, to provide all the necessary information needed for an efficient grille design, both in terms of the geometrical structure of the grille and position with respect to the radiator.

From a numerical perspective, high-fidelity simulation of protective grilles is computationally expensive, due to their fine geometrical structure, which requires dense volume meshes. To better manage this, without losing its influence on the flow, the grille has to be modeled in a simplified way. This project also aims to derive a mathematical parametrization that can be used as a backbone for the modeling of the grille.

The report is structured in three macro sections: the literature study, methodology, and results. The first one will serve as a starting point for the research, presenting the available knowledge on the topic, and will end with the definition of the areas of focus of the research. In the methodology section, the description of both the numerical and experimental setups used to answer the research questions is outlined. The general approach to the research is also described here, outlining the reasons behind the approaches taken and considerations made throughout the project. Finally, in the results section, all the numerical results are presented, and their quality and validity are discussed.

I

Literature Review

2

Previous Aerodynamic Studies

Thermal management is a key aspect of a vehicle design, responsible for maintaining the optimal operating conditions of the principal systems of the car, such as the engine, powertrain, brakes, and the cockpit environment. Proper thermal control ensures mechanical efficiency, safety, and reliability of the components.
Within the world of motorsport, the importance of thermal management is amplified due to three main aspects (Hansra [11]):

- High engine power density, hence producing more heat and requiring more cooling
- The need to maximize the aerodynamic performance, usually leading to tight packaging constraints limiting the amount of airflow reaching the radiators
- The need to minimize weight, limit the amount of coolant fluid, and the size of fans and radiators

The majority of race cars present protective grilles placed in front of the radiator to address the critical need to protect the cooling system (Zhang et al. [46]). The grille acts as a barrier, preventing debris, stones, and any other objects present on the road from striking the radiator at high speeds, damaging it.

2.1. Aerodynamic Considerations for Grille Design

As explained by Zhang et al. [46], one of the principal drawbacks of the protective grilles is the non-uniformity of the airflow past the grille opening. According to Kubokura et al. [21], non-uniform airflow may lead to a drop in radiator heat rejection performance of up to 10% compared to an equivalent cooling configuration with uniform inflow, even though the average flow velocity is the same.
This effect is very well visible in Figure 2.1, where the flow velocity drops significantly in the proximity of the grille struts.

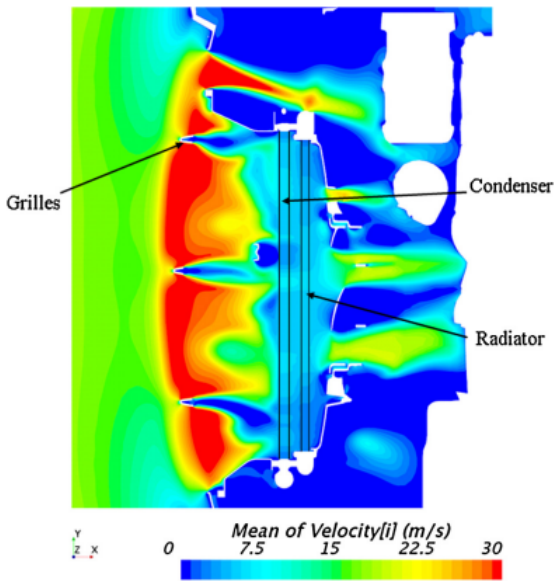

Figure 2.1: Stream-wise velocity on a plane at highway speed (70 mph) with the fan off condition, on a Hyundai Veloster, Zhang et al. [46].

Zhang et al. [49] claims that the grille's geometry and placement are directly responsible for how the air flows to the radiator. A consistent part of the total drag of a vehicle is generated by internal flow resistance, which is closely related to the thermal management and cooling. When designing a protective grille, it is hence important to keep in mind that it plays a key role in balancing the air resistance and the thermal management performance. For cases when the grille is not enclosed together with the same component to be cooled, poor orientation or placement of the grille can lead to the flow missing the radiator partially or completely, reducing the cooling effectiveness (as shown in Figure 2.2 a).

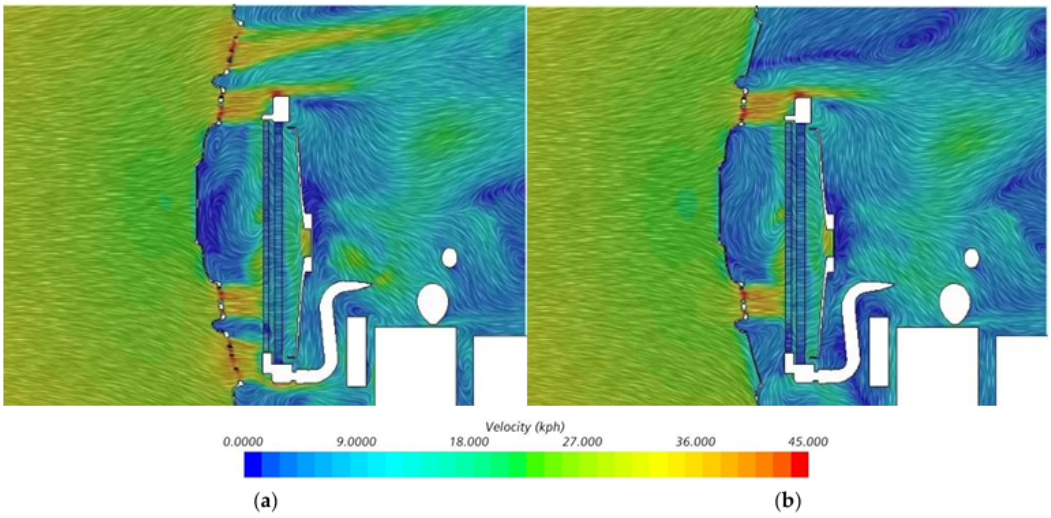

Figure 2.2: Comparison of velocity fields between two grille designs, Zhang et al. [46].

Blocking the futile openings forces the flow to be channeled into the remaining ones, enhancing the cooling performance (Figure 2.3).

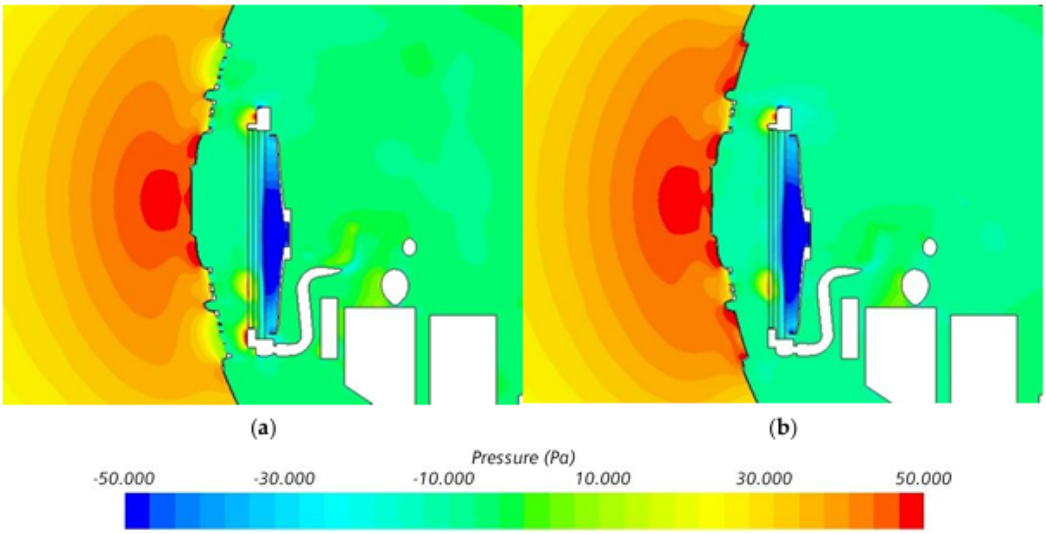

Figure 2.3: Comparison of pressure nephogram between fully open grille (a) and grille with upper closure (b), Zhang et al. [46].

The last point of attention raised by Zhang et al. [49] is on the aerodynamic interaction between components, especially when the flow is channeled to the radiator through two different openings. As shown in Figure 2.4, in the case investigated, the airflow entering from the lower side of the grille has an upwashing impact on the upper airflow, reducing the cooling efficiency of the latter, which partially overshoots the radiator. As a result, configuration (b) has a similar cooling performance to configuration (a), but significantly lower drag, since only the lower opening is present.

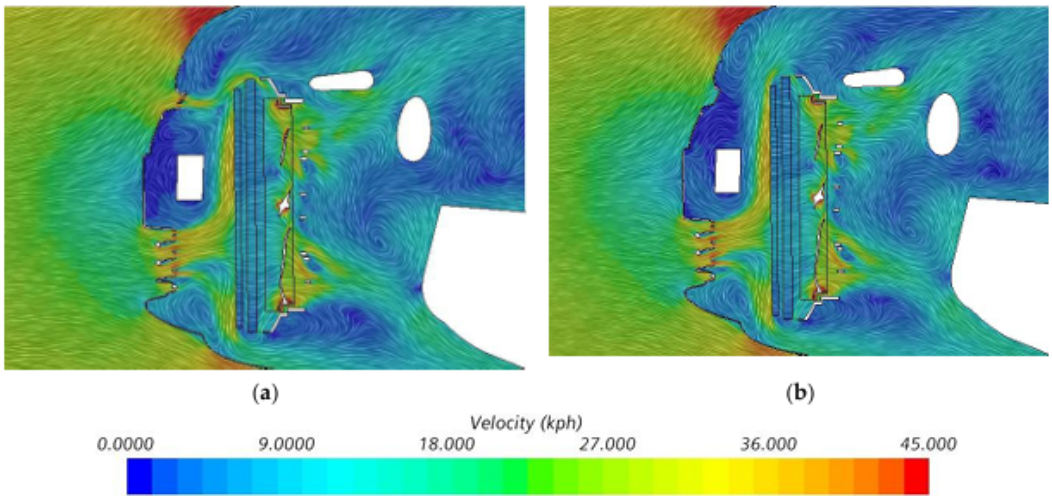

Figure 2.4: Comparison of velocity fields between a grille with an upper grille (a) and without (b), Zhang et al. [46].

2.2. Environmental Considerations for Grille Design

The main reason for installing protective grilles in front of race car radiators is to shield from debris, such as rubber marbles shed by hot and degrading tires during on-track running. It comes as a natural consequence that a driving factor in the design of protective grilles is their ability to sustain the impact of the debris, while still allowing enough air to pass through to meet the cooling requirement and avoid overheating of the engine.

Corfield et al. [6] investigated the problem of rubber marbles blocking the gaps in a double-element wing, reducing its aerodynamic efficiency. The debris was reproduced using blocking tape, allowing it to simulate its blockage in a controlled and repeatable way, as shown in Figure 2.5. The blockage width of the tape was increased at a Reynolds number of 7.4 x 10^5 from 10% to 100% of the span.
As most of the aerodynamic losses registered by a protective grille are in terms of pressure drag Yıldız et al. [44], it is interesting to focus on the drag coefficient loss presented in Figure 2.6. Interestingly, a sudden drop of drag was registered at the minimum tape width tested, and it remained constant until 70% of the span width, when it increased to a higher value than the clean configuration.

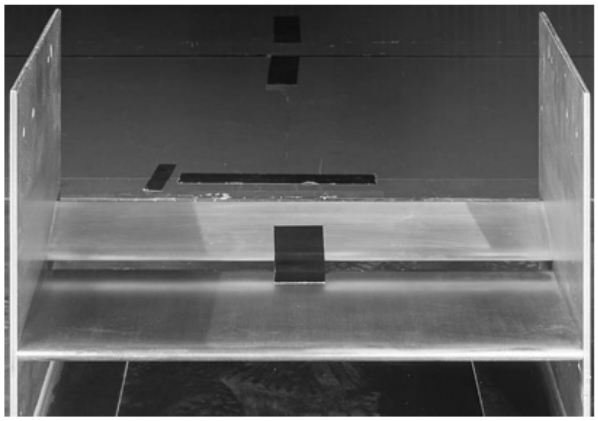

Figure 2.5: Tape blockage setup, Corfield et al. [6].

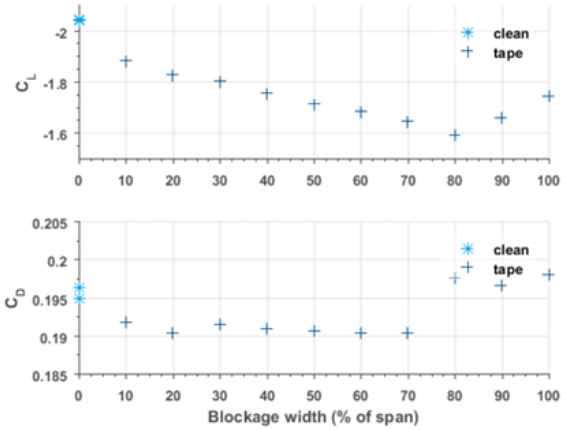

Figure 2.6: Debris force variation, Corfield et al. [6].

Corfield et al. [6] also discusses how the aerodynamic efficiency of the wing is highly dependent on the location of the blockage, resulting in being more detrimental when occurring in the middle, which is a region of high sensitivity.
Closely looking into the flow characteristics around the tape region shown in Figure 2.7, it is clearly visible how the airflow separates behind the tape, diverging outwards.
Translating this investigation on the double wing to the grille design, it is possible to conclude that the presence of marbles is detrimental to the airflow, leading to regions of separation behind the blockages, and their influence on the flow quality depends both on the size and position of the debris.

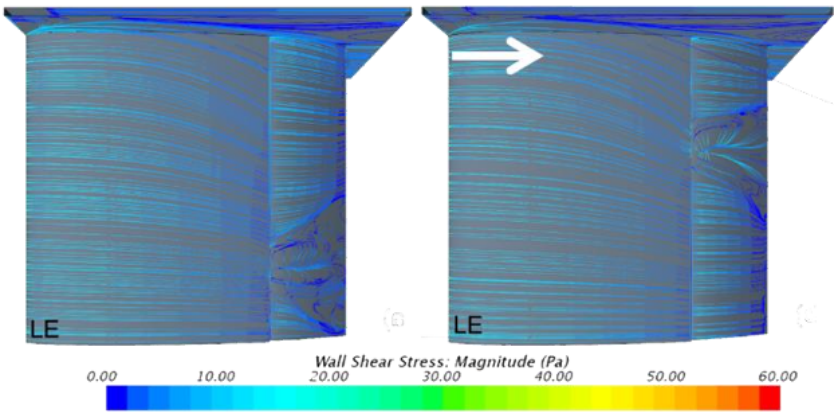

Figure 2.7: CFD surface streamlines on the underside of the main element, Corfield et al. [6].

Given the detrimental effect of rubber marbles on aerodynamic efficiency, it becomes relevant to the design of

a grille, the choice of material, aiming at reducing the percentage of marbles that remain stuck to the grille. On this end, Tiwari et al. [38] and Persson et al. [30] state that increasing the surface roughness generally leads to a strong reduction in adhesion between rubber and hard surfaces.

Pegasus Auto Racing Supplies [28] mentions that protective grilles for motorsport applications can vary in opening size depending on the type of track the car races into. The finest grilles can block even fine obstacles of just under 2 mm, with square openings of about 2 mm, which are suitable for an application where there is a significant amount of dust collected by the vehicle, like in off-road races. There are then larger grille meshes, which can span from square openings of about 3-4 mm for races where the exposure to debris is limited, all the way to the largest ones with openings of 5-6 mm, mostly used in races where the tracks are clean and there is very low probability of encountering small debris. The wider the openings, the more open area there is, so the less the blockage effect of the grille on the flow.

2.3. Grille Wake Analysis Outside Automotive Applications

Tian et al. [37] analyzed the wake of two configurations of two grilles (one with a circular, the second with a rectangular pattern, Figure 2.8) placed in front of an outdoor room conditioner.

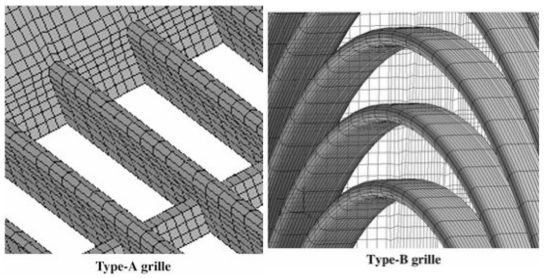

Figure 2.8: Grille types configurations, Tian et al. [37].

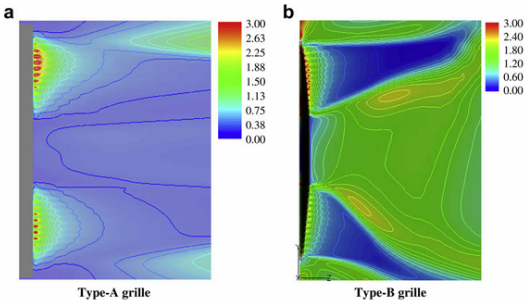

Figure 2.9: Turbulence kinetic energy contours of grille type-A and type-B, Tian et al. [37].

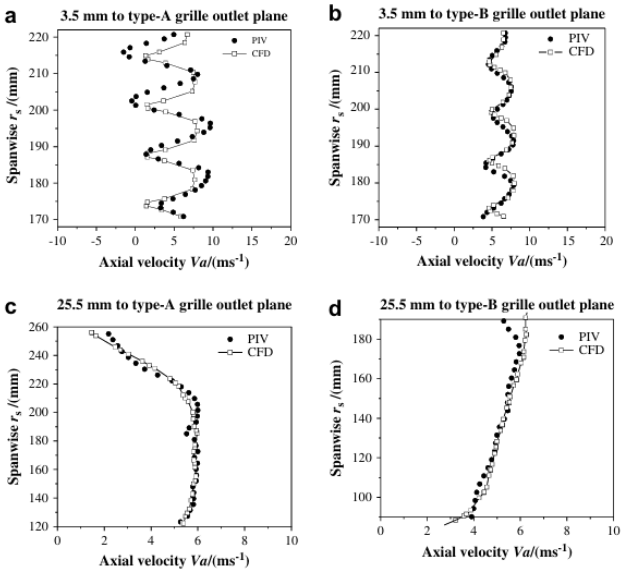

Figure 2.10: Comparison of axial velocity distributions between PIV and CFD for grille type-A and type-B, at the outlet plane at 3.5 mm and 25.5 mm, Tian et al. [37].

From the turbulent kinetic energy distribution of the two grilles, presented in Figure 2.9, the annular grille shows an overall lower and more uniformly distributed turbulent region. The rectangular grille instead has very localized vortex-shedding regions.
This consideration is supported by the axial velocity distribution at an outplane 3.5 mm downstream from the grille, in Figure 2.10. Both show momentum deficits caused by the struts, but the higher concentration of turbulent kinetic energy of grille type A is reflected by a velocity profile that dips sharply in this region. Although the stronger turbulence translates into a 9% loss of mass flow through the grille, it also allows the flow to mix faster, resulting in a more uniform axial velocity distribution at the 25.5 mm, which is generally more convenient for cooling purposes, Kubokura et al. [21].

Thijs et al. [36] confirmed the enhanced mixing effect, showing the peak turbulence intensity happening closer to the honeycomb grille when increasing the Reynolds number (Figure 2.11).

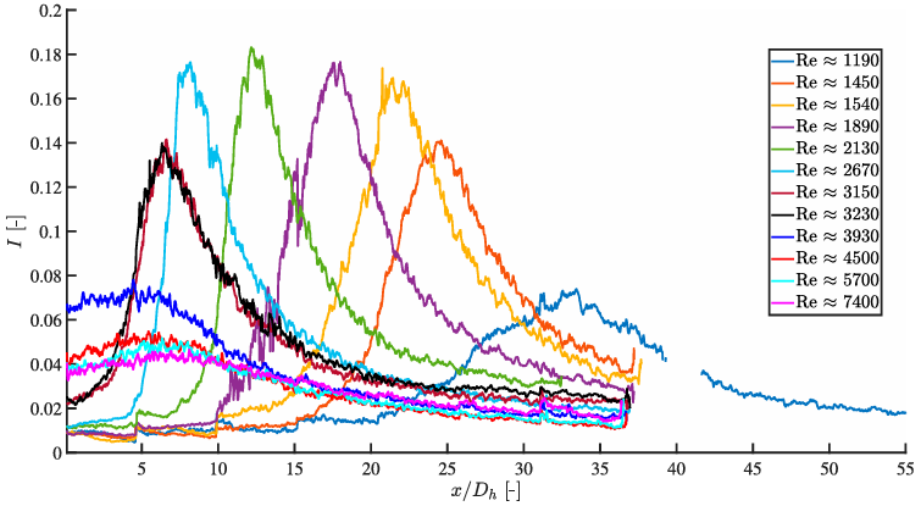

Figure 2.11: Streamwise turbulence intensity for increasing Reynolds numbers at the center of the channel, Thijs et al. [36].

The wake is highly dependent on the value of the Reynolds number. At Reynolds numbers between $1\text{x}10^5$ and $4\text{x}10^5$, Li et al. [23] state that the flow is more prone to cause flow blockage due to large-scale turbulent separation. Airflows at low Reynolds numbers have delayed separation, with the presence of large laminar separation bubbles and thicker boundary layers. At high Reynolds numbers ($5.2\text{x}10^5$ to $2.2\text{x}10^7$, which is a value in the range of typical motorsport applications), Wang et al. [41] reveal that small-scale turbulence becomes more abundant and finer, resulting in higher turbulent kinetic energy and more unsteadiness. This promotes an earlier transition, with smaller separation bubbles, hence a thinner boundary layer and reduced losses.

2.4. Grille Presence Effect Outside Automotive Applications

Koçal et al. [20] investigated the impact of a protective grille on the cooling performance compared to a setup without the grille.

The test was set up utilizing a regular grille with a rectangular and uniform pattern, with the incoming flow at 10 $\mathrm{m\,s^{-1}}$, the fan speed of 1964 rpm, the coolant flow rate of 21 $\mathrm{L\,min^{-1}}$, and coolant inlet temperature of 70°C. The setup is shown in Figure 2.12, and the results obtained are summarized in Figure 2.1.

Figure 2.12: Test Setup, Koçal et al. [20].

Parameter	With grille	Without grille
Cooling load (kW)	20.72	19.58

Table 2.1: Comparison of cooling performance with and without protective grille, Koçal et al. [20].

The configuration with the grille showed an increase in cooling load. Koçal et al. [20] explains that the grille focuses the flow more efficiently, guiding the airflow and limiting the swirling effects, which are detrimental to the cooling performance.
Racing cars don't typically have a cooling fan sucking air from the radiator; hence, the swirling effects are very limited, so the opposite effect to the one observed here may occur.

2.5. Flow Velocity Re-Distribution Around a Perforated Plate

Baines et al. [2] investigate the axial distribution of the flow upstream and downstream of a perforated plate. The setup used for the study is shown in Figure 2.13. In a fully developed and undisturbed flow constrained inside a channel, the velocity of the stream is higher at the core and lower at the sides. When such a flow encounters a perforated plate, this one acts as a dam, partially resisting the passage of the flow. The resistance is proportional to the square of the velocity: this generates a higher resistance at the core and lower at the sides. The larger pressure builds up in the center, pushing the flow towards the walls, where the velocity is lower, and so the resistance of the perforated plate.

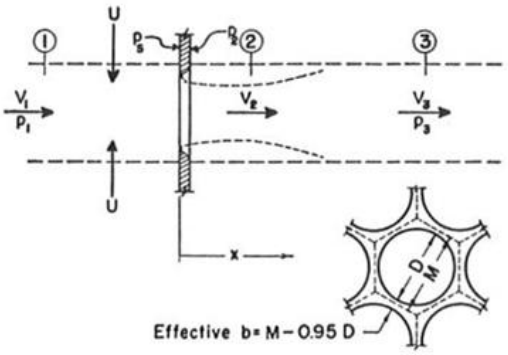

Figure 2.13: Perforated plate setup, Baines et al. [2].

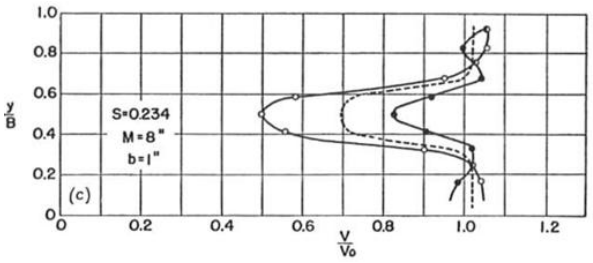

Figure 2.14: Effect of perforated plate on a simulated axially symmetric wake, Baines et al. [2].

This effect generates the axial velocity distribution as depicted in Figure 2.14. The axial distribution is shown in terms of $\frac{y}{B}$, where B is the width of the duct. The effect is present both upstream and downstream of the screen, although it is more evident upstream.

2.6. Grille Opening Parameters

Leaving styling considerations aside, the shape and size of the airflow intake opening are of utmost importance for the efficiency of the cooling system, as they control the quantity of air that reaches the radiator. The geometric characteristics that have the greatest impact on the blocking effect of the grille will be discussed below.

2.6.1. Grille Opening Size Parameter

A thorough investigation of the influence of the size of the grille opening on the drag coefficient and mass flow rate reaching the CRFM (condenser, radiator, and fan module) is performed by Kim et al. [17]. The car chosen for the test is a small passenger car, presenting three front grilles channeling air to the CRFM, as illustrated in Figure 2.15. All the tests are performed numerically, utilizing the CFD software Ansys Fluent with k-ε as a turbulent model, simulating a driving speed of 110 $\mathrm{km\,h^{-1}}$.

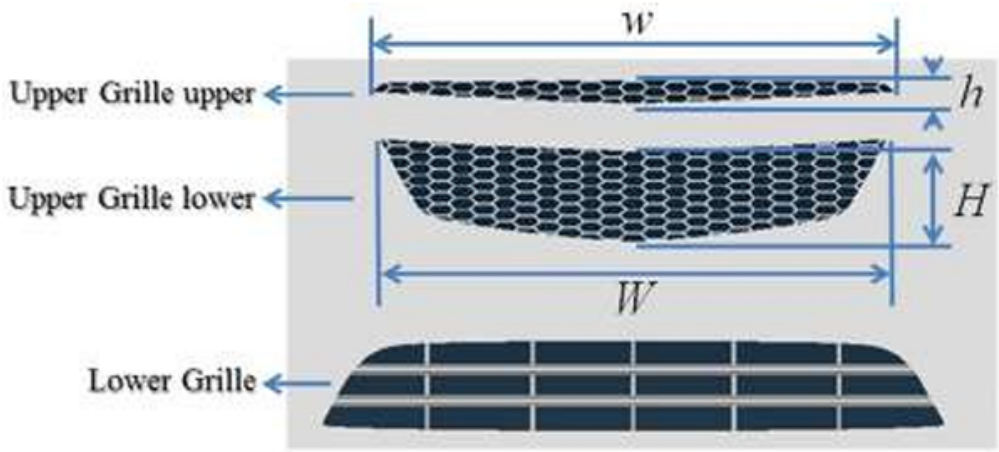

Figure 2.15: Grille shape of small passenger car, Kim et al. [17].

The grille opening size parameter was varied by changing the lengths h and H and the widths w and W (as illustrated in Figure 2.15 from -20% to +20% from the center of the grille, resulting in an area change from -40% to +40%, while maintaining the same shape. From the drag coefficient and mass flow rate obtained numerically in Figure 2.16 and Figure 2.17, Kim et al. [17] conclude that there is a direct proportionality between opening size and both mass flow rate and drag generation. The same effect is also observed by Petrov [31], suggesting that the effect is not limited to a single methodology but may represent a general trend.

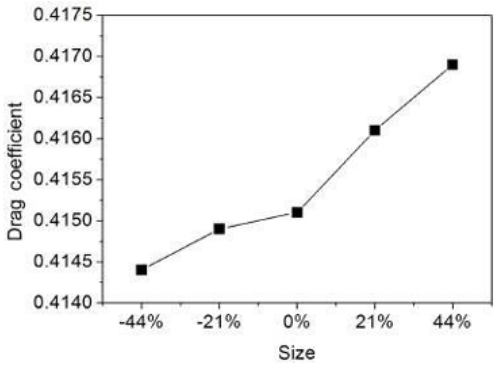

Figure 2.16: Drag coefficient versus grille opening size parameter, Kim et al. [17].

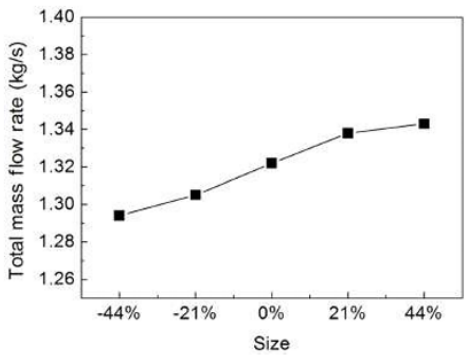

Figure 2.17: Mass flow rate versus grille opening size parameter, Kim et al. [17].

2.6.2. Grille Opening Aspect Ratio Parameter

Kim et al. [17] also test the effect of the aspect ratio of a protective grille on the drag coefficient and mass flow rate. To test this, the lengths h and H (see Figure 2.15) were varied from -20% to +20%, and the widths w and W adjusted to maintain the opening area constant.

From the findings, the impact of the aspect ratio on the drag coefficient is hardly noticeable (Figure 2.18), while the mass flow rate shows a slight increase as the vertical length increases (Figure 2.19). This conclusion is true for homogeneous and aligned flows, while a different trend could be seen with different inlet flow conditions.

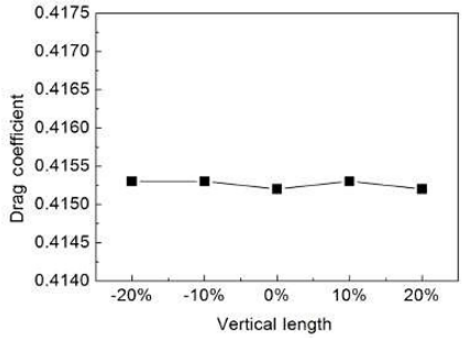

Figure 2.18: Drag coefficient versus grille opening aspect ratio parameter, Kim et al. [17].

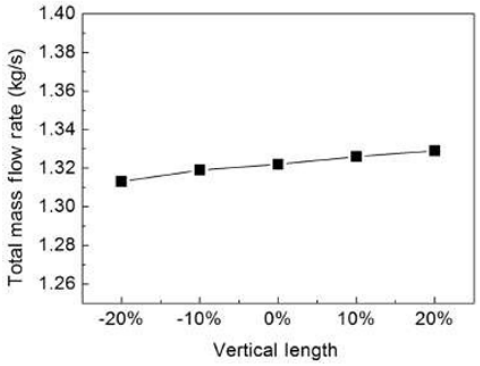

Figure 2.19: Mass flow rate versus grille opening aspect ratio parameter, Kim et al. [17].

2.7. Grille Mesh Parameters

A crucial aspect to consider when designing a protective grille is the type of mesh to use. This involves studying not only the geometrical shape of the single grid cells, but also their thickness and depth, and any pattern variations that may lead to benefits both in terms of thermal management and aerodynamic performance.

2.7.1. Grille Passage Length Parameter

The grille passage length is the grille depth, indicated with l in Figure 2.30. In the study, Kim et al. [17] varied the passage length from -2.5 mm to +5 mm with respect to the size of the base grille.

Interestingly, the drag increased for both an increase and a decrease of the passage length, while the mass flow rate into the engine compartment has a minimum at +2.5 mm.

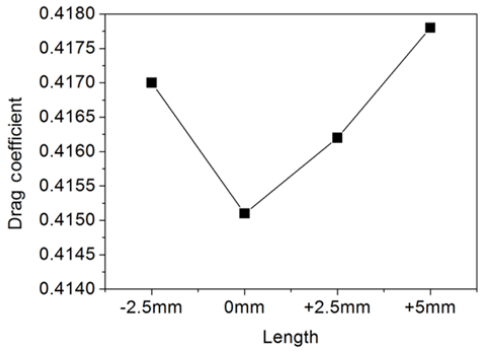

Figure 2.20: Drag coefficient versus grille passage length, Kim et al. [17].

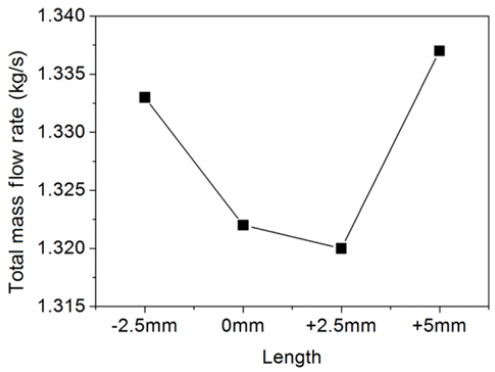

Figure 2.21: Mass flow rate through the grilles versus grille passage length, Kim et al. [17].

From the velocity contour plots (Figure 2.22), the increase in mass flow rate when decreasing the passage length is due to the reduced thickness of the boundary layer, with a consequent decrease in wake size. At +2.5 mm length, the boundary layer thickness significantly increased, leading to a thicker wake and bigger blockage of the flow, resulting in a lower mass flow rate. The drag in this case showed an inverted trend due to the higher airflow momentum loss due to the viscosity of the thicker boundary layer.
When increased to +5 mm, the airflow has time to be deflected by the upper surface of the grille, pressing down the boundary layer on the lower surface and allowing for an increase in the mass flow rate.

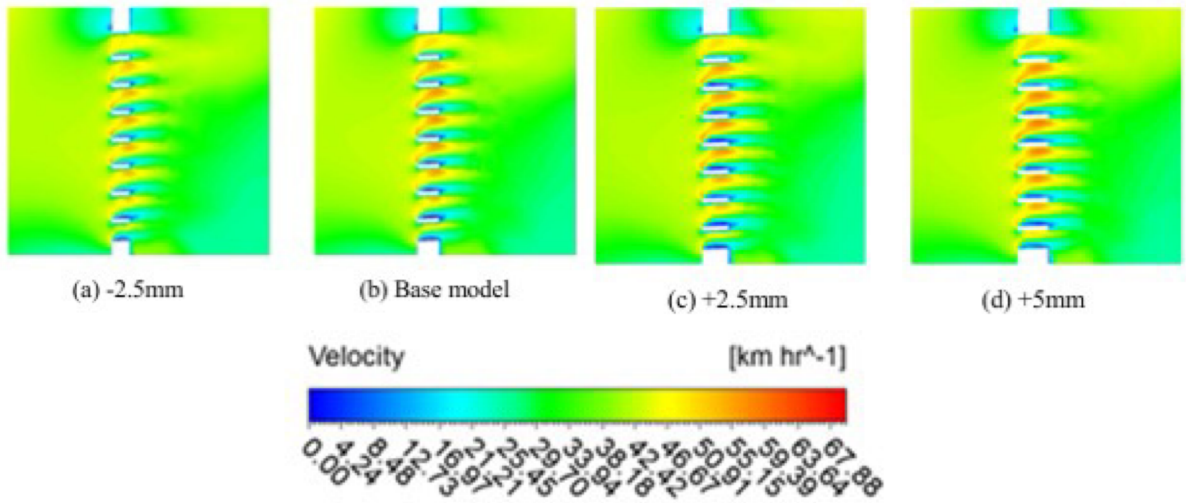

Figure 2.22: Velocity contours around grille, Kim et al. [17]

2.7.2. Grille Strut Thickness

The thickness of the grille's strut is indicated in Figure 2.30 with the variable t.
Kim et al. [17] witnesses, once again, a similar trend of the drag coefficient and mass flow: as the thickness of the grille mesh was increased, the total drag and mass flow through the engine compartment were decreased.
The drag of the grille alone increases when t is thicker because of its greater blockage, augmenting the pressure drop, but the blockage also allows lower pressure in the engine room, resulting in an overall drop of drag.

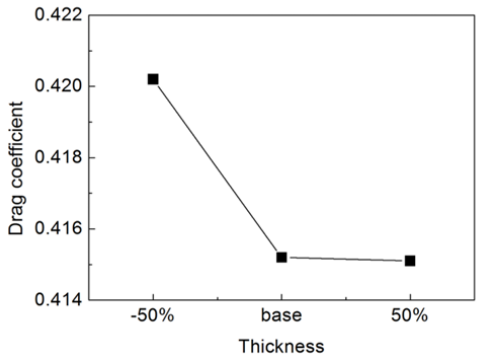

Figure 2.23: Drag coefficient versus grille thickness, Kim et al. [17].

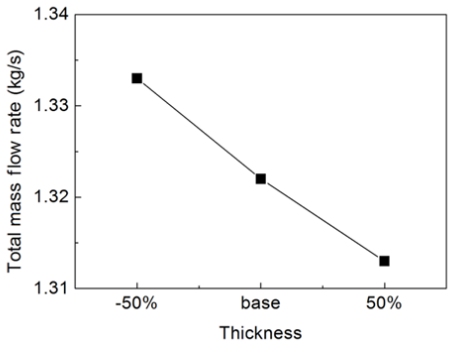

Figure 2.24: Mass flow rate through the grilles versus grille thickness, Kim et al. [17].

A similar aspect on the influence of varying the width of vertical bars composing a grille was also studied by Qi et al. [33], but in this case, maintaining the grille opening area constant; as the bar width increases, the number of bars decreases, but the open area remains the same.

From the research, wider bars seemed to cause smoother flow into the cooling module, reducing turbulence in front of the radiator, but only a marginal effect was observed.

In general, if the opening area available is constant, having a thin grille structure is more beneficial for the mass flow, as thicker ones would reduce the available area for the air to pass and increase the blockage effect. On the other hand, if there is room to modify the air intake opening, a wider grille structure allows for the breakup of the large turbulent structures, allowing jets of air to pass through in a more ordered and sheet-like manner, which is beneficial for cooling purposes, although the effects are marginal.

2.7.3. Grille Mesh Geometry

Qi et al. [33] simulate five different grille mesh shapes to see how they would affect the cooling performance of a series hybrid truck. The study was carried out numerically, using large eddy simulation (LES) as a turbulence model, at a driving speed of 68 $\mathrm{km\,h^{-1}}$. The condenser, radiator, and fan were modeled as porous media with the X direction as the preferred direction and an inertial resistance 100 times higher in the other directions. The shapes tested were: regular hexagon, horizontal bar, vertical bar, square, and rhombus, all with the same total opening area.

The results collected from the study are shown in Figure 2.25, in terms of air mass flow at the grille, condenser, and radiator levels. Although the vertical bar design was the one registering the lowest amount of airflow at the grille level, it resulted in being the one with the best cooling performance (mass flow through the radiator). As Qi et al. [33] describe, the vertical bars help the flow to be channeled more uniformly and to concentrate it towards the center, where the radiator is. Furthermore, their vertical alignment helps to reduce vortex formation in front of the cooling module, making the airflow more stable and uniform.

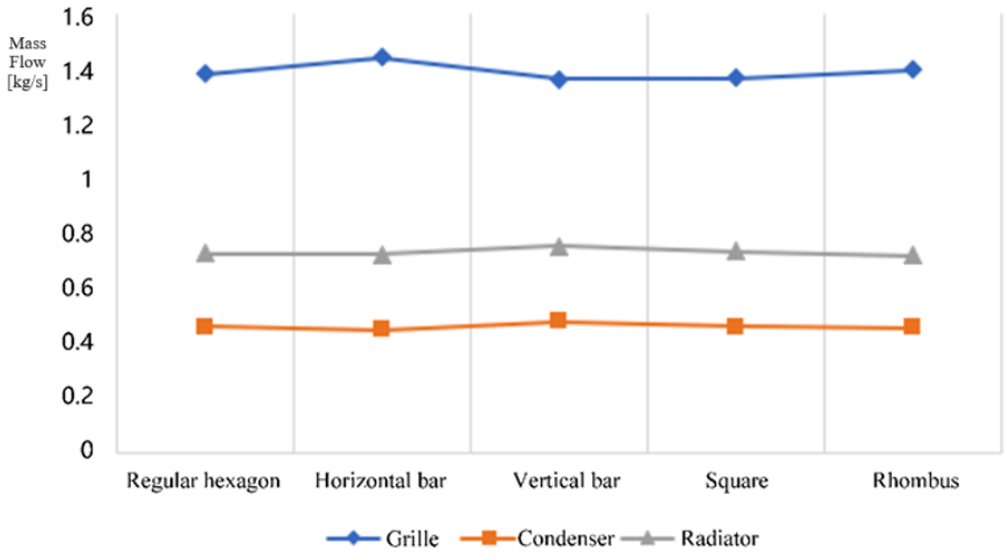

Figure 2.25: Air mass flow detection of grille, condenser, and radiator under different grille shapes, Qi et al. [33].

This study demonstrates that when the cavity between the grille and the radiator is not sealed, not all air entering the grille contributes to cooling, and it is of utmost importance to take directionality and turbulence generation into account when designing a protective grille.

2.7.4. Grille's Wire Cross Section

Hoerner [13] studied the effects on the drag coefficient for the flow passing over a sphere and a square block. While the sphere's curvature allows the boundary layer to stick longer to its surface (delaying separation to 120°-160°), the sharp edges of the square force the flow to separate immediately. This has a direct effect on the pressure drag generation, bringing the drag coefficient of the square to be significantly higher compared to the sphere. In the range between $Re = 10^3$ and $Re = 10^5$, the drag coefficient stays relatively stable, with the drag coefficient oscillating around 1.17 for the circular shape, and 2.05 for the square, resulting in a $\approx 75\%$ increase.
This knowledge can be translated to the grille's wire, where having a circular cross-section is expected to reduce the pressure drop across it compared to the square one.

2.7.5. Grille Strut Pattern

Zhao et al. [50] investigated the effect of varying the grille strut spacing on the aerodynamic downforce of a vehicle with CFD simulations.
The maximum pressure drop occurs at the grille with the least spacing (12.5 mm), while the minimum occurs at the 40 mm spacing. Beyond this gap size, fluid backflow started to occur. In the context of cooling, lower pressure drops are preferred, as they improve the airflow, but at the same time, they may compromise protection from debris. In the case investigated, the grille struts have a size comparable to that of a wing profile; therefore, the grille might also contribute to the vehicle's downforce; in such cases, smaller gaps are more beneficial, so a trade-off between cooling and aerodynamic performance must be found.

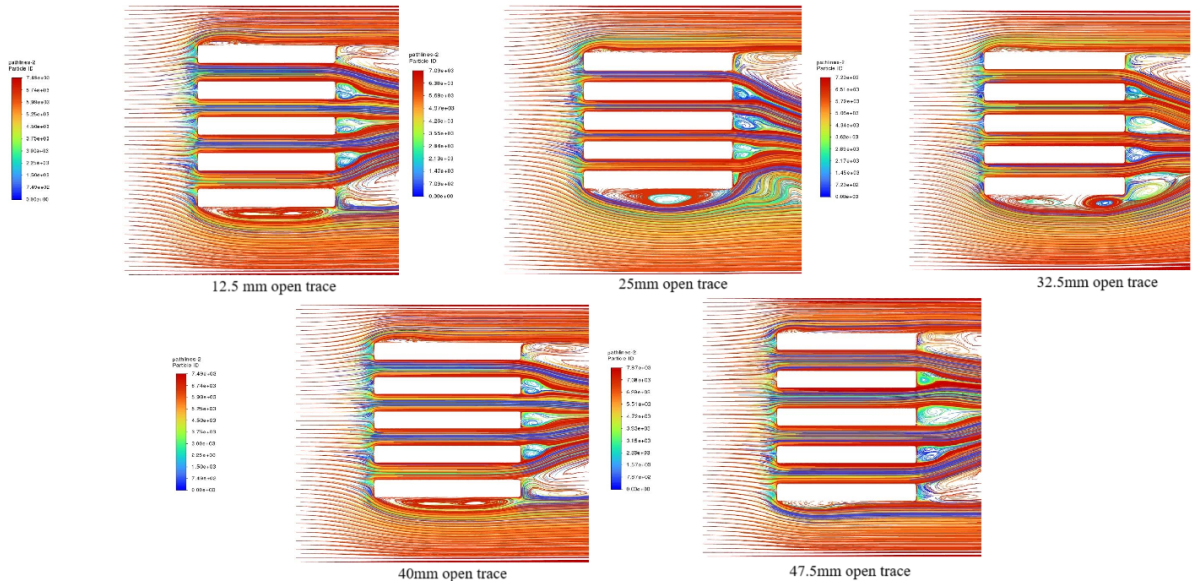

Figure 2.26: Comparison of flow streamlines with varying open trace spacing, Zhao et al. [50].

Koçal et al. [20] analyzed the effect of varying the grille pattern cross-section on the cooling performance. In Figure 2.27, the configurations tested are reported.

Figure 2.27: Grille models with varying pattern, Koçal et al. [20].

As shown in Table 2.2, the highest performing pattern was the decreasing grille section. This demonstrates, once again, how grille geometry significantly affects the distribution of the incoming air before it is directed towards the radiator. As discussed earlier in subsection 2.7.2, a smaller mesh size helps to uniform the flow. The decreasing section presents the finer grid resolution in the center, favoring airflow centralization, resulting in a better cooling load; the flow is indeed forced to pass through smaller openings in the center, where it accelerates, creating a ”cone-like” shape past the grille.
On the contrary, the increasing section has the opposite effect, resulting indeed in the lowest cooling performance.

Parameter	Increasing section	Decreasing section	Fixed Section
Cooling load (kW)	18.86	21.44	20.72

Table 2.2: Varying grille sections test results, Koçal et al. [20].

2.7.6. Effect of Grille Curvature

Liu et al. [24] investigated the aerodynamic performance of the curvature of the grilles. For the study, five grille designs have been studied: straight, concave, M-shaped, W-shaped, and convex, shown in Figure 2.28.

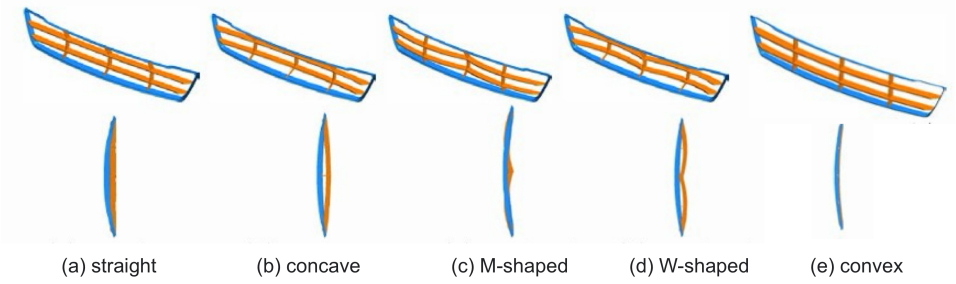

Figure 2.28: Grille shapes investigated, Liu et al. [24].

The simulation focuses on the drag coefficient and mass flow rate at the radiator. Liu et al. [24] reports that all grilles performed similarly, although the straight one resulted in being the best option (respectively in the order straight > convex > M-shaped > concave > W-shaped).

The velocity plots in the area between the grille and the radiator are shown in Figure 2.29, where the grilles are ordered from the best performing (straight) to the least performing one (W-shaped). The red circle highlights the

area of the flow leaking out of the engine compartment. From (a) to (e), the velocity in this area increases, and indeed also the cooling performance decreases.

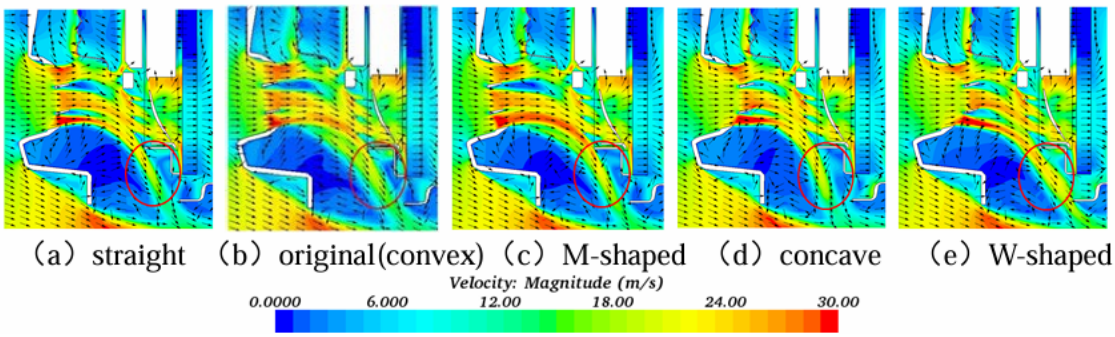

Figure 2.29: Velocity vector plot different grille curvature configurations, Liu et al. [24].

2.7.7. Grille Tilt Angle Parameter

Hsieh et al. [14] and Kim et al. [17] investigate the influence of the tilt angle θ (see Figure 2.30) on the airflow flowing through the protective grille, directly impacting the heat dissipation efficiency of the radiator.

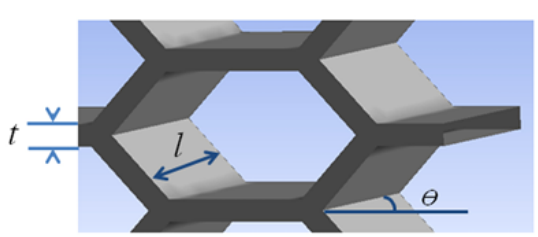

Figure 2.30: Grille mesh shape of small car, Kim et al. [17].

The velocity contours shown in Figure 2.31 highlight the boundary layer and wake formation around the grilles, clearly suggesting a better flow alignment in the 9° angle case, with a thinner boundary layer and wake width. From Figure 2.32, the flow appears separated into an upper and lower region, split by the stagnation point that is formed around the center line of the grille. When the tilt angle is increased, the flow is better aligned and passes through the grill smoothly, increasing the mass flow rate. In general, Hsieh et al. [14] and Kim et al. [17] agree on the fact that there is an optimum inclination angle that minimizes the pressure drop over the grille, and that is when the flow is aligned with the grille cells, allowing it to flow smoothly through it, reducing the area of stagnation.

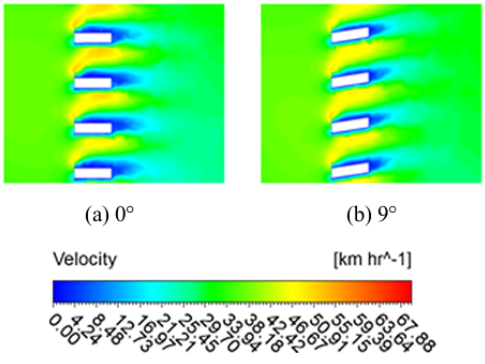

Figure 2.31: Velocity contours near grille, Kim et al. [17].

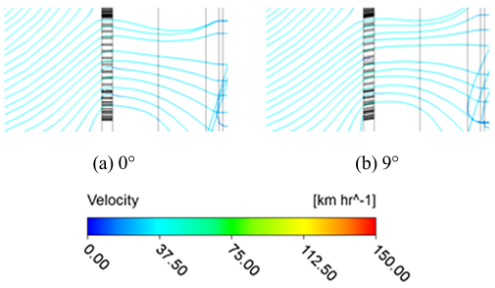

Figure 2.32: Streamlines passing through grille, Kim et al. [17].

The observations made above are perfectly supported by the drag and mass flow plots, both showing a matching trend (Figure 2.33 and Figure 2.34), with a sudden drop at 3° angle. Kim et al. [17] were able to conclude that the tilt angle affects the flow rate into the engine room, which is directly followed by a variation in drag generation. The optimum tilt angle depends on the direction of the incoming flow, with the best option being the one that minimizes the area of stagnation.

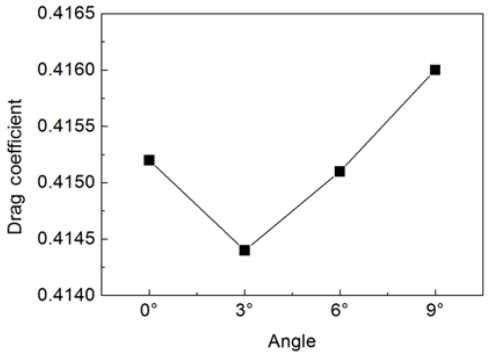

Figure 2.33: Drag coefficient versus grille tilt angle, Kim et al. [17].

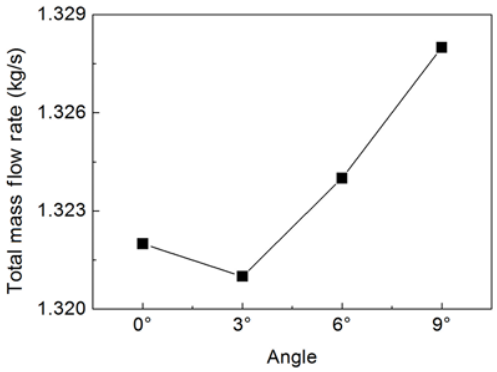

Figure 2.34: Mass flow rate through the grilles versus grille tilt angle, Kim et al. [17].

3

Numerical Modeling of Grille-Radiator Set-Up

3.1. CFD Turbulence Models

One of the crucial aspects of CFD simulations is the choice of an appropriate turbulence model. The key parameters to consider in the choice are the type of flow and boundary conditions (presence of walls, flow separation prediction, ...), the accuracy needed, and the amount of time and economic resources available to perform the simulations. Yu et al. [45] analyzed and compared the accuracy of three turbulence models (RANS (Reynolds Averaged Navier Stokes) with k-ε model, LES (Large Eddy Simulation), and DES (Detached Eddy Simulation)) in predicting the flow characteristics in an engine compartment placed behind a radiator. Table 3.1 shows a summary of the results obtained.

Parameters	**RANS**	**LES**	**DES**
CPU time (h)	12.3	34.4	22.1
Accuracy compared to experimental data	Failed to predict recirculation zones and vortex cores	Captured vortex structures and recirculation zones	Best accuracy of all

Table 3.1: Comparison between CFD turbulence models, Yu et al. [45].

DES, which is a hybrid model combining RANS in the near-wall region and LES far from the walls, resulted in being the best option in terms of accuracy, although it is not able to predict the large-scale eddy currents in the boundary layer. Even though the RANS model showed the lowest accuracy, in terms of computational resources, it was by far the cheapest, making it the best accuracy-to-cost ratio option for industrial designs.

Zhang et al. [47] and Igali et al. [16] tested the accuracy of some of the most used RANS-based turbulence models in vehicle aerodynamics: k-ε, the realizable k-ε, Abe-Kondoh-Nagano (AKN) k-ε, V2F, and k-ω SST. Although the realizable k-ε showed a really good correlation with the experimental results, which are only available for the drag coefficient, though, while the k-ω SST model was the overall closest to the results predicted by the DES models. Since the latter is also widely used in motorsport applications, it will be used as a turbulence model for

the CFD simulations.

3.2. Radiator Modeling

Three main approaches are used when modeling radiators in CFD: physical modeling, the porous media approach, and empirical models. The choice between them depends on the degree of accuracy required and the amount of time and resources available for the specific project.

3.2.1. Detailed Geometrical Modeling

The detailed geometrical modeling of the radiator is the most accurate of all, and it is typically used in contexts where detailed design or optimization is needed.
Ibrahim et al. [15] utilized this approach to compare two cooling systems, one with inline tubes and one with staggered ones. The geometry of the radiator was built using ANSYS software, and the airfield, tube, and water inside it were all included in the model. Another example is the work performed by Pendyala et al. [29] to find out the best material to use for a radiator to maximize heat transfer. Also in this case, very high accuracy is needed; therefore, the radiator was modeled using the CAD software Catia V5 and then simulated in Ansys Fluent.

3.2.2. Porous Medium Modeling

It is a widely used CFD technique for simulating radiators, without having to reproduce the detailed geometry of the fins and tubes, which would make the simulation computationally expensive.

This modeling approach consists of modeling the presence of the radiator in terms of pressure drop through the Darcy-Forchheimer-Brinkman formulation (Çetin et al. [5]), whose terms vary depending on the flow regime.
In the case of laminar and viscous flow, there is a linear relationship between the velocity and the pressure jump:

$$-\frac{dp}{dx} = \frac{\mu}{K}V \tag{3.1}$$

where μ is the dynamic viscosity, dx is the pipe length (distance over which the pressure drop is measured), V is the velocity of the flow, and K is the permeability coefficient. For higher Reynolds numbers, with the presence of turbulence in the flow, the Forchheimer term (β) is added to Darcy's formulation (Çetin et al. [5], Aydın et al. [1]):

$$-\frac{dp}{dx} = aV + bV^2 = \frac{\mu}{K}V + \rho\beta V^2 \tag{3.2}$$

Çetin et al. [5] compare the pressure drop prediction obtained through CFD simulations from the porous media and the physical fin. Although the mesh of the porous media was obtained with only 5320 cells per unit cell mesh, compared to the 4900713 cells of the physical one, the difference in terms of pressure jump is within 2.5%, as shown in Figure 3.1, which is acceptable for thermal analysis. The advantage of using a porous medium is that it allows for the simulation of a full-sized radiator with limited computing time, thanks to the reduced amount of mesh cells required.
Aydın et al. [1] compared the porous media to experimental results obtained from a custom-built test chamber. The results, shown in Figure 3.2, also highlight a low percentage difference in pressure drop measured, with a maximum deviation of 5.55%, considered acceptable for a numerical study.

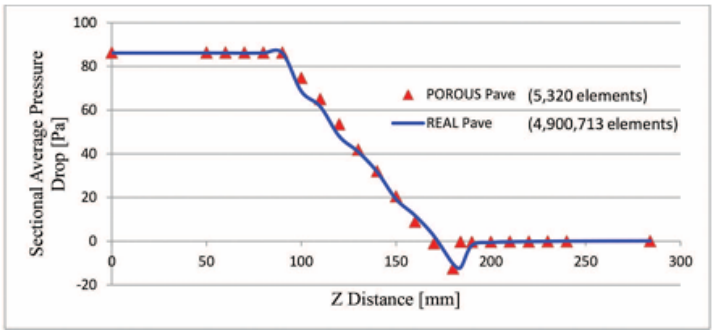

Figure 3.1: Comparison of sectional average pressure drop between physical fins and porous model, Çetin et al. [5].

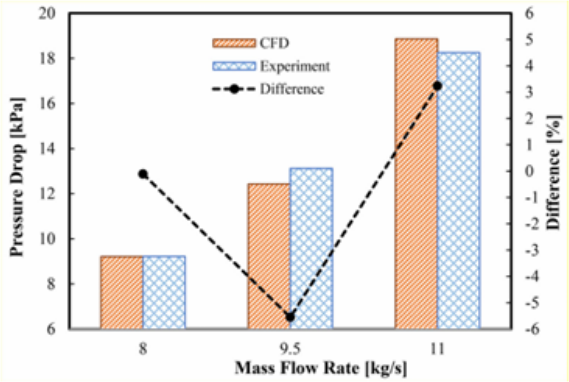

Figure 3.2: Comparison of pressure drops for different mass flow rates, Aydın et al. [1].

3.2.3. Empirical Modeling

Zhao et al. [51] presented a radiator model for CFD applications that simulates the flow behavior through the conservation of mass, momentum, and energy, and the geometry of the radiator is simplified. Also, the heat transfer mechanisms (conduction and radiation) are governed by Fourier's and Stefan-Boltzmann laws, respectively, while for the convection, the oil channel inside the radiator is preserved, while the air domain is removed and modeled with Newton's law of cooling.
Boundary conditions are also set to control the pressure and temperature close to the walls, at the inlet and outlet.

While this model is computationally cheaper than canonical methods, it is founded on numerous assumptions that stand behind the empirical formulations used, such as the assumption of fully developed flow and the uniform air convection parameter. It is designed for steady-state solutions, meaning it does not capture any load transient behavior, and the local turbulence is also lost. This makes this method not suitable for most motorsport applications, where a higher amount of detail in the outcomes is required.

3.3. Grille Modeling

As the grille is the core element of this project, it is essential to investigate the different methods available to model it for CFD simulations. A thorough overview of the methods available allows to choose the best way to simulate its impact, considering both accuracy and computational cost.

3.3.1. Detailed Geometric Modeling

Having the exact geometry of the grille simulated in the CFD is the best option for accuracy, and it is used whenever there is an investigation on the grille that requires high accuracy (Tian et al. [37], Kim et al. [18]). Since the flow around the grille is very prone to separation (aerodynamically, it is a very sensitive region), it requires a very fine surface mesh, as shown in Figure 3.3.

Mahgoub et al. [25] analyzed the blockage effect of a windbreak, utilizing the exact geometry of the net. From the velocity contours using the exact geometry in Figure 3.4, it can be noted that the velocity distribution closely matches the one obtained from PIV testing (only 4% error).

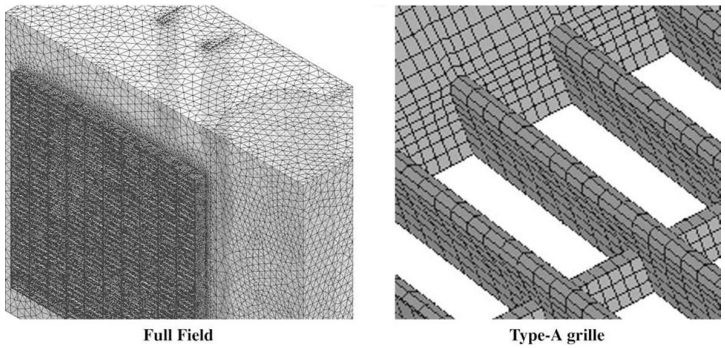

Figure 3.3: Grille surface mesh adopted, Tian et al. [37].

In terms of pressure drop, a 14% difference with the experiments was registered, probably due to the k-ε turbulence model used, which may not capture all the turbulent structures in the near-wall area (Mansour et al. [27]), which contains large adverse pressure gradients.

3.3.2. Porous Medium Modeling

In a similar fashion to the radiator, the grille acts as a barrier to the flow, presenting a difference in velocity, and hence also pressure, between its outer and inner sides. It can therefore be modeled as a porous medium, following the Darcy-Forchheimer-Brinkman formulation of pressure drop as presented earlier in subsection 3.2.2.

Mahgoub et al. [25] compare the CFD results of a windbreak net modeled as a porous medium with the CFD results obtained by modeling it with the exact geometry and with the data obtained from an experimental test performed in the wind tunnel. The number of grid cells, like in subsection 3.2.2, is drastically reduced by an order of magnitude when modeling the grille as porous media, making the simulation computationally cheaper. The simulation was performed at a wind speed of 2 $\mathrm{m\,s^{-1}}$, which is rather low for automotive applications.

The velocity field of the three tests performed is shown in Figure 3.4. While the flow velocity distribution obtained from CFD with exact geometry and PIV shows similar patterns, the one obtained through porous media shows a higher speed on the suction side, behind the windbreak, due to the simplification of the wake structures, enhancing the apparent momentum exchange,resulting in an overestimation of the mixing in this region.

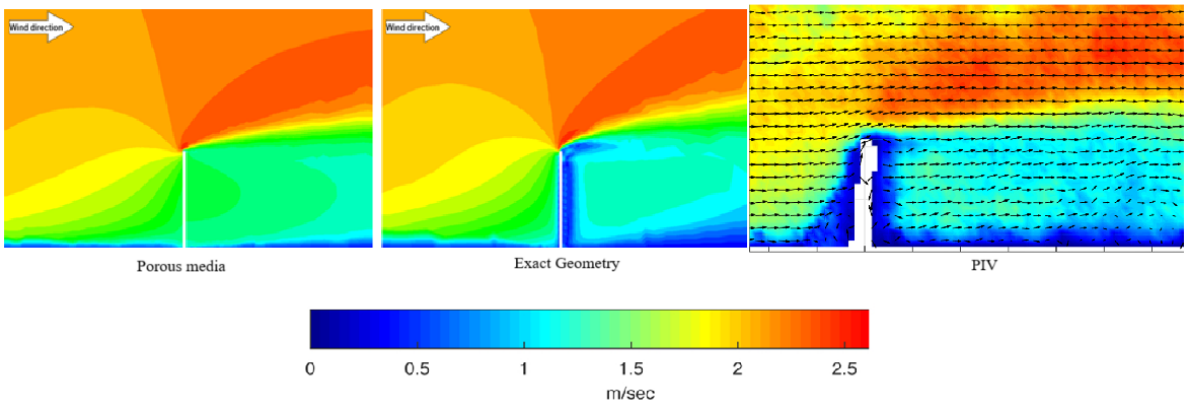

Figure 3.4: Comparison of velocity contours obtained from PIV, exact geometry modeling, and porous media approach, Mahgoub et al. [25].

Compared to the experimental results, the porous medium model shows an error of 6% for the velocity, and 26% for the pressure drop (measured with pressure taps on both sides of the windbreak). It must also be noted that the

results are evaluated at the symmetry plane, which might not be fully representative of the spanwise average of the flux.

The porous media can successfully capture the general characteristics of the flow, but it fails to predict the details of the flow. The porous media can be used as an approach in more complex geometries, where its relative influence is low, and it can reduce computational time. The study also suggests that the porous media approach is less accurate when used for more open geometries, such as a grille if compared with the same approach applied to a radiator.

Since the pressure drop across the windbreak is evaluated by subtracting the static pressure at the two surface levels, the witnessed error is significant, since the flow characteristics are poorly represented on the downstream side. Further downstream, however, the pressure coefficient distribution appears to be quite similar (Figure 3.5). In the case of the protective grille, this is still a favorable scenario; ultimately, what matters most is the cooling performance of the radiator, so if the presence of the grille does not significantly disturb the flow quality at the radiator inlet, then the model can be considered effective.

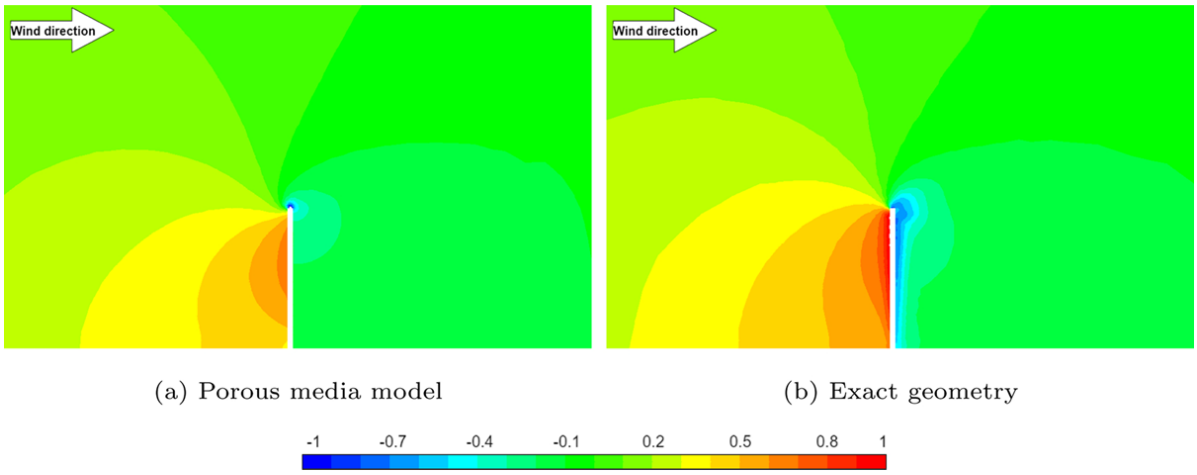

Figure 3.5: Comparison of pressure coefficient contours at the symmetry plane obtained from exact geometry and porous media approach, Mahgoub et al. [25].

Forchheimer Equation Coefficients Formulations

The static pressure drop imposed in the porous medium is governed by the Forchheimer equation, presented in Equation 3.2. The permeability coefficient K and the Forchheimer coefficient β, can be further broken down and calculated from mathematical formulations dependent on the geometrical structure of the grille.

Since the grille acts as a medium with very high porosity values, the most suitable models for K and β are those developed for metallic foams, which exhibit comparable porosity values (typically in the 0.7–0.9 range). In Table 3.2, some of the models derived for open-cell metal foams are presented:

Formulation	Expression	Variables
Du Plessis et al. [7]	$K = d_p^2 \frac{\epsilon^2}{36\chi(\chi-1)}$ $\beta = \frac{2.05\chi(\chi-1)}{\epsilon^2 d_p(3-\chi)}$ $\chi = \frac{d_f^2 \cdot \epsilon}{d_p^2}$	ϵ: porosity d_p: pore diameter d_f: fiber diameter
Dukhan et al. [9]	$K = \frac{1}{1.25 \cdot 10^8} \left[\frac{\epsilon^3 d_f}{(1-\epsilon)^2}\right]^{0.6155}$ $\beta = 1336.7 \left[\frac{(1-\epsilon)^2}{\epsilon^3 d_f}\right]^{0.6184}$	ϵ: porosity d_f: fiber diameter

Calmidi [4]	$K = d_p^2 \cdot 0.00073(1-\epsilon)^{-0.224}\left(\frac{d_f}{d_p}\right)^{-1.11}$ $\beta = 0.00212\frac{(1-\epsilon)^{-0.132}\left(\frac{d_f}{d_p}\right)^{-1.63}}{\sqrt{K}}$	ϵ: porosity d_p: pore diameter d_f: fiber diameter
Richardson et al. [34]	$K = \frac{\epsilon^3}{AS_v^2(1-\epsilon)^2}$ $\beta = \frac{BS_v(1-\epsilon)}{\epsilon^3}$ $S_v = \frac{4\epsilon}{d_p(1-\epsilon)}$ $A = 9.73 \cdot 10^2 d_p^{0.743}(1-\epsilon)^{-0.0982}$ $B = 3.68 \cdot 10^2 d_p^{-0.7523}(1-\epsilon)^{0.07158}$	ϵ: porosity d_p: pore diameter
Dukhan [8]	$K = c_1 \cdot e^{c_2\epsilon}$ $\beta = c_3\epsilon + c_4$	ϵ: porosity c_1, c_2, c_3, c_4: curve-fit constants
Ergun [10]	$K = A \cdot \frac{\epsilon^3 \cdot d_p^2}{(1-\epsilon)^2}$ $\beta = B \cdot \frac{1-\epsilon}{\epsilon^3 \cdot d_p^2}$	ϵ: porosity d_p: pore diameter A,B: empirical constants
Yang et al. [43]	$K = d^2\frac{\epsilon\left[1-(1-\epsilon)^{1/3}\right]^2}{36\left[(1-\epsilon)^{1/3}-(1-\epsilon)\right]}$ $d = \sqrt{\frac{\chi}{\epsilon}}d_p$ $\chi = \frac{\epsilon}{1-(1-\epsilon)^{1/3}}$	Does not have the viscous term ϵ: porosity d_p: pore diameter

Table 3.2: Permeability and Forchheimer coefficients correlations for open-cell metal foams

Yang et al. [42] validate, among others, also the models proposed in Table 3.2, against experimental data collected from open literature on the pressure drop of fluid flow through metallic open-cell metal foams. Out of all the models tested, the one that returned the lowest root mean square errors (RMSE), was Calmidi's formulation. To further improve the accuracy of the existing models, Yang et al. [42] fitted the data using a *"least squares"* fitting approach; the original models had fixed empirical constants derived from limited datasets, which, when applied to different ranges of porosity, showed systematic deviations from the collected data.

3.3.3. Random Blocking Method

Zhang et al. [48] introduce a new simplified method to model a grille diffuser (utilized for a ventilation system), which aims to significantly reduce the computational time and surface mesh resolution needed for common grille modeling techniques.

The approach consists of specifying the flow conditions on CFD cells of simplified grille geometry. The actual velocities are assigned directly to a certain ratio of cells, while the others are randomly blocked. A schematic representation of the model grille is shown in Figure 3.7. The determination of the closed cells (black ones) is done through a mathematical random function that assigns 1 to open cells and 0 to closed ones. The amount of blocked cells must be such that the total effective area ratio of the grille is preserved.

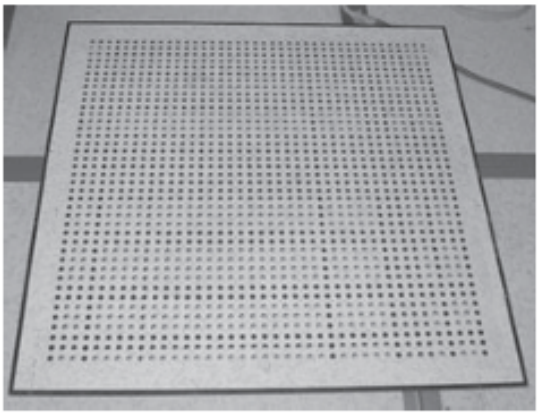

Figure 3.6: Perforated panel diffuser geometry, Zhang et al. [48].

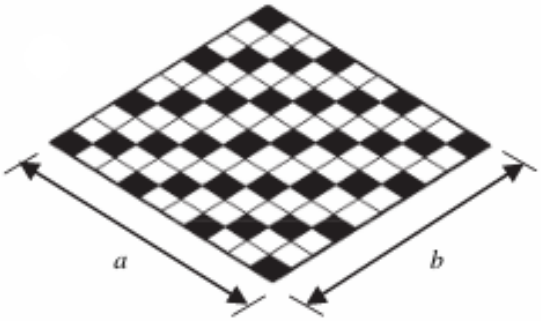

Figure 3.7: Schematic of the CFD random blocking method, where black cells are blocked and white cells are open, Zhang et al. [48].

Zhang et al. [48] impose the discharge air velocity at the cells, given by:

$$U_0 = \frac{\dot{m}}{\rho A_0} \tag{3.3}$$

where U_0 is the normal discharge air velocity, ρ the air density, A_0 the diffuser effective area, and $\dot{m}$ the mass flow rate. To better reproduce any swirling effects (unlikely in motorsport applications due to the absence of the fan) or different local airflow directions after the grille, multiple velocity components can be specified.

The model performance was validated in a workshop environment, and the CFD model showed good agreement with the experimental data, both in terms of air velocity and temperature stratification. However, since the study was performed on a ventilation system diffuser, the model was validated in an environment suitable for that purpose, with very low discharge velocities and different flow turbulence intensity from a typical motorsport application. The good correlation of the CFD with the experimental results is, hence, not a certain indication of good performance when used to simulate protective radiator grilles.

4

Experimental Simulation

It is crucial to validate the results obtained through the CFD simulations with experimental tests. Since this project will revolve around the blockage effect of the grille and its impact on the radiator, the setups investigated in this chapter are focused on the measurement of the pressure drop.

The most common testing rig used to evaluate the blockage effect of a radiator (which will also be used for this project) consists of having pressure probes on both sides of the radiator measuring the local total and static pressure, which can then be converted to a velocity (Hobeika et al. [12]).
The air is pumped towards the radiator through a fan, which also allows for modulation of the air velocity by changing its revolutions (Topuz et al. [39]).

Dallara performed a preliminary investigation for this project on how sensitive the test rig is in measuring the pressure drop across the protecting grilles (Barontini [3]). The study was done at an air temperature of 15 °C with airspeed from 6 to 22 $\mathrm{m\,s^{-1}}$. Each parameter was measured twice to test the repeatability of the results. The pressure is measured via pressure probes located before and after the test section.
Six different setups were tested, as shown in Figure 4.1 and Figure 4.2.

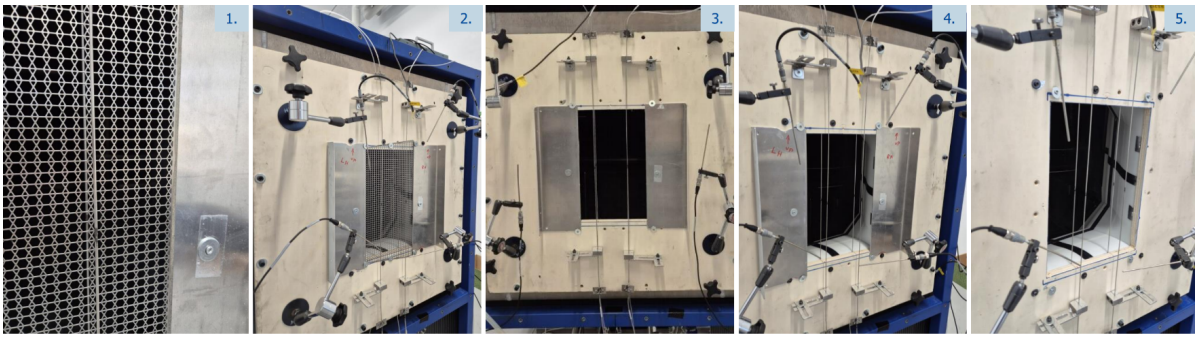

Figure 4.1: Grille configurations tested: (1) grille without duct, (2) grille with duct, (3) no grille no duct, (4) no grille with duct, (5) no grille with duct, no grille mounting strut, Barontini [3].

From the findings (Figure 4.3), it transpired that the presence of the duct helped reduce the pressure drop measured across the grille by about 6%. The presence of the duct allowed for a reduction of roughly 42% in static pressure

losses, probably due to the different velocity profile the flow exhibits in the test section when the duct is mounted compared to when it is not.

The pressure drop due to the strut supporting the grille was 150 Pa at a flow speed of 22 $\mathrm{m\,s^{-1}}$. Because the strut partially obstructed the opening, its presence indicates that any local constriction near the measurement location can substantially affect the accuracy and reliability of the recorded pressure values. This suggests that geometric shrinkage in the vicinity of the probes has a strong influence on measurement quality.

Figure 4.2: Grille 22425157, Barontini [3]

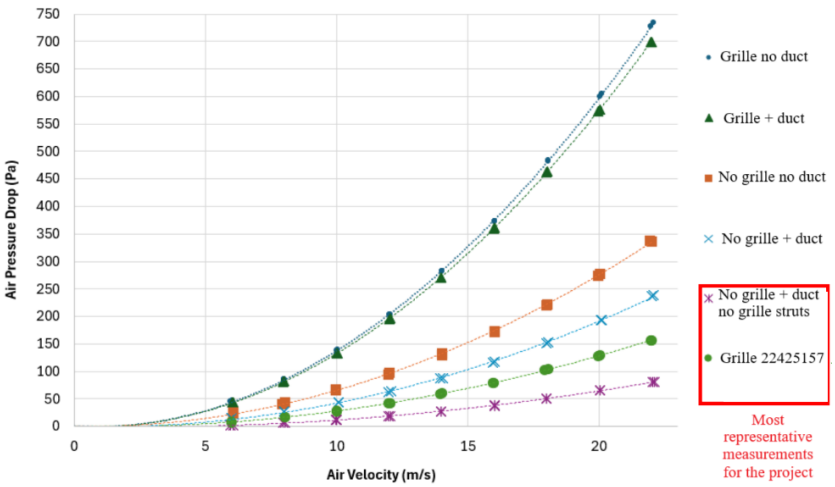

Figure 4.3: Pressure drop measurement, Barontini [3].

The last test, performed with the grille shown in Figure 4.2, is the most representative case in terms of pressure drop performance because the grille has a geometrical structure closer to the ones commonly used in motorsport applications. Compared to the first grille tested, this one leads to a significantly lower pressure drop, in the order of 150 Pa at 22 $\mathrm{m\,s^{-1}}$.

Even though the pressure drop is relatively small at this speed, the effect is not negligible at higher speeds, as the pressure drop has an exponential trend.

5

Literature Discussion

Overall, very limited information is available on the radiator and protective grille design related to motorsport applications. The majority of the findings were focused on everyday vehicle aerodynamic designs, which have different needs and performance goals. Not every aspect investigated can therefore be directly applied to the racing world, but it needs to be carefully analyzed to check which common points there are between the two worlds for every piece of information presented.

The majority of racing cars have an air duct channeling the air towards the radiator, hence limiting the losses and preventing the risk of having misplaced grille openings or upwashing issues as described in section 2.1. The concerns regarding this aspect will therefore not impact the design of the grille in this project, which focuses on motorsport applications, but they are of utmost importance in the case that the results of this study will be used for future applications in high-performance street-legal cars, which may not have a dedicated cooling air duct.
From the literature, it is clear that the grille has a disturbance effect on the flow, due to the struts partially blocking the flow and inducing vortex shedding and turbulence downstream, section 2.3. For cooling purposes, having a thoroughly mixed flow at the radiator inlet is more beneficial. The related knowledge presented applies to low Reynolds number flows; while the major effects are expected to be similar, the knowledge cannot be completely transferred to the motorsport world, where the Reynolds number is orders of magnitude greater.

The primary reason for having a grille in front of the radiator is to protect the radiator from any debris or rubber marbles that might reach that region during a race. The information gathered on their aerodynamic impact is focused on a double-wing element (section 2.2), making it impossible to draw conclusions on the loss of performance of a grille from this knowledge. It demonstrated the importance of not having debris in the most aerodynamically sensitive areas, which, for a grille, translates into the center region, far away from the walls. Designing and positioning the grille in a way that debris accumulation is limited is therefore of utmost importance.

The research presented in section 2.4 on the beneficial effect of the presence of a protective grille in front of a radiator is in a condition of forced flow, i.e., a fan is actively driving the air through the grille at a higher speed, resulting in a strong swirling motion.
Since fans are rarely used in the motorsport context, the flow is generally of better quality, with fewer swirls. As a result, the streamlining effect is reduced, and it may even hinder cooling performance by introducing additional pressure drop.

Both the opening size parameters and mesh geometry parameters influence the quality, direction, and amount of mass flow reaching the radiator (section 2.6). Overall, a strong positive correlation between mass flow through the grille and drag has been observed. The opening shape and size are often fixed in motorsport applications or leave very little room for modifications, hence it will not be the core of the grille design, although it must be kept in mind that maximizing the opening area is always preferred for enhancing the cooling performance.

The pieces of information known on the grille mesh parameters highlight the importance of minimizing blockage effects and prioritizing flow centralization (section 2.7). The strut size should be as small as possible while maintaining its structural integrity to protect the radiator from debris. The passage length could be used to direct the flow in the preferred direction for the radiator, provided that it does not cause excessive blockage. The grille's inclination should align with the incoming flow direction to limit the extension of the stagnation region in front of the grille. This effect is probably marginal for very thin grille struts (widely employed in motorsport applications); in such cases, the inclination of the grille could be beneficial for the collection of marbles.

The grille mesh geometry plays an important role in the mass flow passing through the grille. Using patterns that help focus the flow in the center is beneficial in terms of cooling performance. Although the trends observed seem reasonable, the differences measured are in the order of 10^{-3}, and no sensitivity analysis is provided. There is, therefore, some uncertainty regarding the reliability of the absolute values. The effects observed should hence be confirmed with CFD simulations.
Having a curved grille did not lead to benefits in terms of blockage. However, the case investigated involves flow losses between the radiator and the grille, due to the absence of an air duct. Since this project focuses on motorsport, where the flow is always channeled, it is worth investigating different configurations to be able to judge the best-performing one.
Furthermore, although the pressure drag induced by a square geometry is theoretically significantly higher compared to the one induced by a circular geometry, it remains important to validate that the same effect is seen also in terms of pressure drop across the grille, when using a circular wire compared to a square one.

5.1. Research Objective

Considering the lack of specific knowledge from published literature in the motorsport environment, the objective of this research is to identify and analyze all parameters involved in the grille design that may hinder the aerodynamic performance, considering the pressure drop, pressure distribution, and flow directionality across the grille and radiator. The study will also assess the extent to which the insights and findings available from the literature are transferable to racing contexts. Eventually, the aim is to parametrize the pressure drop across the grille by finding the relationship between all the parameters involved, and to find the optimal grille design which maximizes cooling efficiency, while conserving its protective function.
The research will be carried out through CFD simulations, whose results will be compared and validated with experimental tests performed in the test bench present at Dallara.

The best CFD model in terms of accuracy-to-cost ratio (which will be used throughout the project) is the RANS k-ω turbulence model (section 3.1). Initially, the aerodynamic analysis of the various grille configurations will be performed in CFD with the exact geometry, finely meshed to have the best accuracy possible on the results. The primary areas of focus will be the pressure drop and flow directionality, both at the grille level and at the radiator level, which then relate to the cooling efficiency.
The numerical results will then be correlated with the experimental data, which will indicate the accuracy of the CFD predictions. The correlated results will eventually be used to model the grille in a more simplified way to

reduce computational costs for future simulations.
The radiator will be modeled as a porous medium, as the accuracy of the results from the literature is reasonably low (subsection 3.2.2), and modeling it with the exact geometry would be too computationally expensive.

5.2. Research Questions

To narrowly define the relative importance of all parameters involved in the design of a protective grille within the motorsport context, three research questions will be presented. These will guide the project toward identifying an optimal grille design. The second and third research questions are broken down into sub-questions, which serve as a guide to answer the main research question. This design will then be simplified into a cost-effective representation suitable for future CFD applications, allowing it to simulate its aerodynamic effects without significant computational expenses.

1. ***Which parameters influence the pressure drop through a grille in motorsport cooling systems?***
2. ***What is the most effective way to model a grille in CFD, that balances computational cost and aerodynamic accuracy?***
    a) *How can a grille be modeled in CFD as a standalone component to accurately predict pressure drop with minimal computational cost?*
    b) *How can the standalone grille model be extended to include the radiator's influence on pressure drop while preserving computational efficiency?*
3. ***How can grille design be optimized to balance minimal pressure drop with effective cooling in motorsport applications?***
    a) *How does the distance between grille and radiator affect the pressure drop through the radiator?*
    b) *How does the distance between grille and radiator affect the pressure drop through the grille?*
    c) *Is using grille geometry to align the airflow with the radiator an effective strategy for reducing pressure drop over the radiator and increasing the cooling efficiency?*

II

Methodology

6

Simulation Setup

To ensure proper correlation between numerical and experimental results, the CFD model must replicate the test bench setup. This chapter details the numerical configuration, starting from the original layout (section 6.1), then explaining the rationale for a slightly modified configuration used to analyze the grille alone and the grille–radiator assembly (section 6.2 and section 6.3). Boundary conditions, mesh strategy, and volume refinements are outlined in section 6.4, followed by a near wall mesh sensitivity study in section 6.6.

6.1. Original Test Bench Setup

The firstly modeled test bench setup was a copy of the one physically present at Dallara; reproducing the same setup for the numerical simulations allows for properly correlating the CFD results with the ones obtained experimentally. The grille was mounted directly after the converging duct (Figure 6.1), fixed to the external wall of the test bench. The airflow was then allowed to freely expand beyond the grille.

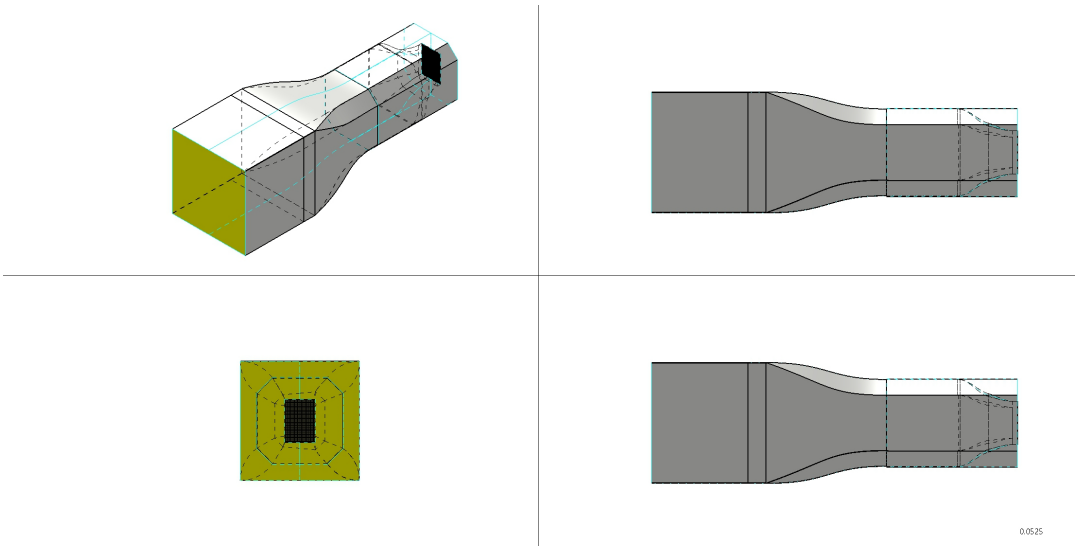

Figure 6.1: Original geometry test rig

The converging duct placed right in front of the test section to reduce the channel area to the size of the grille and limit the losses was not created on purpose for the project, but a pre-existing one has been used. Unfortunately, it is not symmetric (as seen in Figure 6.2). Its close position with respect to the test section was forced by the presence of the Pitot tubes, used to measure the speed of the flow upstream of the test section; since those are welded to the inner walls of the test bench, the duct had to be placed in the space remaining between them and the external wall, as shown in Figure 7.2.

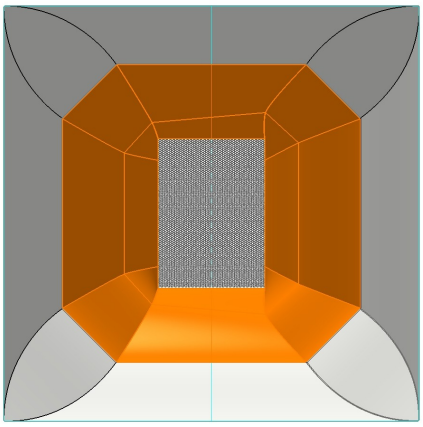

Figure 6.2: Duct asymmetry.

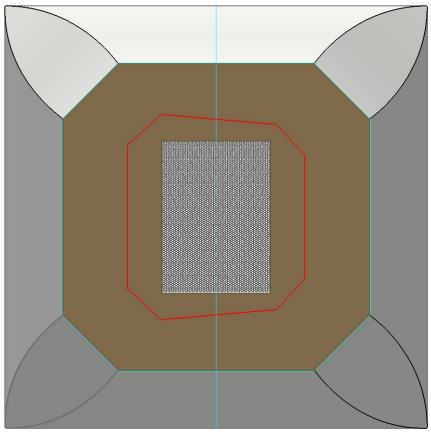

Figure 6.3: Front view test bench with grille.

The influence of the asymmetry on the results was tested both with and without the grille (”net 224” was used), measuring the static pressure in single points positioned at the converging duct exit, 20 mm upstream of the external wall where the grille is mounted (Figure 6.4 and Figure 6.5).

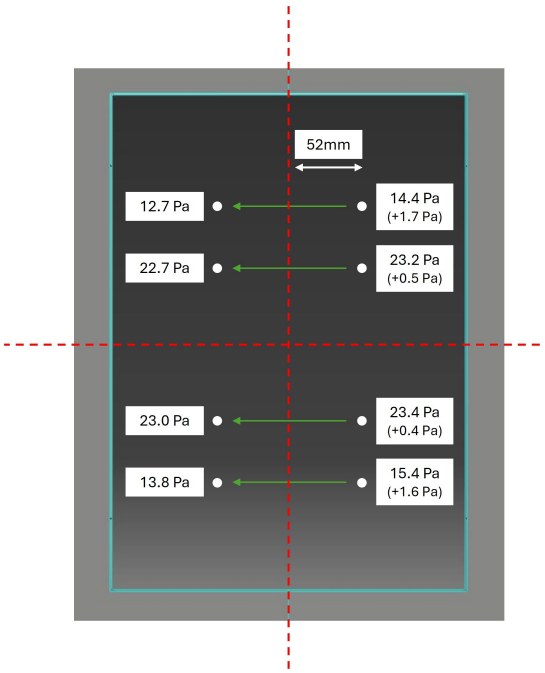

Figure 6.4: Static pressure distribution setup without grille, 20mm upstream of the external wall.

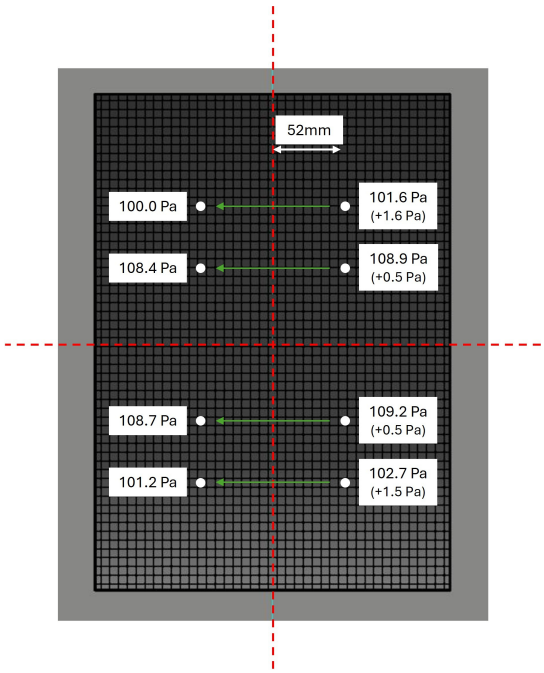

Figure 6.5: Static pressure distribution setup with ”net 224”, 20mm upstream of the external wall.

In both cases, on the right side, a slightly higher static pressure is registered, meaning the flow has a slightly lower speed in this region, according to Bernoulli's law, applicable to the flow in question, which is incompressible, steady, and without major viscous forces or heat transfer present:

$$p_{total} = \frac{1}{2}\rho V^2 + p_{static} \tag{6.1}$$

This effect is due to the asymmetry of the duct, and it's more visible in the points closer to the borders of the test section, where the difference between left and right side reaches a maximum value of 1.7 Pa. About the same absolute difference in static pressure readings is observed both with and without the grille, meaning the slight asymmetric effect remains invariant whether the grille is present or not. Considering the overall pressure read with the grille is around 100 Pa, the difference between left and right side accounts for only 1% of the total amount read, the effect of asymmetry in the flow can be considered to be negligible.

After some initial tests, some issues arose, leading to the decision of slightly modifying the test bench geometry to improve the quality and reliability of the results, as described in section 6.2. The key drivers of this choice were:

- From the numerical results, the distance between the end of the converging duct and the test section was too short (20 mm), preventing the central core of the flow from gradually adapting to the geometric contraction, thereby compromising the proper formation of the velocity profile. In the presence of a negative pressure gradient, the near-wall flow velocity (highlighted in Figure 6.6 by the yellow box), overshoots temporarily that of the stream core (Sauer [35], Kim [19]). The incorrect velocity profile is also testified by the static pressure readings shown in Figure 6.5 and Figure 6.4: the points closer to the core of the flow registered a higher value, signifying the flow has a lower velocity here compared to the region closer to the walls, according to Bernoulli's equation (Equation 6.1). Note that Figure 6.7 uses a finer velocity scale to better highlight the incorrect velocity profile immediately upstream of the grille.

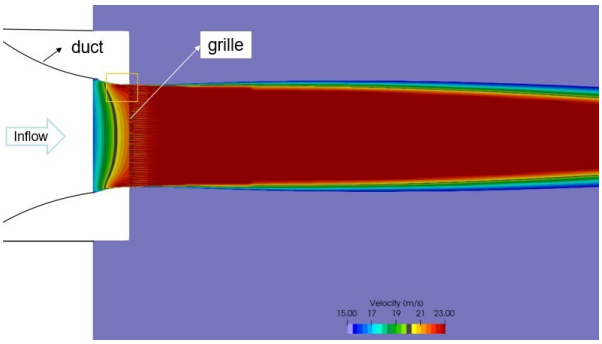

Figure 6.6: Side view flow velocity profile, original test bench setup.

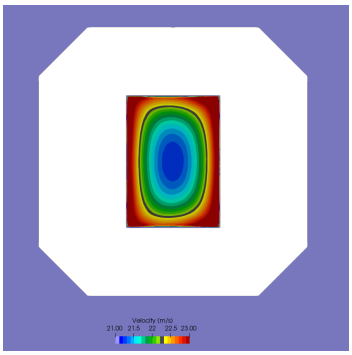

Figure 6.7: Front view flow velocity profile upstream of the grille, original test bench setup.

- Placing the grille on the exterior of the test bench causes the jet flow to expand immediately downstream, introducing additional losses in the system. Although these losses are subtracted from the pressure drop measured across the grille, the blockage effect of the grille, or even worse of the radiator, affects the jet expansion behavior. This interaction compromises the accuracy of the loss subtraction, potentially leading to an underestimation of the grille's actual pressure drop.
- Although the asymmetry effect described above in this section is limited, an elongated straight exit duct would allow the flow to mix and correct any asymmetry effect present at the end of the converging duct.

6.2. Simulation Test Bench Setup - Grille Alone

For the reasons mentioned in section 6.1, the test bench was modified, adding a 900 mm straight duct at the end of the converging duct. Its length was chosen only based on CFD considerations: the flow visually appeared to be sufficiently adapted with a 400 mm duct (Figure 6.9), and the remaining 500 mm were chosen taking into account ten times the characteristic length of the block grille plus radiator and leaving some extra margin for the studies on the influence of the distance between grille and radiator.
The design and dimensions of the selected duct were determined based on the feasibility of constructing it within the test bench, as a significantly longer duct would have been preferable from a purely aerodynamic standpoint. It would have also been preferable to design it slightly divergent, to limit the blockage effect of the boundary layer building up in the straight duct. This option was discarded because the time required to study and design the necessary divergence angle was considered excessive compared to the potential improvement in simulation accuracy.

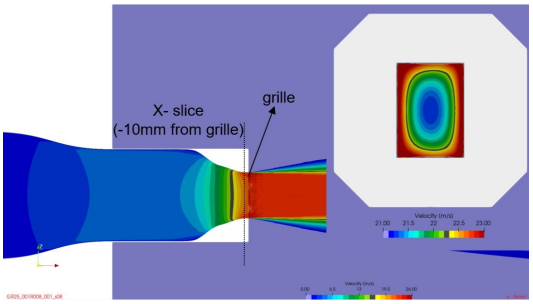

Figure 6.8: Velocity profile old test bench setup *(note the velocity scales in the two sections are scaled differently to better highlight the differences in flow velocity)*.

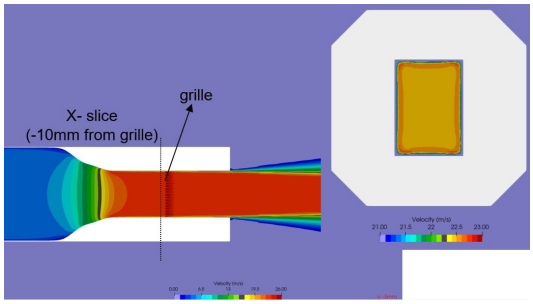

Figure 6.9: Velocity profile new test bench setup *(note the velocity scales in the two sections are scaled differently to better highlight the differences in flow velocity/.*

In order to have both a surface and volume mesh as clean as possible, preventing any degenerated cells from being created, all the surfaces present have been simplified and smoothed, while still preserving the characteristic dimensions of all components. An overview of the final setup used is shown in Figure 6.10.

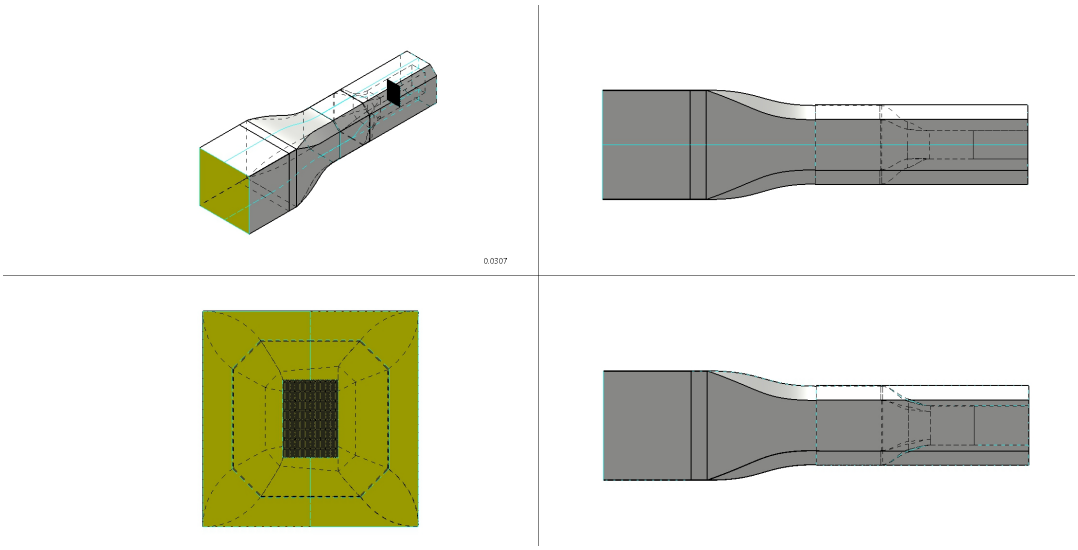

Figure 6.10: Simplified geometry test rig.

Since the test rig has a test section with a cross-sectional area significantly larger than the desired opening size, which matches the size of the radiator tested, a converging duct is added to the final part of the test section to channel the air towards the grille, avoiding pressure losses. In the simulation, the duct is sealed to the inner walls of the test bench. In the test bench, the duct it's a removable piece, so it has to have an opening size slightly smaller than the cross-section of the test bench to be easily mounted inside. To prevent any air from leaking outside, the gaps are sealed using metallic tape. Furthermore, immediately upstream of the grille, there are static pressure probes mounted on the wall of the test rig, between the converging duct and the end-wall. This gap is also sealed using metallic tape.
Although the gaps are sealed, applying tape does not improve the smoothness of the inner surface and may therefore introduce additional losses. These are theoretically removed experientially by measuring the pressure drop with the clean setup (i.e., without the grille), and then subtracting it from the pressure drop measured with the grille:

$$\Delta P_{static} = \Delta P_{static,\ grille} - \Delta P_{static,\ no\ grille} \tag{6.2}$$

The opening where the grille is located measures 360x257 mm. Even though in reality the grille is slightly wider than the test section opening, allowing it to be mounted on the external wall of the wind tunnel, it was sized to exactly match the dimensions of the opening for the simulations, to avoid any degenerated volume cells in the region between the grille and the external wall.

In the actual experimental setup, there are pressure probes located at both ends of the grille, which have not been reproduced in the geometry simulated for simplicity, as their intrusive action on the flow has been considered to be marginal. Having a simple geometry tested in CFD allows for limiting the number of elements to be meshed, reducing the total amount of volume cells needed, as well as avoiding any unnecessary regions where the volume cells might result in being degenerated.

Grille Modeled as Porous Medium

To preserve the aerodynamic influence of the grille while minimizing the computational effort required for detailed geometric simulation, the grille is most effectively modeled as a porous medium.

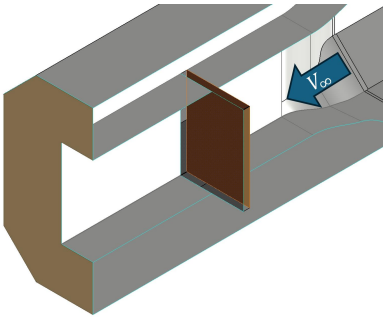

Figure 6.11: Inlet face, grille modeled as porous medium.

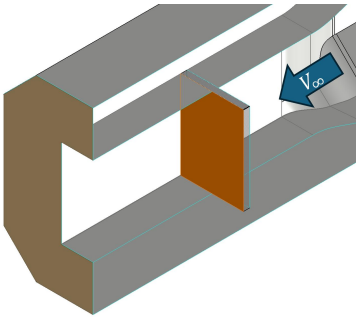

Figure 6.12: Outlet face, grille modeled as porous medium.

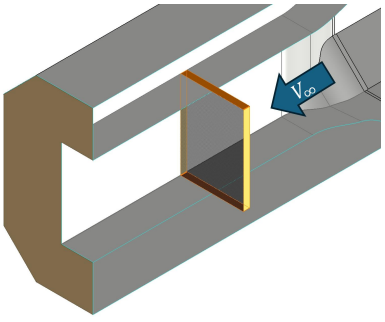

Figure 6.13: Frame, grille modeled as porous medium.

The porous medium is modeled in CAD as a rectangular parallelepiped, with an inlet (Figure 6.11) and outlet face (Figure 6.12) where the flow enters and leaves, respectively. The remaining faces compose the frame (Figure 6.13), which is modeled as a no-slip wall. The pressure drop is driven by the Forchheimer equation (Equation 3.2), depending on the local flow velocity immediately upstream of the inlet face of the porous medium. The

porous zone is defined by a local coordinate system (specifying the direction of flow resistance) and a pair of Forchheimer coefficients (K and β) that represent the pressure drop characteristics of the medium.

When the grille is represented with full geometric detail, the static pressure experiences a sharp drop across it, briefly undershooting the downstream static pressure level before gradually recovering to the correct value (Malico et al. [26]). In contrast, when the grille is modeled as a porous medium, the pressure drop is prescribed empirically as a function of the local flow velocity. Because of this imposed relationship, no downstream pressure recovery region forms; instead, the pressure decreases linearly across the porous block, as illustrated in Figure 6.14. Consequently, the porous medium must be assigned a thickness equal to the distance over which the actual geometry produces its adapted upstream to downstream static pressure change. In Figure 6.14, this thickness is 40mm.

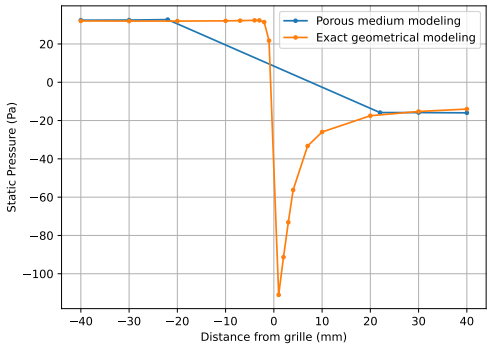

Figure 6.14: Difference in static pressure distribution between the case of porous medium and exact geometric modeling.

6.3. Simulation Test Bench Setup - Grille and Radiator

To test the influence the grille has on the radiator and vice versa, an additional configuration comprising the grille modeled geometrically and the radiator modeled as a porous medium has been tested. The setup is reported in Figure 6.15.

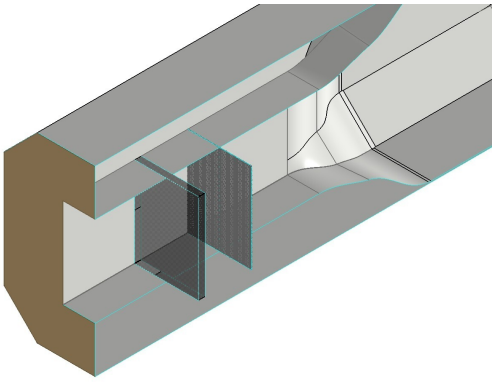

Figure 6.15: Grille plus radiator setup.

Across all the simulations performed adopting this setup, the grille location was always fixed at 400mm downstream of the end of the converging duct, while the radiator was moved within the space left inside the straight duct downstream of the grille.

Both the porosity curves of the cold and hot radiators used for the research were known. To balance the complexity of the simulation with the accuracy of the results, it was chosen to run the simulations as if they were cold, but adopting the porosity curve of the hot radiator, like in a real case scenario. From the hot curve shown in Figure 6.16, the viscous and inertial coefficients (K and β) were directly derived from a second order polynomial *least-squares* fitting of the curve.

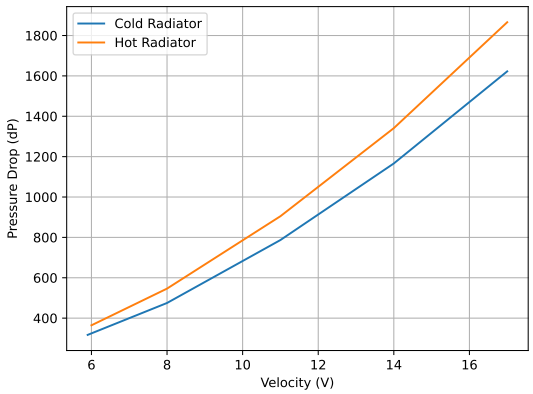

Figure 6.16: Comparison between hot and cold radiator performance.

6.4. Simulation Environment

One of the key aspects of a reliable CFD simulation is the definition of the simulation environment and boundary conditions. The construction of the former is always a trade-off between the amount of the available computational resources and its size. The latter ones define the physical problem, influencing the accuracy, numerical stability, and realism of the results.

6.4.1. Boundary Conditions

The boundary conditions must be applied far enough from the test section, such that they do not physically interfere with the physics of the tested objects in the test bench. To account for this, an external volume is added around the downstream portion of the test bench to represent the ambient environment. The resulting computational domain is composed of two connected regions: the external domain box and the internal volume of the test bench. Figure 6.17, 6.18, and 6.19 illustrate the boundary configuration adopted in the simulations.

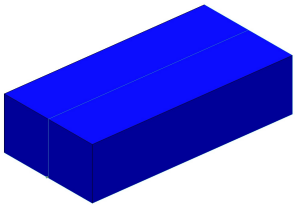

Figure 6.17: Simulation domain, sidewalls (blue).

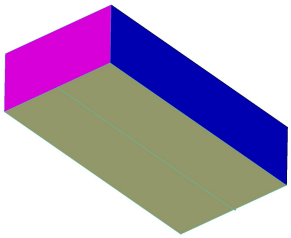

Figure 6.18: Simulation domain, pressure outlet (purple), ground (beige), sidewalls (blue).

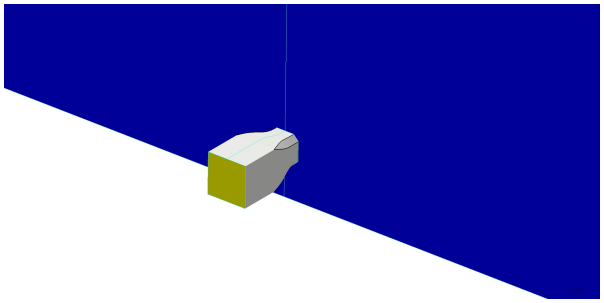

Figure 6.19: Inlet velocity boundary condition (yellow plane).

The domain box around the test bench measures 51.188x100x200 m (height x width x depth), with the mid-plane of the test bench placed 1188 m from the ground, like in the experimental setup. Having a large enough domain box is crucial to avoid any wall effect and to have a fully developed flow at the outlet. Its faces are divided into three areas: the ground, the sidewalls (blue faces in Figure 6.17), and the pressure outlet at the back (in purple in the picture above). The ground is treated as a no-slip wall, meaning that the flow velocity in the proximity of the wall is zero, and the sidewalls are treated as walls with slip. A zero□gauge□pressure condition is imposed at the outlet.

The inlet velocity boundary (the yellow plane in Figure 6.19) specifies the velocity of the flow entering the test section. In the experimental setup, the velocity near the grille is not measured directly. Instead, Pitot tubes positioned upstream of the converging duct, immediately ahead of the grille, record the flow speed inside the test bench. Given the target velocity at the test section where the grille is located, the corresponding flow velocity at the Pitot tube cross section is obtained by applying mass conservation:

$$\int_{A_1} \rho \vec{V}_1 \cdot \vec{n}_1 \, dA + \int_{A_2} \rho \vec{V}_2 \cdot \vec{n}_2 \, dA = 0 \tag{6.3}$$

where subscripts 1 and 2 denote the upstream (Pitot□tube) and downstream (grille) cross□sections, respectively. To apply this relation, the flow is assumed to be incompressible, steady, and one□dimensional, with a uniform velocity profile across each section.

In the CFD simulations, the inlet velocity plane is placed further upstream to allow the flow to develop into a physically realistic velocity profile before reaching the test section. As in the experimental analysis, mass conservation is used to determine the inlet velocity corresponding to the desired speed at the test section.

6.4.2. Surface Mesh Definition

The surface mesh size determines how accurately the geometry is represented in the simulation. A coarse mesh may distort the geometry, especially in regions where the geometry presents 90° angles, leading to inaccurate predictions of the flow behavior around the geometry. The surface mesh also defines the dimension and quality of the first layer of volume cells that grow away from the wall; highly degenerated cells might lead to poor quality volume cells, which might be a cause of numerical instabilities.

The amount of surface cells has to be carefully selected as it impacts the volume cell count, leading to an increase in computational time and resources required to resolve the flow field. For this reason, the geometry is divided into smaller sub-areas, each one having a different mesh refinement. The grille, for instance, is meshed with a very fine resolution to accurately capture the wire mesh geometry, whereas the surrounding duct walls are meshed an order of magnitude more coarsely due to their simpler shape. A smooth surface□refinement transition is used to move from the fine region to the coarser one, as illustrated in Figure 6.20.

In order to improve the overall mesh quality, all the geometrical features with an included angle equal to or smaller

than 90° were filleted. The radii were chosen small enough not to impact the overall aerodynamic behavior significantly.

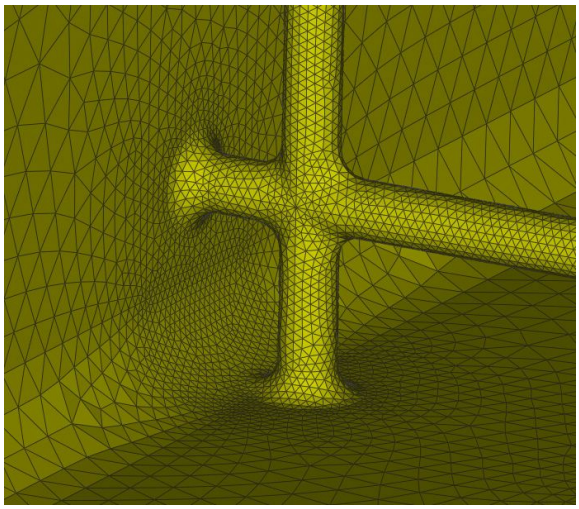

Figure 6.20: Grille surface mesh

6.4.3. Control Volume Cells

The computational field is divided into control volume cells, within which the conservation equations are solved. The resolution of the flow field depends on the size of these cells: the smaller they are, the more accurately the flow can be reconstructed. However, using very fine cells increases the total number of control volumes in which the equations must be evaluated, leading to a direct rise in computational cost. Fortunately, high resolution is only required in the grille region, where the pressure drop is computed, and flow separation occurs around the struts.

To address this, smaller volume refinement boxes are inserted within the domain, as shown in Figure 6.21, each defining the base cell size in its region. These boxes are nested and centered around the grille, with each box having a cell size twice that of the next finer one. This approach ensures a smooth transition from the smallest resolution to the coarsest one of 512 mm, which corresponds to the base resolution of the main domain box.

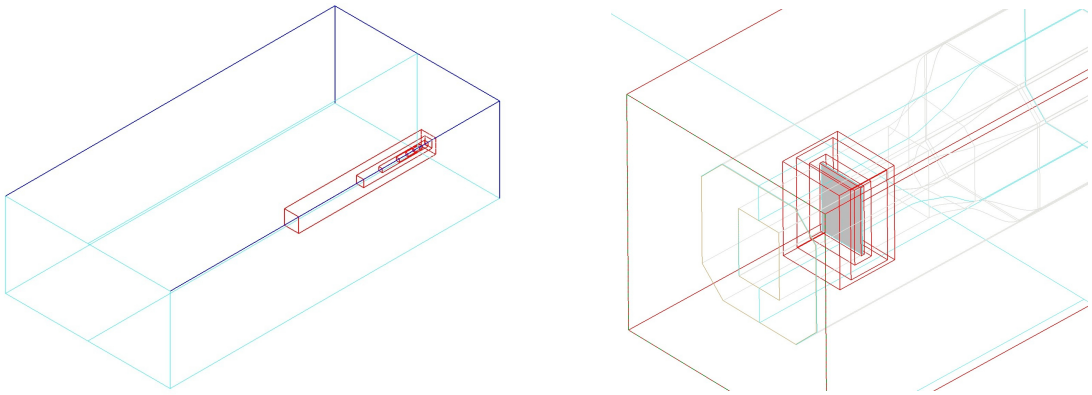

Figure 6.21: Volume refinement boxes (in red).

Each time the resolution of the refinement boxes is halved, the number of control volume cells within the box

decreases by a factor of 2^3. Initially, two resolution sizes for the smallest refinement box were considered: 0.5 and 0.25 mm. Both configurations featured a second smallest refinement box resolution of 1 mm. Among the reasons that led to the choice of the first one:

- In the original test bench setup, the smallest box with a resolution of 0.5 mm led to roughly 95 million cells, compared to the 198 million of the one using a resolution of 0.25 mm. Considering the large amount of numerical tests to be run, having a coarser resolution significantly reduces the resources needed to perform the analysis.
- Using a finer volume mesh means transitioning from 0.25 to 1 mm within a very short distance, resulting in a less gradual change. Combined with the larger mismatch between the surface cells of the walls around the grille and the volume refinement, this reduced the overall cell quality and made the simulation more unstable, increasing its tendency to diverge.
- The ”net 224” (Figure 9.1) with a square pattern (side of 5.8 mm) and circular strut cross section (diameter of 0.6 mm) returned similar results in terms of pressure drop across the grille when tested at 14 and 18 $\mathrm{m\,s^{-1}}$ with the 0.5 and 0.25 volume mesh resolution. The results have been collected using the original setup (Figure 6.1) and are shown in Figure 6.22. At an incoming average speed of 18 $\mathrm{m\,s^{-1}}$ the pressure drop predicted with the 0.5 mm refinement was 2.8 Pa (7%) higher compared to the 0.25 mm, a difference considered to be negligible. For this reason, the coarser resolution was chosen.

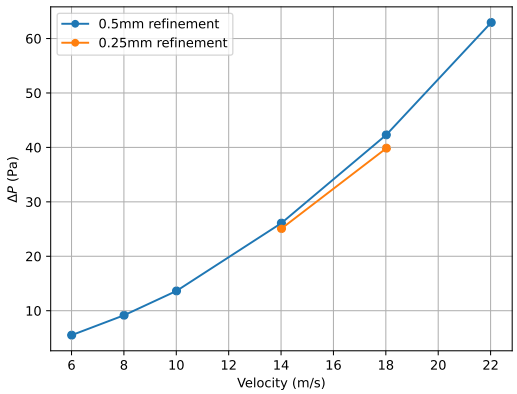

Figure 6.22: Results comparison for ”net 224” with 0.5 and 0.25 mm of volume mesh resolution with old test bench setup.

6.5. Simulation Residuals

To ensure convergence and proper relaxation in the results, all the runs have been computed as fully coupled pseudo-transient simulations in a steady state fashion.
The under-relaxation is obtained by introducing a pseudo time τ in the transport equation ([32]). Initially small time steps are used to relax the equation, once the simulation starts to converge, the time step is gradually increased.

The residuals from one of the runs obtained using this method are shown in Figure 6.23.

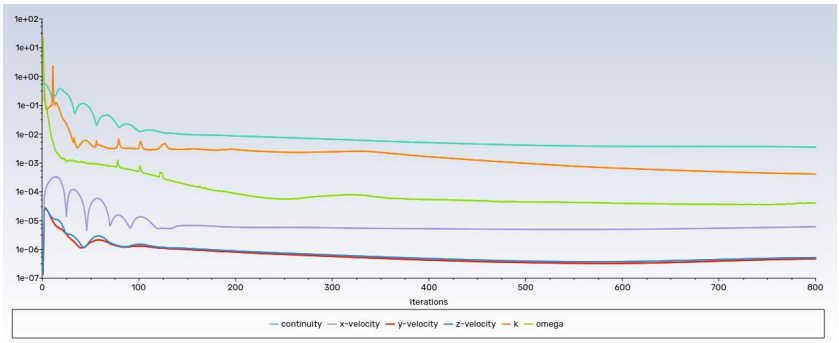

Figure 6.23: Residuals simulation

6.6. Near-Wall Mesh Resolution

When simulating the flow through a grille, the accuracy of the resulting pressure drop and wake turbulence depends heavily on how the fluid interacts with the solid surfaces. Because of the small scale sizes of the grille geometry, the gradients of flow velocity and pressure around the grille can be exceptionally high. To ensure the simulation captures these effects correctly, the non-dimensional wall distance y^+ is used to evaluate the suitability of the mesh:

$$y^+ = \frac{yu_\tau}{\nu} \tag{6.4}$$

where y is the distance of the first control volume cell from the wall, u_τ is the friction velocity, and ν is the kinematic viscosity of the fluid. If the y^+ is below 1, then the viscous sublayer is fully resolved, instead of approximating it using wall functions, which might fail to predict separation regions. This is fundamental, especially in the grille region, where the flow separates around the struts of the grille.
While a low value of y^+ is beneficial for the quality of the simulation, there are other aspects to carefully evaluate. The first is the aspect ratio (AR) of those cells:

$$AR = \frac{\Delta x_{tangential}}{\Delta y_{normal}} \tag{6.5}$$

When targeting a very low value of y^+, the first cell height is incredibly small. However, the longitudinal width of the cells is kept larger, to control the total cells count. This creates cells with a high aspect ratio, which in this region of high gradients might become a source of diffusion error, especially if the flow is not aligned with the volume cells. Furthermore, to limit any numerical jumps, a low volume cells growth rate should be kept, allowing for a smooth solution.

Looking closely at Equation 6.4, the only variable that can be actively controlled in the numerical simulation is the distance of the first control volume cell from the wall, y. Since no changes can be made to the geometry, the fluid, and the velocity inlet condition, both u_τ and ν are fixed. ANSYS Fluent, the software used for running all the numerical simulations, provides two options for generating the volume mesh in the proximity of the geometry walls: having a few layers of prism cells before transitioning to the hexagonal volume cells through the mosaic cells (Figure 6.25), or having the mosaic cells starting directly at the wall (Figure 6.26).

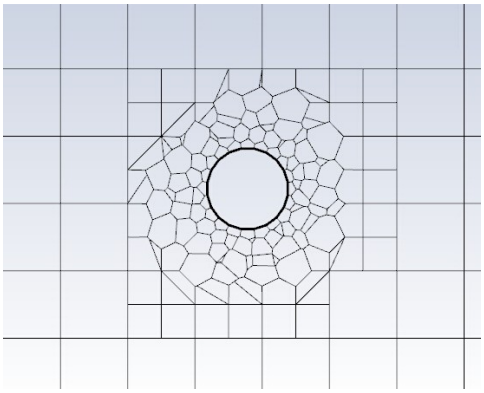

Figure 6.24: Volume mesh generation around the grille strut.

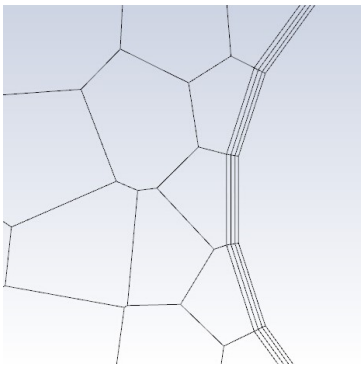

Figure 6.25: Volume mesh generation around the grille strut with prisms.

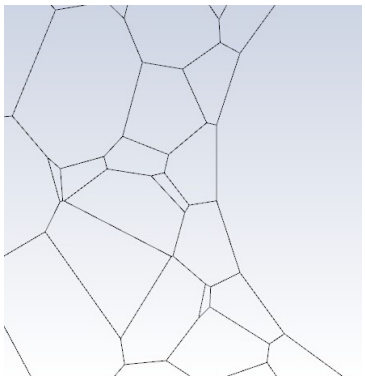

Figure 6.26: Volume mesh generation around the grille strut without prisms.

In the first case (Figure 6.25), the low height of the prisms allows for a significantly lower value of the y^+, allowing it to be below 1, as shown in Table 6.1. Since the y^+ depends directly on the flow speed, the investigation is performed at the highest speed that will be investigated in this study at the test section, 22 $\mathrm{m\,s^{-1}}$.

Configuration	**Max** y^+
With prisms	0.91
Without prisms	10.55

Table 6.1: Maximum values of y^+ on the grille, at test section velocity of 22 $\mathrm{m\,s^{-1}}$.

With the prism layers, the highest value of y^+ drops by a factor of 10, indicating that without them the mosaic cells would begin too far from the wall to properly resolve the near-wall gradients. Therefore, 3 layers of prisms will be grown from the grille's walls in all future simulations.

In the converging duct region, where the flow accelerates, the surface mesh resolution gets progressively coarser moving away from the frame of the grille. The prism layers present in this region are much taller to avoid having volume cells with an excessively high aspect ratio. As a result, the y^+ reaches a maximum value of around 10.6, at a test section speed of 22 $\mathrm{m\,s^{-1}}$. This means that in this region, wall functions are used to resolve the viscous sublayer; since it is a converging duct, with a negative pressure gradient, no flow separation is expected to occur, hence this value of y^+ is considered acceptable.

7

Experimental Testing Setup

To certify the accuracy of the numerical simulations, it is fundamental to experimentally measure the static pressure drop through the grille and through the block composed of the grille and radiator.
In section 7.1, the experimental setups used to test the performance of the grille alone are presented, in section 7.2 the setup used to measure the impact the grille has on the radiator and vice-versa, and finally in section 7.3 the setup used to evaluate the performance of the radiator alone is outlined.

7.1. Experimental Setup with Only Grille

The first configuration tested is the pressure drop across the grille. Two different setups were used to evaluate its performance: the original test bench, which is the standard configuration already present at Dallara, and a second setup with the addition of the 900 mm straight duct, which according to the numerical simulations should provide sufficient space for the flow to develop correctly.

7.1.1. Original Test Bench Setup

The setup, shown in Figure 7.1, presents a converging duct which channels the air towards the opening where the grille is mounted. Two symmetric static pressure probes are mounted upstream and downstream of the grille, allowing for the measurement of the difference in static pressure across the grille.

The converging duct is removable, so its wider side upstream is slightly smaller than the test section; furthermore, the duct is made up of four different pieces held together by screws, which introduce small hollow depths on its surface. Since any small opening is a potential source of error introducing a pressure loss, every imperfection was taped, as shown in Figure 7.2.
To adapt the opening area to match that of the grille, a wooden plate of 2 cm is mounted externally, on top of which the grille is mounted. The opening area of the wooden plate is slightly smaller than the downstream cross-section of the converging duct, and the small bump between the two is smoothed using some tape. In Figure 7.2, the Pitot tubes, which measure the freestream speed, are also visible. They are located right upstream of the converging duct; since the cross section of the test rig is larger than the test section opening, the software controlling the speed of the fan was adapted to impose a lower freestream velocity matching the desired speed at the grille opening, by

applying the law of conservation of mass.

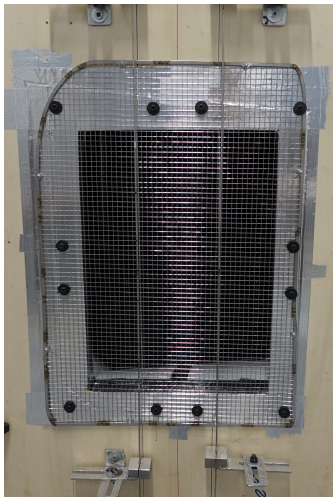

Figure 7.1: Experimental setup test rig with grille.

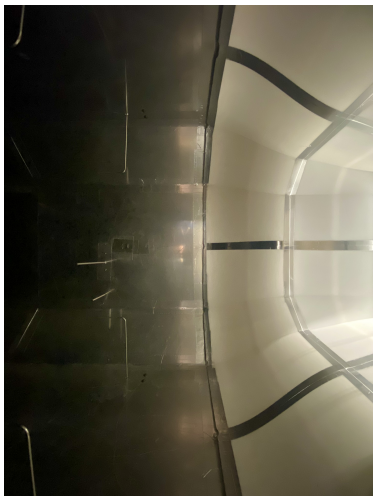

Figure 7.2: Converging duct taping.

The static pressure probes are small hollow tubes with tiny holes placed perpendicular with respect to the incoming flow, allowing them to measure the static pressure. Each probe contains four pairs of holes, and it is welded in the middle. This allows to split the single probe into two, and have twice as many static pressure readings. Each probe is connected through a plastic tube to a sensor, which directly computes the pressure difference read between two pairs of half probes (the upstream with the downstream counterpart). A total of four static pressure differences are measured each time.

7.1.2. Addition of the Extended Straight Duct

To overcome the uncertainty on the velocity profile of the flow at the test section, given the close distance between the converging duct and the grille, as explained in section 6.1, the same setup as the one used for the numerical simulation was constructed. The setup in quest comprised an extended duct of 900 mm, split into two separate components of metal sheet, one of 400 mm and of 500 mm (Figure 7.3). The two components are bolted together through their frame, and the grille is pressed in between.

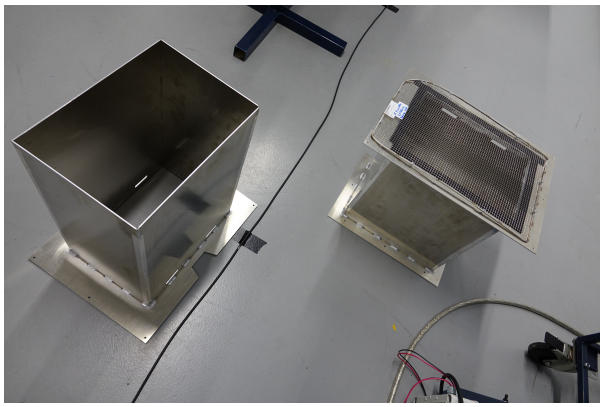

Figure 7.3: Straight ducts used in the new experimental setup.

To prevent the air from leaking out of the system, a foam tape was applied on the frame of both ducts, and the gap

between the two pieces was taped externally, as shown in Figure 7.4. The static pressure probes were mounted through slots appropriately carved out 20 mm upstream and downstream of the grille. The same configuration and convention shown in Figure 9.3 was used.

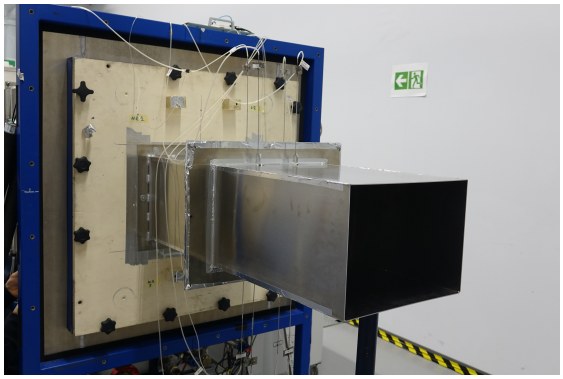

Figure 7.4: Extended straight duct addition.

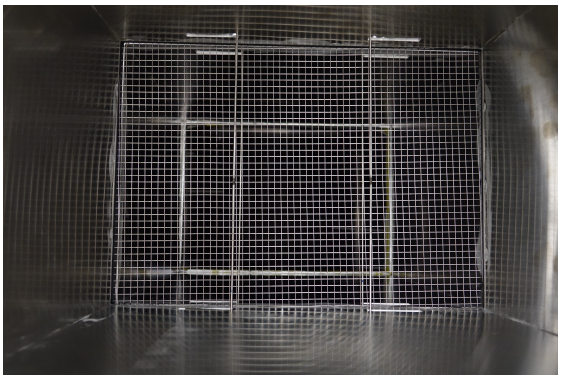

Figure 7.5: Extended straight duct, zoom into the mounting of the grille and static pressure probes.

Since this setup was thought after postprocessing the results of some initial tests, to better debug the system, additional hollow tubes were connected first upstream and then downstream of the grille to have a direct indication of the static pressure read on each side of the grille.

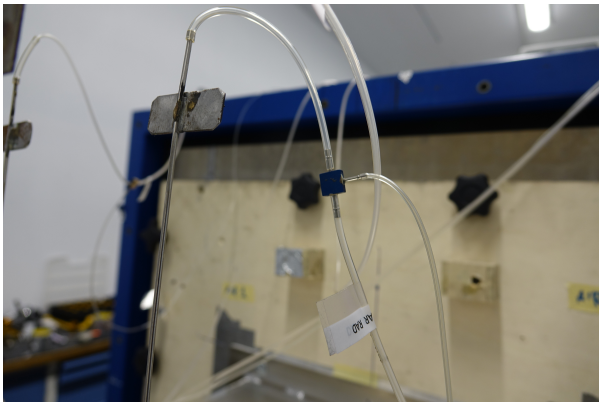

Figure 7.6: T-shaped static pressure tubes connection.

The static pressure sensor used during the tests described in subsection 7.1.1, only returned the difference in static pressure between the values read upstream and downstream of the grille, not giving information on the pressure read on either side of the grille.

7.2. Experimental Setup with Grille and Radiator

The grille in series with the radiator was also tested to experimentally investigate the impact the grille has on the radiator and vice versa. Due to logistical reasons, given the time constraints, only one distance between them was tested. The test bench setup was the same as described in subsection 7.1.1, with the difference that a radiator was also placed immediately downstream of the grille, and fixed to the wooden plate. They were distanced 5 mm apart; the choice was driven by the simplicity of the setup, as a wider distance between grille and radiator would have required a specific support for the radiator.

The whole setup was then sealed with some metallic tape to prevent the air from leaking outside. The static pressure probes for this test were mounted horizontally, as shown in Figure 7.7.

Figure 7.7: Grille + radiator setup.

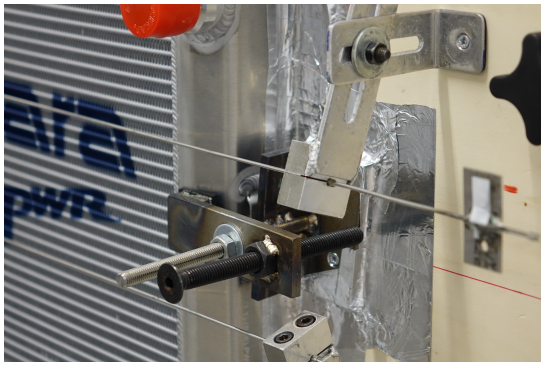

Figure 7.8: Static pressure probes supports.

At the time of the experimental tests, the thin radiator used in the preliminary simulations was not available. Consequently, a thicker radiator of 51 mm was used instead. Although the initial plan was to repeat the numerical simulations with the correct radiator, this was ultimately deemed unnecessary, as the experimental data did not provide sufficient reliability to justify additional computational effort.

7.3. Experimental Setup with Only Radiator

The radiator was also tested alone, to extrapolate the porosity curves and better understand the influence of the grille on the radiator.
When the test bench was originally designed at Dallara, it was intended primarily for radiator testing. Radiators typically exhibit a porosity approximately an order of magnitude higher than that of the grilles considered in this study, reducing the uncertainty in the results. Therefore, testing the radiator is also a potential way to extract the losses of the grille by subtracting the pressure drop read with the grille from the one read without it.

The setup used is very similar to the one shown in Figure 7.7, with the only difference that there is no grille upstream of the radiator.

8

Grille Parametrization

The first part of the project focuses on simulating the grille alone, to isolate and properly analyze its effect on the flow in terms of pressure drop. Once an initial study on the grille alone has been performed, the radiator (modeled as a porous medium) is added to the simulation to investigate the impact the radiator has on the grille and vice versa.
Deriving a formula that accuracy predicts the porosity curve based solely on the geometric characteristics of a grille enables the immediate and quantified preliminary estimation of its aerodynamic performance. This, in turn, enables a more informed evaluation of different grille designs and facilitates the selection of the most suitable option.

8.1. Test Matrix

This section collects all the parameters tested to analyze the effect of different grille configurations on the static pressure losses, as well as the tested combinations of grille and radiator to investigate how they influence each other.

8.1.1. Grille Test Matrix

Multiple combinations of grille parameters were tested and compared: the geometry of the pattern, opening size, cross-section shape, and passage length of the wire, and different inclinations with respect to the incoming flow. Each geometry change was tested while keeping all the other parameters constant (i.e., when changing the thickness of the wire, the grille pattern consisted of square openings of constant width). This way, the influence of the single parameter on the pressure drop can be better isolated. All the parameters tested on the grille alone are shown in Table 8.1, 8.2 ,8.3, and 8.5. The influence of all the single geometrical parameters was tested using the square grille, as it is the easiest shape to mesh in CFD.
The performance of the grilles was evaluated at a range of speeds[1] from 6 to 22 $\mathrm{m\,s^{-1}}$, measuring every 4 $\mathrm{m\,s^{-1}}$. This range of low speeds was chosen because cooling is more critical at low speeds, where the mass flow rate reaching the radiator is limited, and the heat transfer rate is at its minimum. Having a precise mapping of the

[1]The range of speeds mentioned refers to the velocity of the flow before the convergent duct, where it is measured by the Pitot tubes.

impact of the grille on the flow at these velocity ranges is critical, as underestimating its effects might lead to insufficient cooling and overheating of critical components of the vehicle.

Parameters Investigated	Values Tested
Velocity $[\mathrm{m\,s^{-1}}]$	6, 10, 14, 18, 22
Wire diameter $[\mathrm{mm}]$	0.6, 0.8, 1.0, 1.2
Hydraulic diameter $[\mathrm{mm}]$	3.5, 4.2, 5.7, 7.1
Passage length $[\mathrm{mm}]$	5, 10
Wire cross section	round, squared

Table 8.1: Square mesh, parameters tested.

Parameters Investigated	Values Tested
Velocity $[\mathrm{m\,s^{-1}}]$	6, 10, 14, 18, 22
Wire diameter $[\mathrm{mm}]$	0.6
Hydraulic diameter $[\mathrm{mm}]$	4.0, 4.2
Wire cross section	round

Table 8.2: Triangular mesh, parameters tested.

Parameters Investigated	Values Tested
Velocity $[\mathrm{m\,s^{-1}}]$	6, 10, 14, 18, 22
Wire diameter $[\mathrm{mm}]$	0.6
Hydraulic diameter $[\mathrm{mm}]$	4.2, 5.2
Wire cross section	round

Table 8.3: Hexagonal mesh, parameters tested.

Parameters Investigated	Values Tested
Velocity $[\mathrm{m\,s^{-1}}]$	6, 10, 14, 18, 22
Wire diameter $[\mathrm{mm}]$	0.6
Hydraulic diameter[2] $[\mathrm{mm}]$	4.2, 5.6
Wire cross section	round

Table 8.4: Octagon+square mesh, parameters tested.

Parameters Investigated	Values Tested
Velocity $[\mathrm{m\,s^{-1}}]$	10, 14, 18, 22
Wire diameter $[\mathrm{mm}]$	0.6
Hydraulic diameter $[\mathrm{mm}]$	4.2
Wire cross section	round

Table 8.5: 45° rotated square mesh, parameters tested.

Figure 8.1, 8.2, 8.3, and 8.4 give a visual overview of the geometries mentioned above.

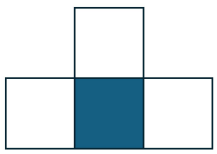

Figure 8.1: Square mesh pattern.

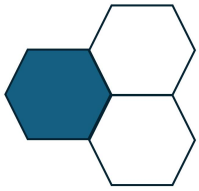

Figure 8.2: Hexagonal mesh pattern.

Figure 8.3: Triangular mesh pattern.

Figure 8.4: Octagonal+square mesh pattern.

8.1.2. Grille+Radiator Test Matrix

To fully assess the performance of a grille, it is not sufficient to analyze it as an isolated component. The grille is designed to be installed upstream of the element it protects; therefore, its behavior is influenced by the surrounding geometry and the downstream system. For this research, the protected component is the radiator, meaning that the grille's aerodynamic and thermal performance must be evaluated in conjunction with the radiator and its immediate environment. The two aspects that have been investigated are the effect of the distance between the grille and the radiator and the use of the grille to give a certain directionality to the flow, to better align it with the orientation of the radiator. The cases tested are collected in Table 8.6.

[2]The hydraulic diameter refers to the one of the octagon

Parameters Investigated	Values Tested
Velocity [$\mathrm{m\,s^{-1}}$]	22
Wire diameter [mm]	0.6
Hydraulic diameter [mm]	4.2
Wire cross section	round, airfoil[3] (30°), airfoil (15°)
Distance grille-radiator [mm]	2.5, 5, 10, 20, 50, 100, 200

Table 8.6: Square mesh and radiator, parameters tested.

8.2. Parametrization Methodology

One of the key goals of the research is to model the grille numerically in a simplified manner, reducing the burden of the computational time, cost, and complexity of simulating a grille with its exact geometry. Since the radiators are modeled using the porous medium approach at Dallara, using the same method to model the grille allows to easily adapt it into the automated CFD process. As described in section 3.2, the static pressure drop is governed by the Forchheimer equation (Equation 3.2), where the parameters are adapted according to the porosity of the modeled medium.

8.2.1. Base Parametrization Model

Since the numerical simulations return discrete data, the differential term $\frac{dp}{dx}$ in Equation 3.2 needs to be explicit as:

$$\frac{\Delta p}{\Delta x} = \frac{\mu}{K} V + \rho \beta V^2 \tag{8.1}$$

where Δx is the thickness of the grille, V is the superficial velocity (Tupin et al. [40]), μ is the dynamic viscosity of air (1.7894e-05 $\mathrm{kg\,m^{-1}\,s^{-1}}$ in the simulations), ρ is the fluid density (1.177 $\mathrm{kg\,m^{-3}}$ in the simulations), K is the permeability coefficient and β is the Forchheimer coefficient. The latter two parameters can be further broken down according to the formulations presented in Table 3.2. All the formulations contain coefficients that were originally derived from datasets that differ from this specific application; for this reason they have been recalculated using a *least-squares* fit based on the CFD data obtained at 6, 10, 14, 18, and 22 $\mathrm{m\,s^{-1}}$ for the square grille with circular wire, first varying one parameter (either the side length of the square or the wire thickness) while keeping all the other parameters constant, and then varying the other. All the coefficients that followed from empirical considerations were kept the same.
The static pressure drop across the various grilles was evaluated as the difference between the mean static pressure measured on two planes, each as wide as the duct, located 20 mm upstream and 20 mm downstream of the grille, shown in pink in Figure 8.5. At this distance, the static pressure showed, on average, an almost complete recovery, making the pressure drop measurement distance consistent with the porous medium approach, as shown in Figure 6.14.

The performance of the various models has been evaluated, fitting the respective coefficients with half of the data points, and comparing the average root squared error (RMSE) (Equation 8.2) between the predictive model and the entire data set available (35 data points). Training the models on incomplete data (20 points out of 35), and then testing their performance on everything, allows to check how effectively the models behave when they're missing information. Testing the generalization of the models is very important as they need to be used

[3]The grille was shaped like an airfoil; the degrees indicated refer to the angle the tangent line to the mean chord makes at the trailing edge with the horizontal. The radiator was inclined 30° with respect to the horizontal when testing the performance of the airfoil-shaped grille

for whatever combination of grille geometry, and the final fitting of the coefficients will be made solely on the available data collected from CFD, which is limited. The selected data points were those in the middle of the range, rather than the extremes (ten points were selected from the grille analysis focused on wire thickness, and another ten from the analysis investigating the opening size). For example, if the wire thickness values are 5, 6, 8, and 10, only the grilles having wire thicknesses of 6 and 8 were considered. In principle, any data point could have been chosen for this comparison, without affecting the results.
The RMSE is defined as:

$$\text{RMSE} = \sqrt{\frac{1}{n}\sum_{i=1}^{n}(d_{p_i} - \hat{d}_{p_i})^2} \tag{8.2}$$

where d_{p_i} is the actual value of the i-th static pressure drop, and $\hat{d}_{p_i}$ is the predicted value. The RMSE performance of the models considered is collected in Figure 8.7.

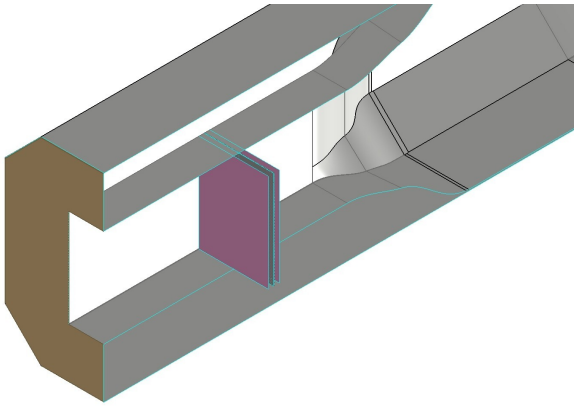

Figure 8.5: Static pressure measure planes (in pink) 20mm upstream and downstream of the grille.

Formulation	**Mean RMSE** [Pa]
Du Plessis et al. [7]	32.560
Dukhan et al. [9]	5.617
Calmidi [4]	2.680
Dukhan [8]	12.350
Ergun [10]	24.720
Yang et al. [43]	9.199

Table 8.7: Average root mean squared error (RMSE) of the entire data-set predicted with different Forchheimer (β) and permeability (K) coefficients formulations.

The best performing model in terms of RMSE resulted being the formulation of Calmidi [4] for K and β, which can be rewritten as:

$$\frac{1}{K} = D_h^2 \cdot C_v(1-\epsilon)^{n_1}\left(\frac{d}{D_h}\right)^{q_1} \tag{8.3}$$

$$\beta = C_i \frac{(1-\epsilon)^{n_2}\left(\frac{d}{D_h}\right)^{q_2}}{\sqrt{K}} \tag{8.4}$$

where n_1, n_2, q_1, and q_2 are empirical coefficients, $D_h = \frac{4A}{P}$ is the hydraulic diameter, d is the diameter of the grille's wire, ϵ is the porosity of the grille (ratio of open to total area of the duct $\frac{A_{open}}{A_{total}}$). As discussed by Calmidi [4], the parameters involved are not arbitrary: $(1-\epsilon)$ mimics the behavior of the flow as ϵ approaches unity, and $\frac{d}{D_h}$ allows for capturing the effect of the wire diameter and of the hydraulic diameter on the losses.
Substituting the values of the coefficients found with the *least-squares* fitting of the entire data-set available for the best accuracy possible, Equation 8.3 and Equation 8.4 become:

$$\frac{1}{K} = D_h^2 \cdot 0.4868(1-\epsilon)^{1.2397}\left(\frac{d}{D_h}\right)^{0.7780} \tag{8.5}$$

$$\beta = 1.6342 \frac{(1-\epsilon)^{-0.5331} \left(\frac{d}{D_h}\right)^{1.6254}}{\sqrt{K}} \tag{8.6}$$

The Forchheimer equation is composed of the sum of the viscous (AV) and inertial (BV^2) contributions of the flow to the static pressure drop:

$$\frac{\Delta p}{\Delta x} = \frac{\mu}{K} V + \rho \beta V^2 = AV + BV^2 \tag{8.7}$$

As the freestream speed of the flow in the simulations becomes higher, the inertial contribution to the pressure drop becomes predominant. This effect can be better visualized by looking at the change in static pressure coefficient as the flow speed in the test section increases from 6 to 22 $\mathrm{m\,s^{-1}}$ (Figure 8.6):

$$c_{p_{static}} = \frac{p_{static} - p_\infty}{\frac{1}{2}\rho V_\infty^2} \tag{8.8}$$

Since $c_{p_{static}}$ normalizes the difference between static and freestream pressure by the square of the velocity, the inertial contribution (associated with V^2) is effectively removed. This makes the resulting $c_{p_{static}}$ graphs independent of dynamic pressure, highlighting variations due to viscous effects rather than changes in flow speed. In Figure 8.6, the drop in static pressure coefficient across various grilles with different open area ratio values (ϵ) is shown at increasing freestream flow speed. As expected, the curves get closer to each other as the flow velocity increases, demonstrating the gradual loss of impact of viscous effects on the static pressure drop.

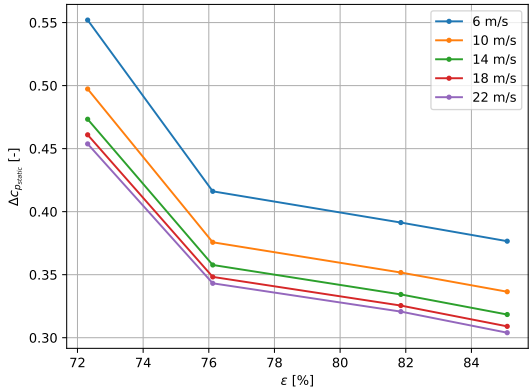

Figure 8.6: Static pressure coefficient drop across grilles with varying porosity.

8.2.2. Model Adaptation to Different Mesh Geometries

To extend the model described in subsection 8.2.1 to different mesh geometries, it is necessary to establish a common metric for comparison. This ensures that any variation in the results is solely due to the geometrical shape.

Three geometries were considered: the equilateral triangle, square, and regular hexagon as they are easily manufacturable and can be arranged into repeating patterns. The meter chosen was to consider grilles with the same hydraulic diameter (D_h), as they showed similar porosity (ϵ) values (Figure 8.7). If the material, dimension, and shape of the wire are the same, then any difference in the static pressure drop seen among grilles with an equal porosity is to be attributed to the difference in the geometrical structure of the mesh.

The hydraulic diameter chosen to perform the parametrization was selected randomly, and it was equal to $0.0042\mathrm{m}$.

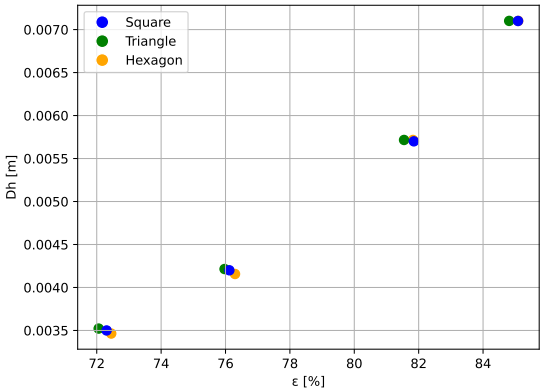

Figure 8.7: Porosity (ϵ) given a hydraulic diameter (D_h) for unit mesh shapes as: square, equilateral triangle, and regular hexagon.

To quantify the geometrical effect, the pressure drop curve of a given geometry is divided by that of a reference geometry, yielding a factor S, referred to as the shape factor. From the postprocessing of the CFD data, the shape factor resulted in being a second-order polynomial depending on the freestream flow velocity V:

$$S = \frac{\Delta p_{geometry}}{\Delta p_{ref.geometry}} = AV^2 + BV + C \tag{8.9}$$

where A and B have very low values as the polynomial has a very light curvature. By multiplying Equation 8.1 by S, then the pressure drop curve of the grille with the same porosity but different geometry is found:

$$\frac{\Delta p}{\Delta x} = S \cdot \Delta p_{ref.geometry} = S \cdot \left(\frac{\mu}{K_{ref,geometry}} V + \rho \beta_{ref.geometry} V^2 \right) \tag{8.10}$$

In order to parametrize the coefficients A, B, and C based on the geometrical parameters of the various mesh shapes, a few observations must be made first:

- As the number of sides of a regular polygon increases, the angle between two adjacent wires also increases, reaching a maximum value of 180° in the limiting case of a circle. However, a circle cannot form a discrete wire pattern, since it has no individual sides. The relative positioning of the wires is not captured by the porosity value, which only indicates the percentage of the duct's cross-sectional area that is unobstructed. When the flow encounters a wire, a static pressure build-up occurs near the stagnation point, creating resistance to the flow. If the angle between two adjacent wires is very small, two stagnation regions will be close to each other, forcing the flow to pass through the remaining open area where resistance is lower. This effect increases the static pressure losses across the grille.

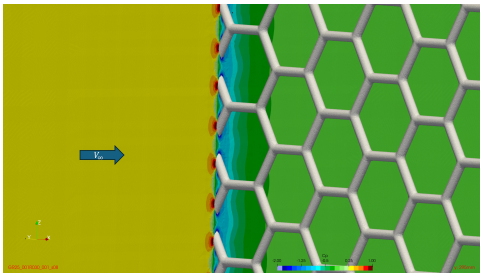

Figure 8.8: Static pressure coefficient distribution around hexagonal mesh.

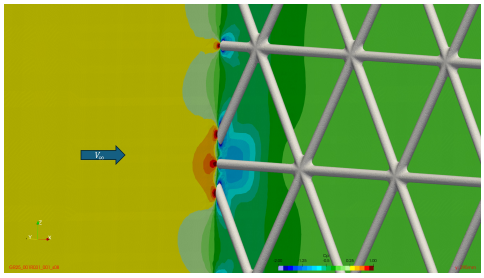

Figure 8.9: Static pressure coefficient distribution around triangular mesh.

Figure 8.8 and 8.9 visually show the larger static pressure build up present in the triangular mesh, where the spacing between two adjacent struts is reduced.
This information indicates that the static pressure drop curve for a geometry with fewer sides will consistently exhibit greater blockage. The behavior of S is as follows:

$$S > 1 \text{ if } n_{sides,geometry} < n_{sides,ref.geometry}$$

$$S < 1 \text{ if } n_{sides,geometry} > n_{sides,ref.geometry}$$

- As the freestream velocity of the flow approaches zero, the pressure drop will tend to zero as well, and the shape factor S will approach unity. As a result, whenever S is above one, the second-order polynomial will have a negative value of A (concave down); if it is below one, then the opposite is true ($A < 0$ and S concave up), as shown in Figure 8.10.

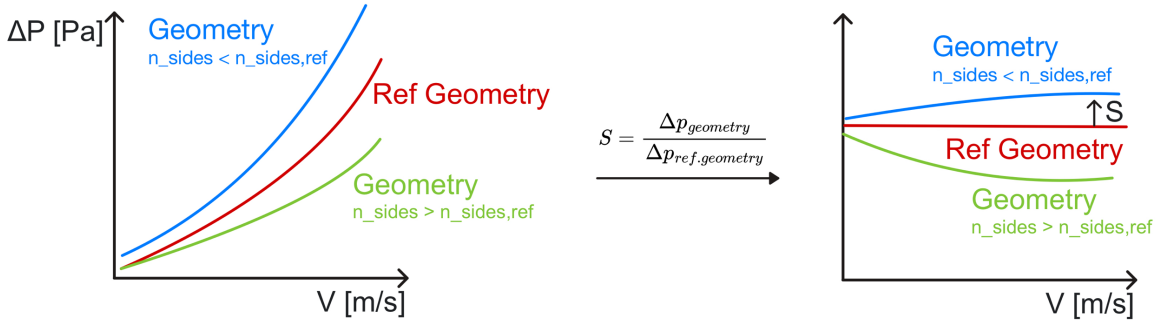

Figure 8.10: Schematic overview of the shape factor.

These two observations highlighted that the switch of sign of A is directly linked to the number of sides of the polygon considered, and that the increased pressure drop is linked to the angle between two adjacent wires, and led to the identification of these two base parameters that constitute the foundation of the modeling of the shape factor, the angle factor AF, and the perimeter factor P:

$$AF = 1 - cos(\theta) \tag{8.11}$$

$$P = 1 - \frac{P_{geometry}}{P_{ref.geoemtry}} \tag{8.12}$$

Since all the geometries considered for this study are regular polygons with equal internal angles, θ has always been considered to be the average internal angle of the polygon. This assumption has not been confirmed to hold for different geometries where the internal angles do not have all the same opening.
The angle factor AF has been chosen as such for two main reasons:

- $cos(\theta)$: using the sine function would result in identical values for multiple angles. For instance, both an equilateral triangle and a hexagon would yield the same result since $sin(60°) = sin(120°)$, which is undesirable.
- $1 - cos(\theta)$: since θ can only assume values between 0° and 180°, its cosine will always be positive, ranging between 0 and 2. This is advantageous because it isolates any sign changes to the perimeter factor P, thereby reducing the number of combinations that need to be tested during the parametrization.

The perimeter factor P will be negative when the geometry has fewer sides compared to the reference geometry, and positive when it has more. This allows for easy control of the switch of sign needed to correctly model the direction of the parabola's concavity.

Although the shape factor behaves as a second-order polynomial with respect to the freestream speed, there is no direct correlation between the quadratic term and inertial effects, nor between the linear term and viscous effects. This is because S results from dividing two quadratic pressure-drop curves, where the corresponding effects cancel each other out, eliminating any physical relationship.

The most accurate representation of the shape factor was obtained by modeling the coefficients A,B, and C as follows:

$$C = 1 + m_1 \cdot AF^{m_2} \cdot P \tag{8.13}$$

$$B = m_3 \cdot AF^{m_4} \cdot P \tag{8.14}$$

$$A = m_5 \cdot AF^{m_6} \cdot P \tag{8.15}$$

where m_1, m_2, m_3, m_4, m_5, and m_6 are the coefficients to be fitted with the CFD data.

Rewriting the equations above with the explicit fitted empirical coefficients, using as reference geometry the one of the square, becomes:

$$C = 1 - 0.1935 \cdot AF^{0.0772} \cdot P \tag{8.16}$$

$$B = 0.8747 \cdot AF^{-0.0109} \cdot P \tag{8.17}$$

$$A = 0.5692 \cdot AF^{0.0002} \cdot P \tag{8.18}$$

The modeled shape factor compared to the one computed from CFD data is shown in Figure 8.11. The absolute deltas between the actual and modeled shape factors are all in the order of 10^{-3}, as highlighted in Figure 8.12, indicating an almost exact match.

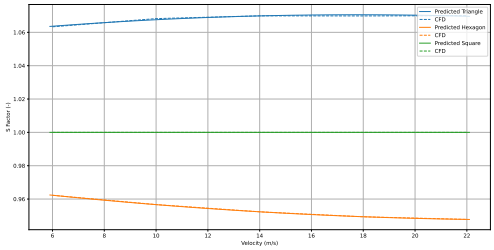

Figure 8.11: Shape factor modeled versus the one computed from CFD data, using the square as reference geometry.

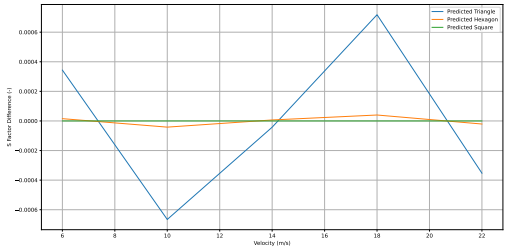

Figure 8.12: Shape factor model error compared to the one computed from CFD data, using the square as reference geometry.

Modeling in CFD

To produce the grille-specific static pressure drop curve, the presented model requires as inputs all the parameters summarized in Table 8.8, which can all be derived from the geometrical construction of the grille.

Variable	Unit
Wire thickness	m
Hydraulic diameter	m
Porosity $\left(\frac{A_{open}}{A_{total}}\right)$	-

Table 8.8: Inputs required by the static pressure drop curve model developed.

The model only holds for wires with circular cross-section, as the square one introduced additional losses in the system, at equal geometrical construction of the grille, as described later in subsection 10.1.2. While the wire thickness and hydraulic diameter can be easily computed, the porosity ϵ would require the physical modeling of the grille in a CAD software to measure the ratio of open area to total area occupied by the grille. Although this remains the most accurate way of computing this parameter, an estimation can be done as follows:

$$\epsilon = \frac{A_{geometry\ without\ frame}}{A_{geometry\ with\ half-frame}} \tag{8.19}$$

where $A_{geometry\ without\ frame}$ refers to the area highlighted in blue in Figure 8.13, while the $A_{geometry\ with\ frame}$ refers to the one highlighted in red. Note that for simplicity, the two areas have been shown on a square, but the same idea can be extended to whatever geometry is considered. This estimation does not account for the borders of the grille, which may cut the unit patterns, leading to a slight deviation of the porosity estimated from the physical modeling.

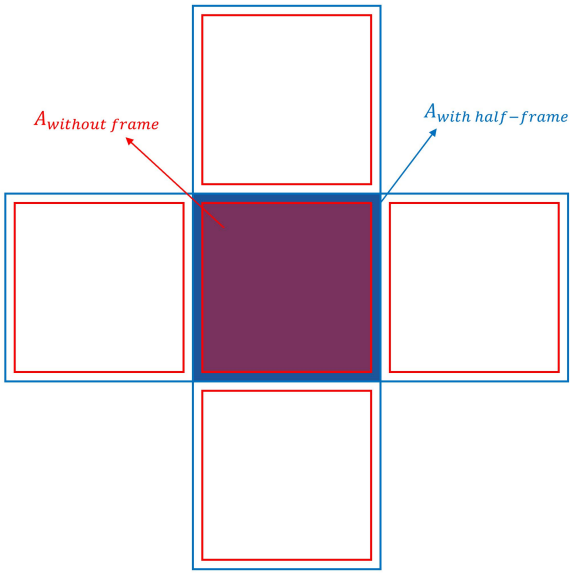

Figure 8.13: Schematic overview $A_{geometry\ without\ frame}$, and $A_{geometry\ with\ half-frame}$

Complex Patterns

So far, only patterns made up of a single regular polygon have been investigated, as they are usually the most widely used for motorsport applications, due to their high availability, hence lower purchase costs. It may happen that a more complex pattern composed of multiple polygons is desired, especially on street-legal cars, where styling also plays a role. To investigate such a case, a grille with a pattern made up of an octagon and a square sharing one side has been tested (Figure 8.4), utilizing the same model derived in subsection 8.2.2.

To achieve an accurate prediction, the static pressure drop was decomposed into two contributions: one from the octagonal section and one from the square section. These were then combined using weights consistent with the grille's geometric construction. Generalizing the approach for any geometrical pattern couple (where the two geometries are $geom\ 1$, and $geom\ 2$):

$$w_{geom\ 1} = \frac{n_{unit\ patterns} \cdot A_{geom\ 1\ with\ frame}}{A_{total}} \tag{8.20}$$

$$w_{geom\ 2} = \frac{n_{unit\ patterns} \cdot A_{geom\ 2\ with\ frame}}{A_{total}} \tag{8.21}$$

$$\Delta p_{geom\ 1+2} = \Delta p_{geom\ 1} \cdot w_{geom\ 1} + \Delta p_{geom\ 2} \cdot w_{geom\ 2} \tag{8.22}$$

Multiplying the area of the selected geometry by the number of times the unit pattern appears in the grille accounts for edge cuts, thereby improving the accuracy of the parameter.
The same approach, shown here for a pattern composed of two regular polygons, can be extended to a larger number of different geometries included in the pattern. The porosity ϵ required for estimating $\Delta p_{geom\ 1}$, and $\Delta p_{geom\ 2}$, can be obtained using Equation 8.19.

8.2.3. Richardson vs. Calmidi's Formulation

The formulation of Richardson et al. [34], presented in Table 3.2, showed a better RMSE than the formulation of Calmidi [4] when its extrapolation capability was tested.
Although the two formulations differ, the physical basis behind them is very similar. Both are based on the $(1-\epsilon)$ term, which goes to zero when the porosity is 1. The main difference between the two is that Calmidi also included the diameter of the wire as a variable; even though Richardson did not, its influence is still captured indirectly by the porosity ϵ.

The reason why Calmidi's formulation was still preferred over Richardson's is the poor performance the latter showed when used to predict the pressure drop curve of the grille comprising the octagon plus square pattern (Figure 8.4). This grille geometry serves as a critical extrapolation check. The shape factor is not derived from octagonal data, and the predicted pressure drop depends on the combined contributions of the octagon and square elements. If the prediction aligns with expectations, it strongly indicates robustness. However, the fact that it fails suggests the model is not reliable for predicting grilles that differ significantly from the fitted cases. In Table 8.9, an overview of the differences in accuracy in predicting the octagon+square grille in terms of RMSE is presented.

Octagon side length	RMSE Calmidi [4]	RMSE Richardson et al. [34]
1.7 mm	2.346 Pa	11.295 Pa
2.3 mm	1.321 Pa	2.844 Pa

Table 8.9: RMSE comparison between Calmidi and Richardson's formulations in predicting the octagon+square grille.

8.2.4. Robustness of the Model

One of the elements that was left out of the discussion is the reference geometry to use as a base for the modeling of the shape factor. In principle, there is no empirical or physical justification for favoring one geometry over another. Therefore, if the underlying model is formulated correctly, the predicted pressure drop should remain unaffected by the choice of geometry. To assess this aspect, pressure drops were computed for the hexagonal, the square, and the triangular grilles. As a reference, the pressure drop for each geometry, denoted as $\Delta P_{ref.\ geometry}$, corresponds to the CFD prediction for a grille with the same hydraulic diameter of 4.2mm. The perimeter of the reference geometry $P_{ref.\ geometry}$ was also adapted in the perimeter factor (Equation 8.12). Depending on the geometry, the perimeter is calculated from the hydraulic diameter D_h as:

$$P_{ref.\ geometry} = 4 \cdot D_h \quad : \quad \text{for the square}$$

$$P_{ref.\ geometry} = 2\sqrt{3} \cdot D_h \quad : \quad \text{for the hexagon}$$

$$P_{ref.\ geometry} = 3\sqrt{3} \cdot D_h \quad : \quad \text{for the triangle}$$

In Table 8.10, the RMSE obtained by predicting the same pressure drop with different reference geometries is shown. Since all the values are in line with each other, the initial hypothesis of independence of the results on the reference geometry used to model the shape factor is validated.

Reference geometry	**RMSE square grille prediction [Pa]**	**RMSE hexagonal grille prediction [Pa]**	**RMSE triangular grille prediction [Pa]**	**RMSE octagon+square grille prediction [Pa]**
Square	2.1193	1.1997	2.9731	1.8428
Hexagon	2.1880	1.3071	3.0288	1.9863
Triangle	2.1119	1.1879	2.9679	1.8314

Table 8.10: RMSE of the prediction of the static pressure drop of square, triangular, hexagonal, and octagon+square meshed grilles with the same hydraulic diameter (4.2mm), with different reference geometries.

Since the empirical coefficients of the shape factor formulation were calibrated by fitting the pressure drop curves of the triangle, hexagon, and square geometries, all sharing the same hydraulic diameter of 4.2mm, the RMSE values reported in Table 8.10 may reflect an intrinsic bias. Although the shape factor was recomputed using different base geometries, the coefficients were always obtained through a least-squares fit of the same underlying dataset. Consequently, the resulting prediction errors appear largely independent of the chosen base geometry, yet a residual bias is likely present due to the repeated use of identical calibration data.
To avoid it, the same model was used to check the independence of the model from the reference geometry used, when the longest diagonal of 6mm is fixed. Once again, the RMSE obtained (Table 8.11) is in line, proving the model is robust.

Reference geometry	**RMSE square grille prediction [Pa]**	**RMSE hexagonal grille prediction [Pa]**	**RMSE triangular grille prediction [Pa]**	**RMSE octagon+square grille prediction [Pa]**
Square	2.1993	1.0941	3.3410	1.1994
Hexagon	2.1880	1.1658	3.3964	1.3082
Triangle	2.1119	1.0920	3.3411	1.1867

Table 8.11: RMSE of the prediction of the static pressure drop of square, triangular, hexagonal, and octagon+square meshed grilles with the same longest diagonal (6mm), with different reference geometries.

Figure 8.14, 8.15, 8.16, and 8.17 show the absolute error in Pa between the results obtained from CFD and the ones predicted with the derived model. The error is defined as:

$$E = \Delta P_{model} - \Delta P_{actual} \tag{8.23}$$

Whenever the error is positive, it means the model is over-predicting the pressure drop; when it is negative, it is under-predicting it.

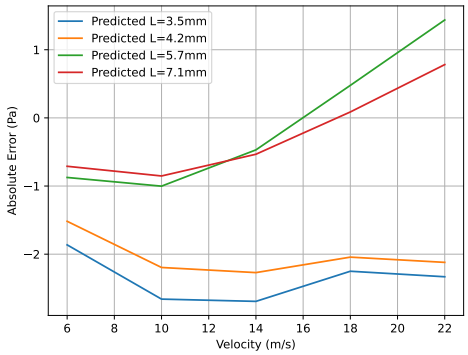

Figure 8.14: Absolute error of the derived model in predicting the pressure drop obtained from CFD at varying the side length L of a square grille with wire diameter 0.6mm.

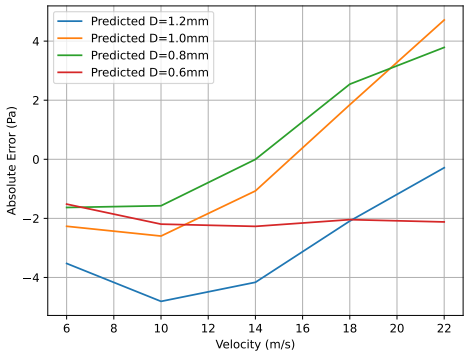

Figure 8.15: Absolute error of the derived model in predicting the pressure drop obtained from CFD at varying the wire diameter D of a square grille with side length 4.2mm.

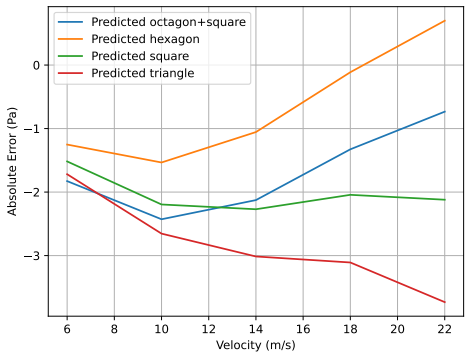

Figure 8.16: Absolute error of the derived model in predicting the pressure drop obtained from CFD with different pattern shapes with the same hydraulic diameter of 4.2mm, and wire diameter of 0.6mm.

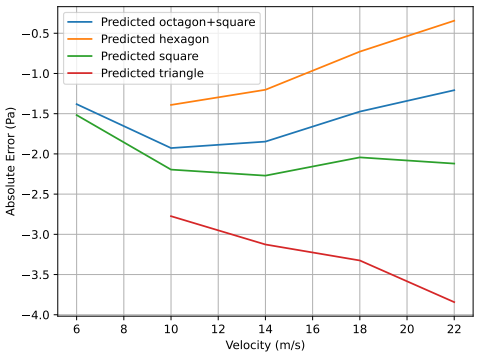

Figure 8.17: Absolute error of the derived model in predicting the pressure drop obtained from CFD with different pattern shapes with the same longest diagonal of 6.0mm, and wire diameter of 0.6mm.

III

Results

9

Correlation Between Numerical and Experimental Results

To assess the validity of the numerical model tested in CFD, and to quantify the differences due to the simplifications made to the simulated geometries, a correlation study between the results obtained experimentally and the numerical ones must be performed. In section 9.1 the setup used in the tests is outlined, and how the experimental results were properly compared to the CFD ones. In section 9.2, and 9.3, the usability of the results for the study is tested by shedding light on the robustness of the experimental results.

9.1. Correlation Study Setup

Two types of grille were used for the tests, since they were already available in the warehouse at Dallara. Both grilles were adopted in motorsport applications: ”Grille 224”, with a square pattern (side of 5.8 mm) and circular strut cross section (diameter of 0.6 mm), and ”grille custom”, also with a square pattern (side of 10.0 mm) and circular strut cross section (diameter of 1.0 mm), shown in Figure 9.1 and Figure 9.2 respectively.

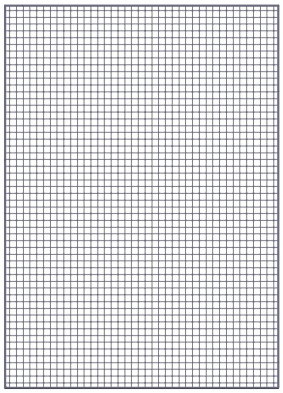

Figure 9.1: ”Net 224”, with a square pattern (side of 5.8 mm) and circular strut cross section (diameter of 0.6 mm)

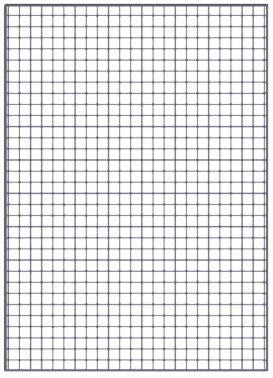

Figure 9.2: ”Net custom”, with a square pattern (side of 10.0 mm) and circular strut cross section (diameter of 1.0 mm)

All CFD results presented for comparison with the experimental data were evaluated by measuring the static pressure at the same locations where the probes were positioned during the tests. To verify the influence of alignment between individual points and the grille struts, multiple points spaced a few millimeters apart were sampled around each static pressure probe hole. The average of these points was then calculated and used for plotting. Since the pressure values at these points consistently differed by less than 2 Pa, the averaged value was considered representative. The pressure differences measured are always plotted at the average speed of the flow across the entire test section instead of the local velocity at the points. This approach ensures greater consistency with the experimental results. In the tests, the difference between probe locations is known, but the local velocity is not directly measured; instead, it is reported as an average across the test section.

For the radiator tests, a slightly thicker radiator was used compared to the one originally simulated in CFD. The initial radiator was unavailable at the time of testing, so an oil radiator was used instead. The plan was to rerun the relevant CFD setups using the porosity curve obtained from the experimental tests and then compare the results to establish the correlation.

9.2. Robustness of the Readings in the Original Test Bench Setup

As anticipated in chapter 7, tiny gaps are present between the parts used during the experimental setup. Even though they were at all times sealed by metallic tape, the surface was never as smooth as the one tested in CFD. For each setup tested, there were non-negligible losses in the system when neither a grille nor a radiator was placed in the test section. As a result, to get results comparable to CFD, these losses had to be measured and subtracted from the tests with the grille and/or the radiator (referenced as porous medium (PM) in the formula below):

$$\Delta P = \Delta P_{with\ PM} - \Delta P_{without\ PM} \tag{9.1}$$

As described in chapter 4, a preliminary test was done before the start of the project, testing whether the static pressure probes were able to measure a difference in static pressure between upstream and downstream of the grille. However, because this was the first time the test bench was used to measure the pressure drop across a grille, no reference values were available to assess the accuracy of the measurement.

9.2.1. Grille only Tests

To test it, the experiments were performed using two sets of pressure probes: the first set composed of existing probes, denoted as ”old”, and the second set composed of pressure probes specifically produced for these tests, denoted as ”new”.

For all the tests shown in this subsection the pairs of probes that measure the pressure differential have been assigned the following names as illustrated in Figure 9.3: ”Air 1” for the top left probes, ”Air 2” for the top right, ”Air 3” the bottom left, and ”Air 4” the bottom right.

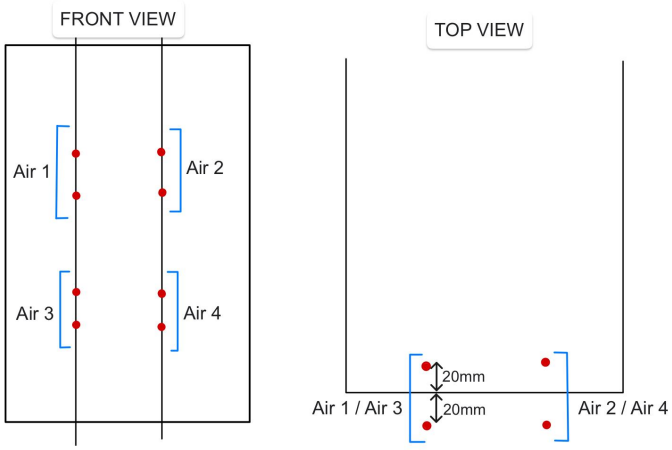

Figure 9.3: Vertical static pressure probes setup.

In Figure 9.4 and 9.5, the results obtained in the four static pressure differentials (”Air 1”, ”Air 2”, ”Air 3”, and ”Air 4”) are shown. The convention used is the one shown in Figure 9.3. These tests were performed using the original test bench setup (Figure 6.1).
In the case of the old pressure probes, only the right side is coherent (air 2 and air 4), while for the new probes, only air 2 and air 3 show coherence. From the CFD results, as shown in Figure 6.4, there is little to no difference between the left and right sides of the test section, so it is unlikely the asymmetry is due to the presence of the converging duct.
A first consideration that can be made is that the system losses are rather high compared to the expected pressure drop to be measured across the grille. This is an anticipatory sign of the reliability of the results, since it increases the amount of uncertainty in the results.

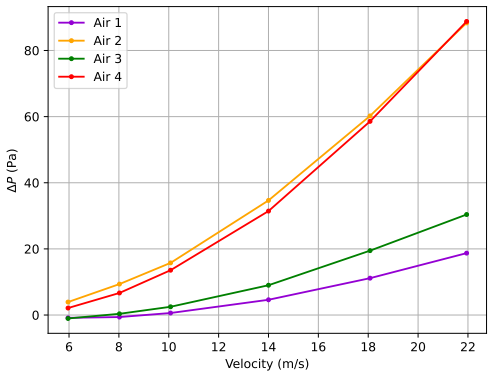

Figure 9.4: Experimental tests with no net, old static pressure probes.

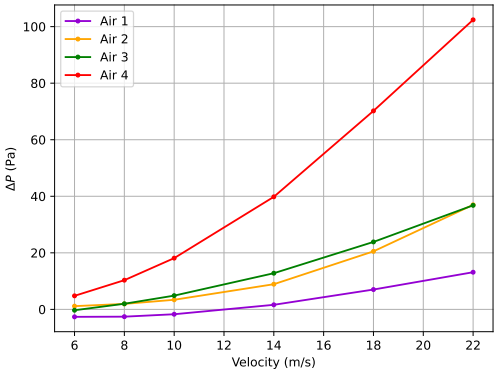

Figure 9.5: Experimental tests with no net, new static pressure probes.

The static pressure drops across ”net 224” with the old and new probes are presented in Figure 9.6 and 9.7 respectively. Even though when the old probes were used, all four pressure differentials were in line with each other and with the CFD results, when the test was repeated with the newly produced probes, the left and right sides of the test section were not coherent anymore.

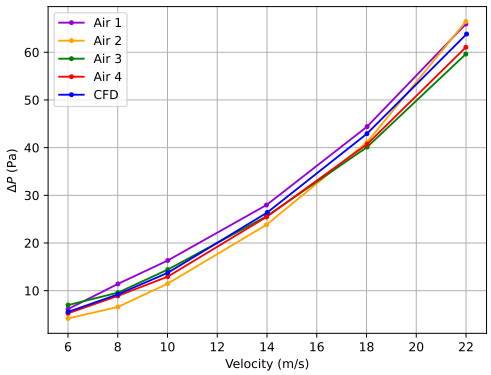

Figure 9.6: Experimental tests with ”net 224”, old static pressure probes.

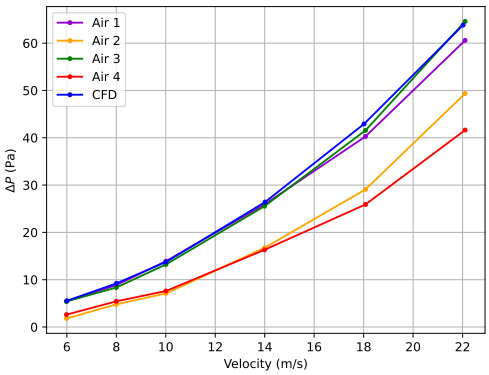

Figure 9.7: Experimental tests with ”net 224”, new static pressure probes.

In a similar fashion, Figure 9.8 and 9.9 represent the pressure drop across the ”custom grille” with the old and new probes, respectively.
The old probes this time showed coherence on the left side and on the right side, but not between the two sides. Interestingly, the CFD results appeared to be right in the middle between the two sides. The new probes agreed with the CFD results on the left side (air 1 and air 3), while the probes on the right side were not coherent.

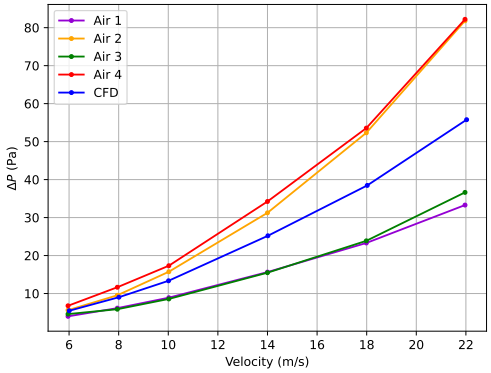

Figure 9.8: Experimental tests with ”net custom”, old static pressure probes.

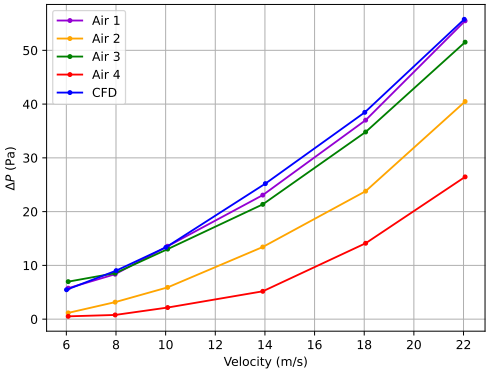

Figure 9.9: Experimental tests with ”net custom”, new static pressure probes.

To confidently use the results to perform a correlation study, the results collected should not vary significantly when varying the instruments, if the setup remains the same. The static pressure probes are positioned 20 mm from the grille, both upstream and downstream. Any local wake effects induced by the grille at this location should not be influential on the results. ”Grille custom” has the thickest wire of the two grilles tested, with a diameter of 1.0 mm; the pressure probe is positioned at 20 times the characteristic length of the grille, making it unlikely that any local wake effects are affecting the coherence of the results.

9.2.2. Probes Misalignment

To rule out the possible wake disturbance of the static pressure upstream on the downstream one, the downstream probes were moved inwards by 30 mm, as depicted in Figure 9.10. Comparing the results obtained with this pressure probe setup with the original setup also allows to have an insight into the velocity profile of the flow at

the test section, which from the CFD simulations appeared to be slower at its core than at its sides (Figure 6.8).

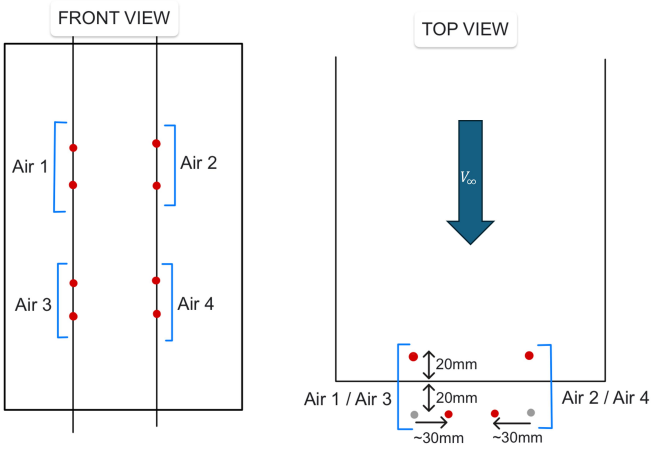

Figure 9.10: Misalignment of the downstream static pressure probes.

The CFD results exhibit the expected trend in the static pressure drop curve. When the core flow is slower, the static pressure measured by the downstream probe increases slightly as the probe is moved inward. If the upstream probe position remains unchanged, this results in a smaller pressure difference between the two probes. This behavior is clearly illustrated in Figure 9.11. Between the two configurations, at $V_\infty = 22\ \mathrm{m\,s^{-1}}$ the static pressure drop difference is 4.6 Pa.

The opposite trend occurred in the experimental results. The trend is consistent among all four static pressure differentials, which measure a higher drop in pressure with the pressure probes misaligned. This might suggest that in the experimental tests, unlike what seen in the numerical simulations, the velocity of the stream is higher in the core, as it would be in a fully developed velocity profile. However, such a large discrepancy between numerical and experimental results is unlikely. Considering the limited reproducibility of the experimental setup, potential sources of error, such as improperly connected probes or air leaks, cannot be ruled out. These factors could have contributed to the observed differences.

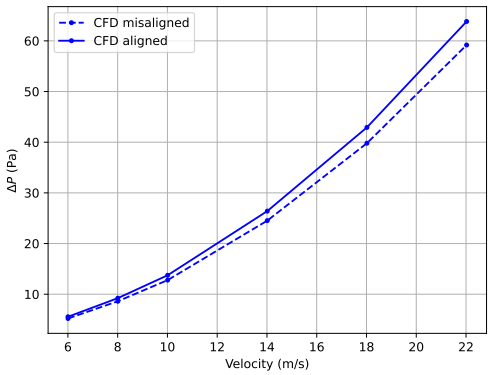

Figure 9.11: CFD results with ”net 224”, comparison between aligned and misaligned pressure probes.

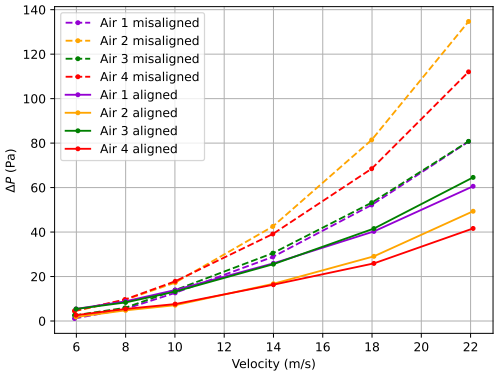

Figure 9.12: Experimental tests with ”net 224”, comparison between aligned and misaligned pressure probes.

9.2.3. Test with Radiator

Before evaluating the radiator in series with the grille, it was first tested on its own to assess its baseline performance in the original test bench setup, with the converging duct placed immediately upstream of it.

For the tests, the static pressure probes were rotated 90° horizontally. The position of the four static pressure differentials was not varied to maintain the same logic, as shown in Figure 9.13.

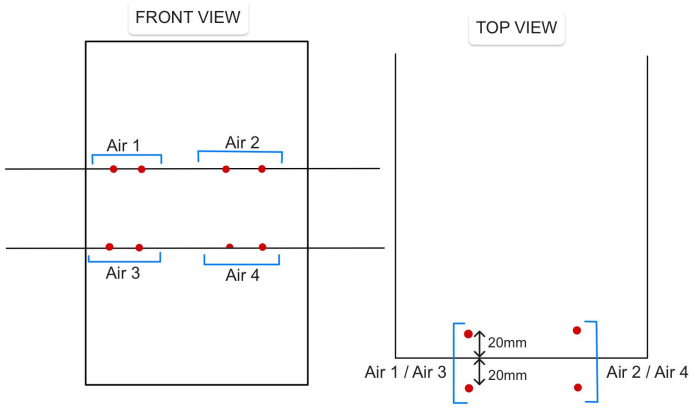

Figure 9.13: Horizontal static pressure probes setup.

The results presented in Figure 9.14 include the losses of the test system. The flow velocity during the experiments reached approximately 16.5 $\mathrm{m\,s^{-1}}$, which corresponds to the maximum airflow the test bench fan was able to deliver under the flow restriction imposed by the radiator.

All differential pressure probes exhibited consistent behavior. However, when examining the zoomed static pressure trend at approximately 16.5$\mathrm{m\,s^{-1}}$ (Figure 9.15), discrepancies of roughly 100–120 Pa emerged among the four measurement locations. Although these variations appeared significant in absolute terms, they represented only about 2.5% of the total pressure level being measured, which is one order of magnitude higher.

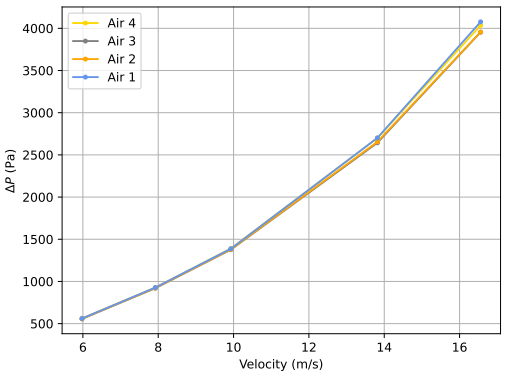

Figure 9.14: Pressure drop across the radiator, including the losses of the system.

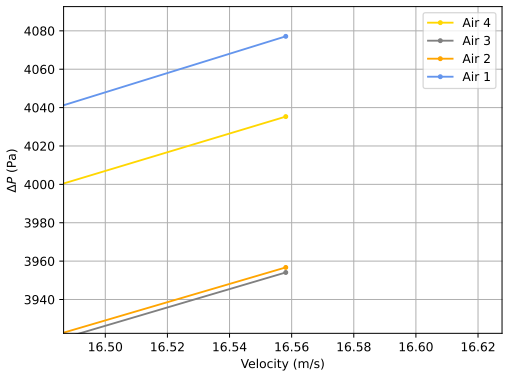

Figure 9.15: Pressure drop across the radiator, zoom-in.

This observation nonetheless provides an important indication regarding the sensitivity and suitability of the instrumentation: the probes were calibrated for radiator testing, where pressure drops are substantially larger. In contrast, the pressure differences across the grille alone are of the same order of magnitude as the resolution

limit of the static pressure probes. As a result, the system lacks the sensitivity required to accurately quantify the grille's standalone performance.

9.2.4. Test with Grille and Radiator in Series

The same setup presented in Figure 9.13 was also used for testing the radiator mounted in series to the "net 224". This grille was the one with the lowest porosity among the available ones. This choice ensures that if the grille contributes a significant pressure drop, its effect is more pronounced, especially considering that the radiator already imposes a substantial flow restriction.
The grille was inserted 5 mm upstream of the radiator, and the static pressure probes were kept mounted 20 mm upstream and downstream of the tested block.

The results reported in Table 11.4 include the losses of the empty test bench. Consistent with the behavior observed in subsection 9.2.3, the four differential pressure measurements showed good coherence (Figure 9.16), with discrepancies between the probes reaching up to approximately 100 Pa. In this configuration, the measurements also revealed a noticeable asymmetry: the right-hand side of the duct (air 2 and air 4) consistently exhibited lower pressure drops compared to the left-hand side (air 1 and air 3).

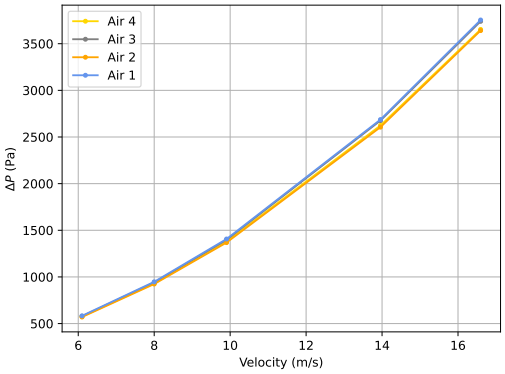

Figure 9.16: Pressure drop across the grille and radiator, including the losses of the system.

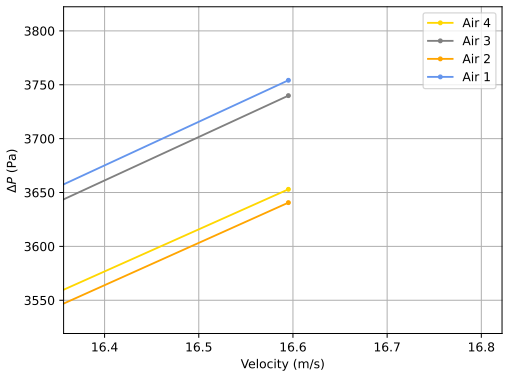

Figure 9.17: Pressure drop across the grille and radiator, zoom-in.

After the initial tests performed on the grille, the intention was to estimate the performance of the grille by taking the difference between the measurements obtained in the configuration with both grille and radiator and those obtained in the configuration with the radiator alone. To avoid aerodynamic interaction between the two components, the grille and the radiator would have been placed at a sufficient distance from each other. This distance would have been determined using numerical simulations together with a suitable safety factor.
During the experiments, it became evident that the differential pressure probes did not provide enough sensitivity to resolve the very small pressure drops generated by the grille on its own. Because the magnitude of the signal was comparable to the measurement noise, it was concluded that continuing with this testing strategy would have not produced reliable results. For this reason the procedure was not carried forward.

9.3. Robustness of the Readings in the New Test Bench Setup

To eliminate any doubt on the flow velocity profile at the test section raised by the CFD simulations (Figure 6.8), "net 224" was also tested inside the elongated 900 mm duct shown in subsection 7.1.2.

Likewise, the previous simulations performed on the grille alone with the original test bench setup, there is limited coherence between the four pressure differentials (Figure 9.18). Between the value read by ”Air 1” and ”Air 4” at 22 $\mathrm{m\,s^{-1}}$, there is a 40 Pa of difference; considering the overall pressure drop measured from CFD at this speed is roughly 60 Pa, the difference is more than half of the total amount read.

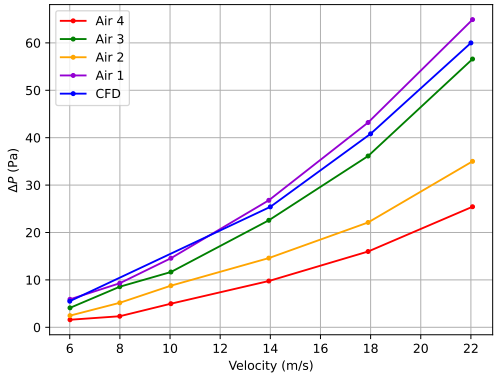

Figure 9.18: Experimental results for ”net 224” using the new setup.

10

Pressure Drop Analysis: Grille Parameters and Coupled Effects

This chapter investigates all the parameters involved in the grille design process, highlighting the relative impact they have on the pressure drop across both the grille itself and the radiator positioned downstream of it. All the parameters involving the grille alone are discussed in section 10.1, while the coupling effect between the radiator and the grille is discussed in section 10.2. Since the results could not be properly correlated, as discussed in chapter 9, all the results shown are obtained from CFD simulations, utilizing the new test bench setup (Figure 7.4).

10.1. Grille Pressure Drop Drivers

Before diving into the empirical prediction of the pressure losses across a grille, it is necessary to fully understand which geometrical parameters influence the losses, and to which extent. In this section all the parameters investigated are thoroughly analyzed, including a comprehensive explanation of their relative impact in the generation of aerodynamic losses. The rpesssure drop drivers have been ordered per their relative impact on the static pressure drop.

10.1.1. Effect of Boundary Layer

The first aspect investigated is the effect that the walls of the duct around the grille have on the static pressure drop. This has been the first parameter investigated, since it allows to know how the shape of the duct around the grille influences the results.

Within the boundary layer, the fluid velocity decreases smoothly from the free stream value to zero at the wall. When the measurement region includes this near wall zone, the plane averaged velocity becomes lower because the slow flow in the boundary layer reduces the overall mean value compared to the core flow. Since pressure losses vary with the square of the velocity, even a moderate reduction in the averaged velocity produces a noticeable effect on the inferred pressure drop. This behavior is shown in Figure 10.1. The figure presents the pressure drop curves for several mesh geometries, specifically triangular, hexagonal, square, and octagonal with an inner square, each with a longest diagonal of 6 mm. For each geometry, the pressure drop is evaluated on two measurement planes. The first one extends across the entire width of the duct and is referred to as the ”100% plane”. The

second one covers 60% of the duct width, thereby excluding most of the boundary layer region. The difference between these two evaluations clearly demonstrates the influence of the boundary layer on the resulting pressure drop estimation. For every tested grille configuration, the curves from the small and large measurement planes overlap. Therefore, it can be concluded that the only effect of including the boundary layer is a reduction in the plane-averaged velocity, shown by the leftward and downward shift of the pressure points obtained with the larger plane.

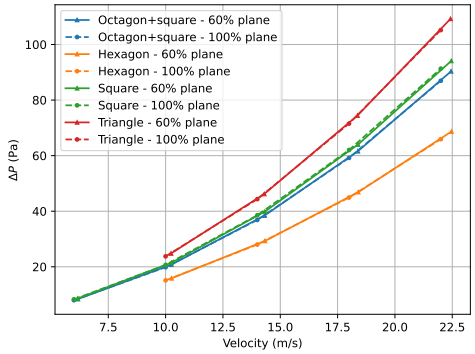

Figure 10.1: Boundary layer effect on static pressure drop

The main takeaway is that the grille's aerodynamic efficiency is independent of the portion of cross-section considered. The inclusion of the near-wall boundary layer region only affects the average speed over its cross-section, impacting the absolute average static pressure drop registered across the grille.
For all the subsequent investigations, the pressure drop presented will be taken across the largest plane, including the effect of the boundary layer, as this is the case closest to reality.

10.1.2. Effect of Wire Cross Section

The cross-section of the wire is the geometrical characteristic investigated with the biggest impact on the static pressure drop across the grille. As mentioned in Hoerner [13], a square cross section increases the amount of surface area where the flow stagnates, leading to significantly higher static pressure losses (a nearly 90% increase, as reported in Table 10.1) compared to the same square grille, with a circular wire of 0.6 mm in diameter and side length of 4.2 mm (Figure 10.2). This effect is considered the most impactful on the aerodynamic losses of the grille, as choosing the circular one allows to have a reduction in static pressure loss, without losing structural integrity, nor changing any other geometrical parameter (wire thickness, opening size, geometrical shape, ...).

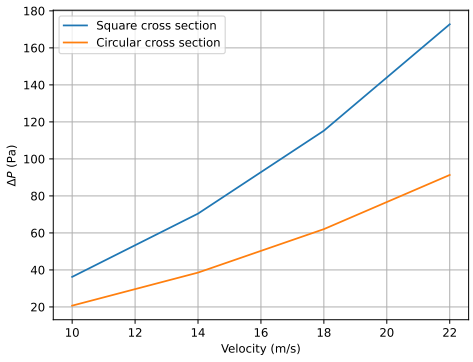

Figure 10.2: Effect of wire cross section on static pressure drop.

Cross Section Type	ΔP from circular cross section [%]
Square	+89.2
Circular	-

Table 10.1: Static pressure drop difference of each grille form the most porous one at V_∞=22$\mathrm{m\,s^{-1}}$.

In Figure 10.3 and 10.4, a visual overview of the difference in stagnation pressure build-up in front of the grille's struts is shown. In the case of the square cross-section, the stagnation region is much larger, leading to the significantly higher static pressure loss compared to the circular case.

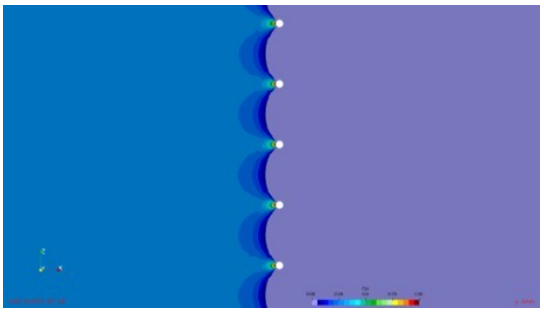

Figure 10.3: Pressure coefficient distribution for a wire with circular cross section.

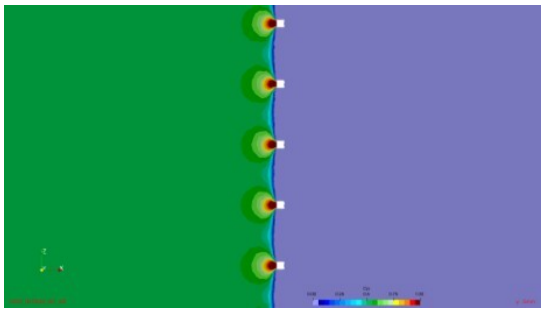

Figure 10.4: Pressure coefficient distribution for a wire with square cross section.

When the wire has a square cross-section, the vortex shedding becomes much stronger because the sharp edges force the flow to separate immediately at the trailing corners. The different formation of trailing edge vortices between the round and square wire is shown in Figure 10.5 and 10.6, respectively.

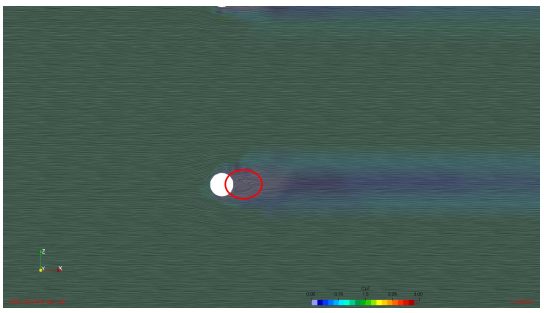

Figure 10.5: Streamlines around a wire with circular cross section.

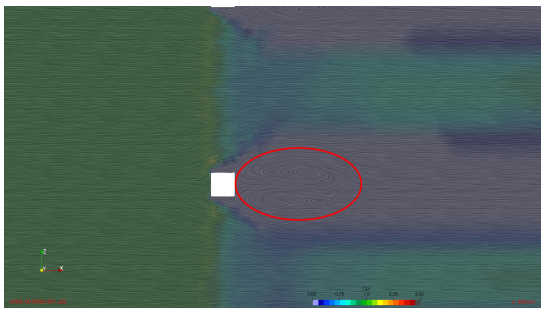

Figure 10.6: Streamlines around a wire with square cross section.

10.1.3. Effect of Geometrical Mesh Shape

Another key parameter is the geometrical shape of the pattern used. In order to properly compare the different shapes, they must be considered based on the protection they provide against all debris bigger than a certain chosen size.

Given a debris of size x, two paths have been explored to provide sufficient protection, as visually shown in Figure 10.7:

1. Fixing the longest diagonal $d = x$: this approach consists of fixing the longest diagonal of the shapes considered, where the diagonal is as long as the largest debris dimension. This approach is very conservative, as it ensures that the required protection is met, regardless of the shape of the debris. Shapes with fewer sides are disadvantaged under this approach, as they enclose less area for a given maximum diagonal. The circle represents the optimal case, maximizing enclosed area for a fixed span.

2. Fixing the diameter of the inscribed circumference $D = x$: this approach assumes the debris striking the grille is roughly spherical. By designing the opening so that the largest circle that can fit inside the chosen geometry is no bigger than the debris diameter, you get adequate protection. But because this relies on debris being mostly sphere-like, it doesn't guarantee full protection against irregular or elongated objects

that could still slip through. On the positive end, this approach re-evaluates shapes with fewer sides, like the triangle, which are otherwise more compromised by the first approach of fixing the longest diagonal. As represented in Figure 10.8, for the same inscribed circumference, the triangle comprises more free area (green one in the figure) than the square.

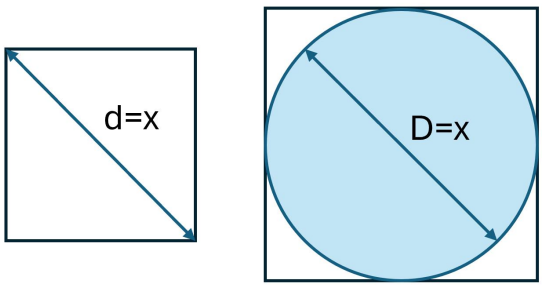

Figure 10.7: Visual comparison of the two protective paths explored.

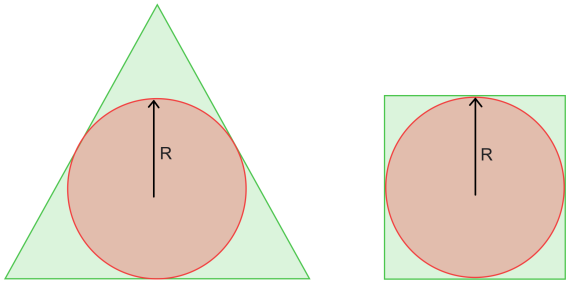

Figure 10.8: Comparison of available empty area per given inscribed circumference radius.

The choice of which approach to prefer depends on the type of debris present at the tracks where the races are programmed to take place. In the two subsections below, the results for both approaches will be presented to provide insights into the performance difference between the two approaches. In the case of the approach fixing the dimension of the inscribed circumference, a diameter of 4.2 mm was chosen; for the second approach, a diagonal of 6 mm was selected.

Same Inscribed Circumference D=4.2mm

As shown in Figure 10.9, the best performing shape when fixing the size of the inscribed circumference is the hexagonal one. However, as described above, the advantage of this shape is marginal over the square and triangle. For the pattern made out of an octagon and a square, the circumference considered is the one inscribed into the octagon, as it represents the widest opening. Although the octagon itself should lead to a higher overall porosity, the contribution of the square is significantly damaging to its aerodynamic performance. The octagon, given its small side length for a fixed inscribed circumference, results in the neighboring square having a very narrow opening, creating an overall significant resistance to the flow.

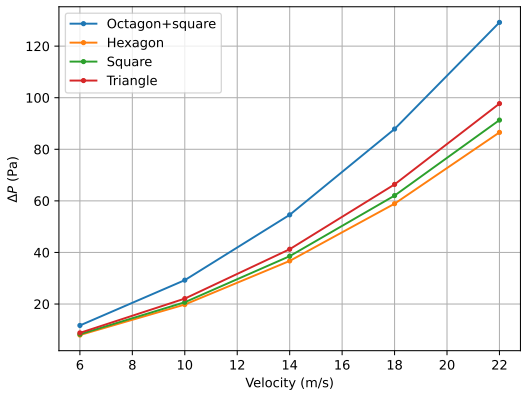

Figure 10.9: Geometrical change effect on static pressure drop at constant hydraulic diameter of 4.2 mm.

Geometrical Shape	ΔP **from hexagonal shape [%]**	ϵ [%]
Octagon+square	+49.2	71.1
Triangle	+12.9	76.0
Square	+5.0	76.1
Hexagon	-	76.3

Table 10.2: Static pressure drop difference of each grille from the most porous one at V_∞=22$\mathrm{m\,s^{-1}}$.

Overall, the hexagonal shape delivers the best performance. However, if manufacturing constraints or cost considerations prevent its use, substituting it with a grille featuring a square or triangular pattern results in only minor performance losses.

Same Longest Diagonal d=6 mm

As shown in Figure 10.10, when the longest diagonal is fixed, the best-performing geometrical shapes are the ones with the largest number of sides, since they are the ones with the largest amount of open area per perimeter.

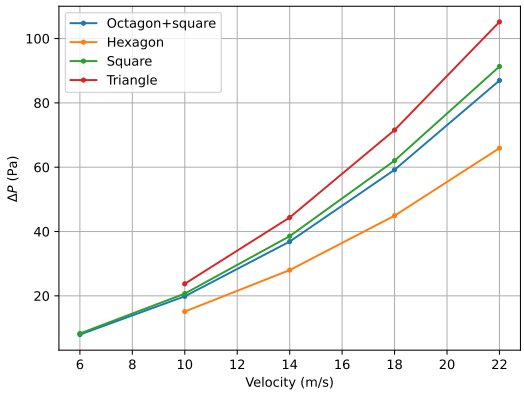

Figure 10.10: Geometrical change effect on static pressure drop at constant longest diagonal of 6 mm.

Geometrical Shape	ΔP from hexagonal shape [%]	ϵ [%]
Triangle	+59.5	74.9
Square	+38.5	76.1
Octagon+square	+31.9	77.3
Hexagon	-	80.3

Table 10.3: Static pressure drop difference of each grille from the most porous one at V_∞=22m s^{-1}.

Compared to the case discussed above, where the inscribed circumference was fixed, here the difference between the various shapes considered is more pronounced, placing the hexagonal grille far ahead of the square, triangle, and octagon plus square patterns. Similarly, the pattern composed of the octagon and the square is penalized by the presence of the tiny square sharing its side with the octagon; although in this case, the geometry still performs as second best.

45° Square Rotation

The last geometrical aspect considered was the impact of rotating 45° the square pattern, to investigate whether it would have an impact in terms of performance. This test was performed based on the observation that this specific orientation of the square was used in various automotive applications.

Since there is no physical reason to expect a difference in performance, the results shown in Figure 10.11 are unsurprising: the static pressure drop curve of the rotated square coincides with that of the non-rotated configuration.

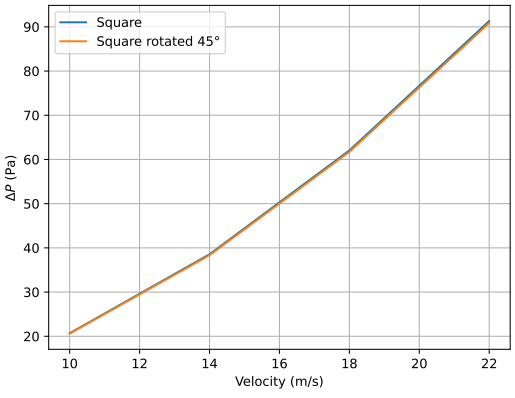

Figure 10.11: Square rotation effect on static pressure drop.

10.1.4. Effect of Wire Thickness

The increase in wire diameter changes the porosity of the grille, increasing the pressure drop. The four grilles compared share a square pattern with a side length of 4.2 mm. As reported in Table 10.4, a doubling of the diameter of the wire from 0.6 to 1.2 mm brings an increase of static pressure loss of roughly 150%. This is directly linked to the porosity of the grilles, which increase as the wire diameter decreases. If the porosity is higher, then the blockage effect on the flow and pressure losses introduced are lower (Figure 10.12).
The minimum size of the wire is, although limited by the structural integrity of the grille: thinner wires are more fragile, and the grille might break when hit with debris on the track.

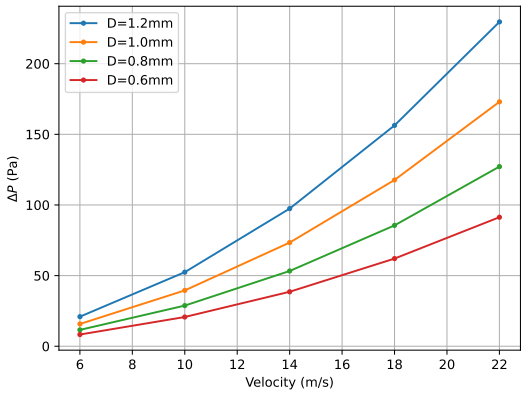

Figure 10.12: Wire thickness effect on static pressure drop.

d [mm]	ΔP **from d=0.6** mm **[%]**	ϵ [%]
1.2	+151.4	59.6
1.0	+89.5	64.6
0.8	+39.2	70.1
0.6	-	76.1

Table 10.4: Static pressure drop difference of each grille from the most porous one at V_∞=22m s^{-1}.

10.1.5. Effect of Opening Size

One other aspect directly influencing the amount of air let through the grille is the size of the openings. The investigation has been made considering square grilles, having a circular wire diameter of 0.6 mm, where the only variable parameter is the side length of the square, ranging from 3.5 to 7.1 mm.
As expected, as the opening area increases, the porosity also increases (Table 10.5), leading to a reduction in static pressure losses. When the size of the square is doubled (going from 3.5 to 7.1 mm), the pressure drop at 22 m s^{-1} increases by 147%, making this parameter very sensitive to the static pressure losses registered.

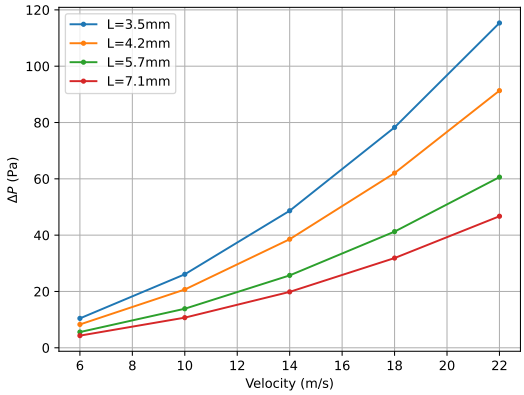

Figure 10.13: Opening size (L) effect on static pressure drop.

L [mm]	ΔP **from L=7.1** mm **[%]**	ϵ [%]
3.5	+147.0	72.3
4.2	+95.5	76.1
5.7	+29.8	81.9
7.1	-	85.1

Table 10.5: Static pressure drop difference of each grille form the most porous one at V_∞=22m s^{-1}.

From this analysis, a wider side length is generally advantageous, as it increases the available open area for the air to pass through. However, the maximum allowable length is constrained by the level of protection required for the specific application. The design must therefore balance openness with the necessary protective performance.

10.1.6. Effect of Passage Length

The passage length l in Table 10.6 denotes the grille's depth. Its influence was assessed by comparing the square grille, built from a 0.6 mm wire with a 4.2 mm side length, to versions of the same grille extended by 5 mm and 10 mm in depth. Because this extension is aligned with the direction normal to the grille's main plane, none of the grille variants introduces any flow deflection.

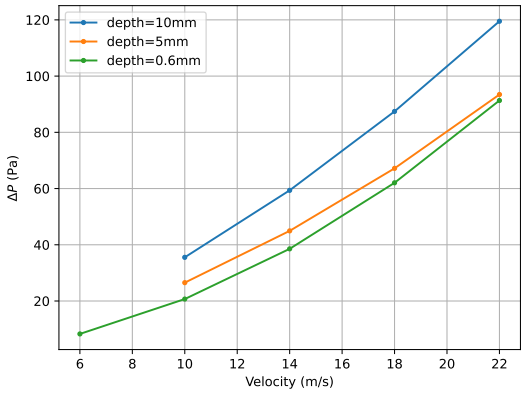

Figure 10.14: Passage length effect on static pressure drop.

l [mm]	ΔP **from** l**=0.6** mm **[%]**	ϵ [%]
10	+30.8	76.1
5	+2.3	76.1
0.6	-	76.1

Table 10.6: Static pressure drop difference of each grille from the most porous one at V_∞=22m s^{-1}.

As the passage length increases, the flow has time to develop a thicker boundary layer on the walls of the grille. The boundary layer creates a blockage in the proximity of the wall, shrinking the effective flow area and reducing the effective porosity of the grille. This effect is particularly visible in the grille with a 10 mm passage length, while in the 5 mm it is mostly visible at the lower speeds. As the velocity increases (hence the Reynolds number), the inertial effects in the flow become mush stronger than the viscous ones, and the boundary layers tend to be relatively thin (Leishman [22]). This reduces its blockage effect, leading to lower losses.

A visual overview of the boundary layer build up as the passage length increases from the thin grille to the 10 mm grille is shown in Figure 10.15, 10.16, and 10.17. The increase in velocity magnitude in the 10 mm deep grille (darker red color) indicates the area of passage is decreasing due to the boundary layer growing in between the grille's walls.

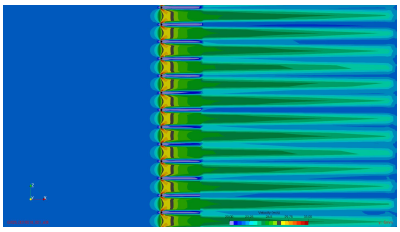

Figure 10.15: Velocity magnitude distribution in the thin grille.

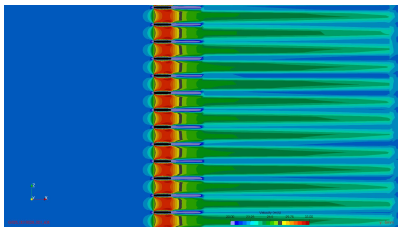

Figure 10.16: Velocity magnitude distribution in the 5mm deep grille.

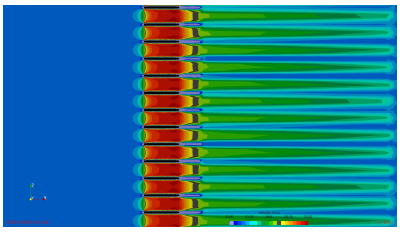

Figure 10.17: Velocity magnitude distribution in the 10mm deep grille.

Although the thinnest grille is the most efficient because it minimizes the boundary-layer blockage, it is still useful to study how passage length affects static pressure loss. Increasing the grille depth can be used to steer the flow so it aligns better with the radiator, potentially recovering some of the pressure losses incurred on the grille side at the radiator.

10.2. Grille–Radiator Coupling Effects

This section focuses on the impact the grille has on the radiator and vice versa. In particular, two main aspects will be investigated: the effect of the distance between grille and radiator, and the potential usage of the grille to direct the flow towards the radiator when it is inclined with respect to the incoming freestream flow.

The overall pressure drop across the block composed of the grille and radiator is given by the following contributions:

$$\Delta P = \Delta P_{grille} + \Delta P_{radiator} + \Delta P_{recovery} \tag{10.1}$$

where $\Delta P_{recovery}$ is negative, and represents the pressure delta occurring in the region between the two porous media. Each of these contributions will be thoroughly discussed in this section.

10.2.1. Effect of Distance Grille-Radiator

In order to thoroughly investigate the impact of the distance between the grille and the radiator, the pressure losses have been evaluated between various planes, located both upstream and downstream of the grille and the radiator. To ease the understanding of the results, the same color convention of the planes shown in Figure 10.18 has also been used in the graphs below. Throughout the entire study, the grille was always kept at the same location, and only the radiator was moved. Both of them were always oriented normally with respect to the incoming flow. The distances tested between grille and radiator were 2.5, 5, 10, 20, 50, 100, and 200 mm. For all the tests, the grille considered has a square pattern of side length 4.2 mm and circular wire of diameter 0.6 mm.

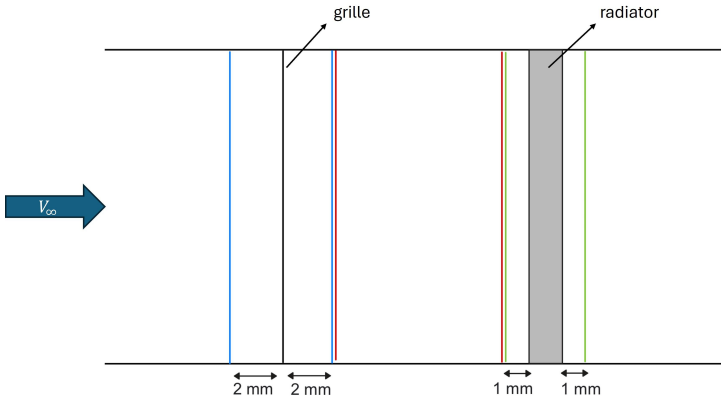

Figure 10.18: Static pressure measure planes color convention.

The results showing the effect the presence of the radiator has on the grille when placed at different distances apart are reported in Figure 10.19. Immediately upstream of the radiator, a stagnation pressure build-up occurs. Positioning the grille very close to the radiator places it within this high-pressure region, which significantly reduces the pressure drop effect that the grille would exhibit in free flow. As the distance increases, this effect vanishes, and the pressure drop across the grille reaches the free flow value (indicated by the dashed horizontal black line) asymptotically. From Figure 10.19, the grille seems to greatly benefit from the presence of the radiator only if positioned within millimeters of the inlet face of the radiator. However, local pressure variations immediately upstream and downstream of the radiator are not captured with full accuracy due to the fact it is modeled as a porous medium, which also affects the estimated magnitude of its influence on the grille.
A similar trend also occurs on the radiator level (Figure 10.21), with the pressure losses being minimal when

the grille is closest to the radiator. As the radiator is moved further downstream, its performance approaches the asymptotic losses it would have if the grille were not present. This effect can be attributed to the radiator being influenced by the grille's wake, which consists of regions of both high and very low velocity. Since the pressure drop across the radiator is quadratically proportional to the local inlet velocity in each surface mesh cell of its upstream face, the non-uniform velocity distribution caused by the grille results in a lower overall pressure loss across the radiator.

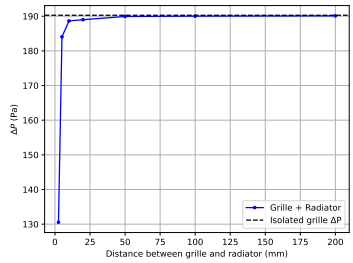

Figure 10.19: ΔP across the grille.

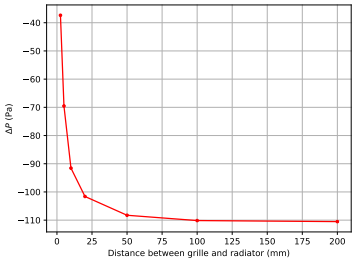

Figure 10.20: ΔP between grille and radiator.

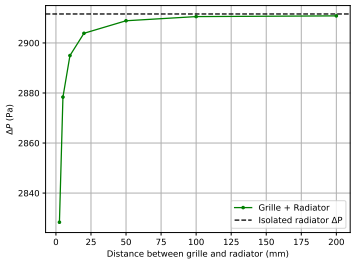

Figure 10.21: ΔP across the radiator.

In between the grille and the radiator, there is the so-called "pressure recovery" region (Malico et al. [26]). The static pressure adjusts downstream of the grille, slightly reducing the bulk pressure drop, which is measured from the inlet face of the porous medium to the outlet face:

$$p_{bulk} = p_{outlet} - p_{inlet} \tag{10.2}$$

Since the grille has a high porosity value, resulting in a rather low bulk pressure drop, the pressure recovery effect becomes significant. When the radiator is placed very close to the grille, there is not sufficient space for the pressure to fully recover, resulting in a lower static pressure gain. This effect is better highlighted when looking at the upper graph of Figure 10.22, where the pressure recovery for the different distances between grille and radiator is clearly shown. Because the spatial resolution of the graph decreases as the distance from the grille increases, the static pressure drop curves associated with the radiator are not perfectly parallel.

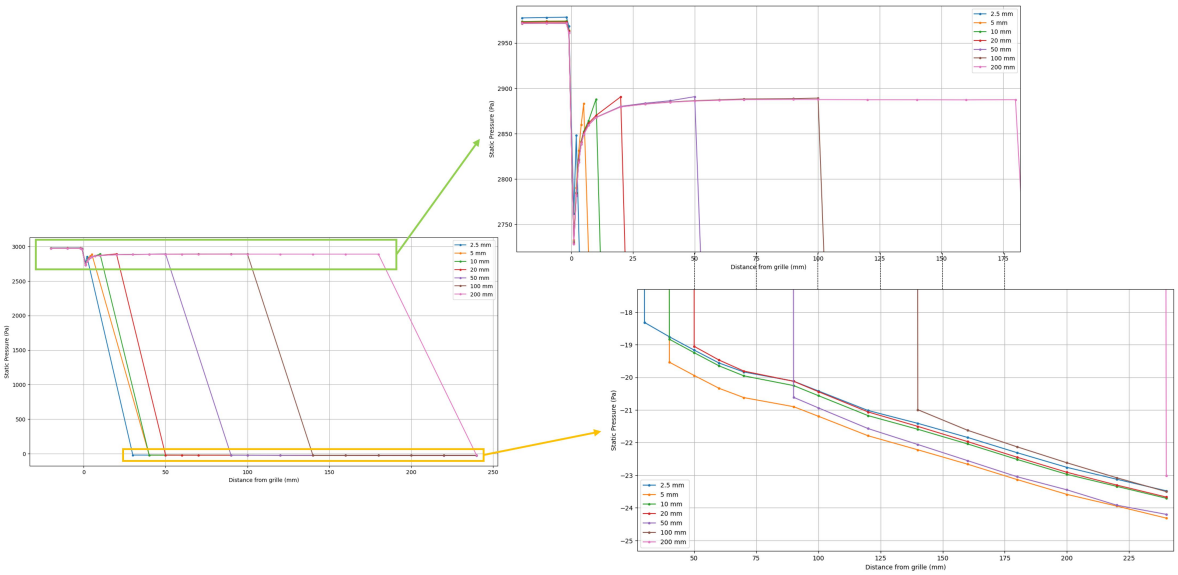

Figure 10.22: Static pressure distribution across the grille and radiator at variable distances between the two (*the pressure scale differs from the top right to the bottom left graph*).

It is also interesting to analyze the overall static pressure losses registered across the block comprising the grille and the radiator. The color convention of the planes used for this analysis is defined in Figure 10.23.

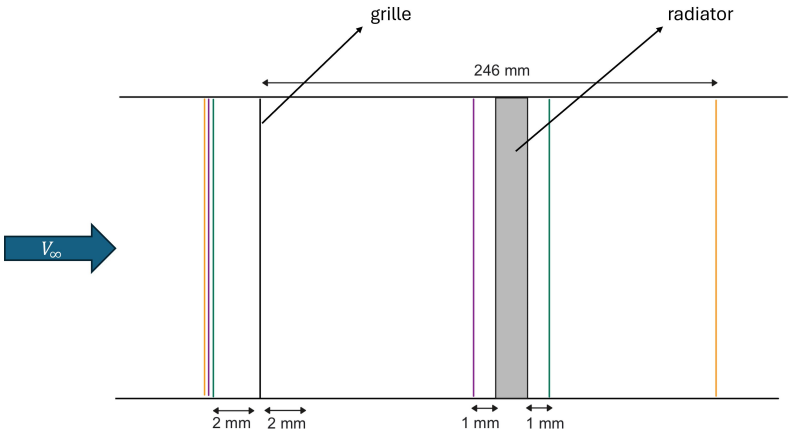

Figure 10.23: Static pressure measure planes color convention.

Figure 10.24 shows that up until the radiator, the sum of the pressure lost across the grille and of the pressure recovery effect is minimized when the radiator is located far downstream from the grille.
The pressure drop across the block composed of the grille and the radiator was measured in two ways:

- Firstly, by keeping both the plane upstream and downstream of the grille constant (Figure 10.25). In order to do so, the plane upstream of the grille was fixed 2 mm from the grille, and the one downstream 246 mm from the grille. At this location, the plane is always downstream of the radiator, even when the radiator is 200 mm from the grille.
- In motorsport applications, the duct is very often interrupted past the radiator, as there is no need to channel the air downstream of it. For this reason, a comparison of pressure drop from the same 2 mm plane upstream of the grille to one 1 mm downstream of the radiator was made (Figure 10.26).

For each result obtained, the pressure losses measured in the empty duct at the corresponding plane locations were subtracted.
In both configurations, the trend is the same: the overall static pressure loss is minimized when the radiator is as far as possible from the grille. However, the difference from the worst case (2.5 mm distance) to the best performing case (200 mm distance) is roughly 6 Pa, which is negligible.

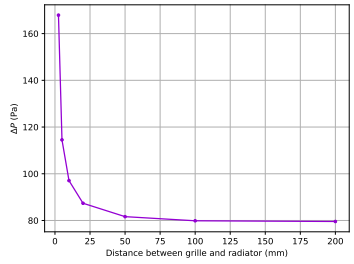

Figure 10.24: ΔP between 2 mm upstream of the grille and 1 mm upstream of the radiator.

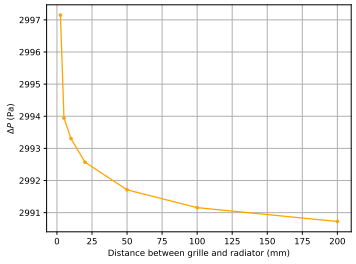

Figure 10.25: ΔP between 2 mm upstream of the grille and 246 mm downstream of the grille.

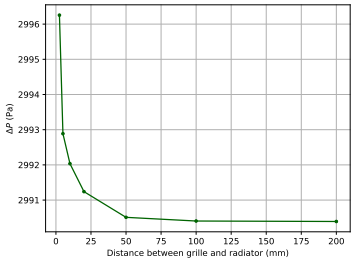

Figure 10.26: ΔP between 2 mm upstream of the grille and 1 mm downstream of the radiator.

Because of the way the simulations were set up, fixing the inlet velocity of the flux inside the duct, the amount of mass flow flowing through the radiator was the same in every configuration. As a result, the radiator always

had the same cooling capacity. The best performing radiator resulted hence being the one where the grille was located the closest to the radiator, having the lowest loss of pressure for the same amount of cooling performance. The combined effect of grille and radiator indicates an opposite optimum, with the radiator placed as far as possible from the radiator. The difference between the worst and best case, though, is almost negligible. Therefore, while the contribution of the grille and radiator to the pressure loss varies, the combined effect of the two is almost entirely independent of the distance between them.

The formulation derived for the static pressure drop across the grille is equal to the sum of ΔP_{grille} and $\Delta P_{recovery}$ (Equation 10.1). The losses estimated across the grille and radiator can then be represented by two porous media in series, with the pressure drop given by:

$$\Delta P = \Delta P_{grille\ modeled} + \Delta P_{radiator} \tag{10.3}$$

10.2.2. Effect of Flow Directionality

The last aspect investigated is the usage of the grille to direct the flow towards the inlet face of the radiator when this one is at an angle with respect to the horizontal. For the study, the radiator was inclined 30° with respect to the horizontal. The color convention of the static pressure measure planes used is shown in Figure 10.27.

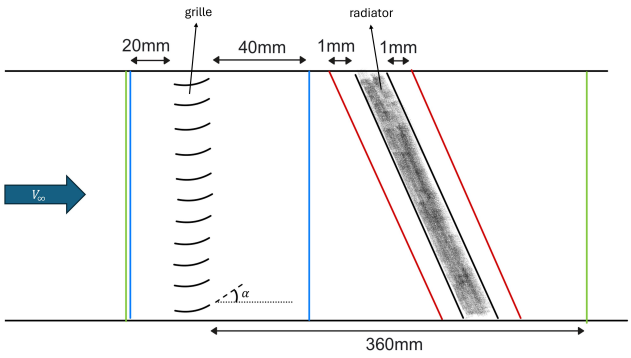

Figure 10.27: Static pressure measure planes color convention.

The center of the radiator, around which it was rotated, was positioned 200 mm from the grille (note that Figure 10.27 is not up to scale). It was chosen to use grilles with a passage length of 10 mm and to shape them like an airfoil, to bend the flow towards the radiator. The airfoil shapes were constructed with the grille's leading edge kept parallel to the horizontal plane. The bending angle (α) was defined as the angle formed by the line tangent to the trailing edge relative to the horizontal plane. Both 15° and 30° were tested and compared to the case of the thin grille, also located 200 mm from the inclined radiator. The entire study has been done at a freestream speed of 22 $\mathrm{m\,s^{-1}}$, as this speed is the highest of the range, and any aerodynamic effect induced by the different grille geometries is maximum.

The effect across the grille (Figure 10.30) is as expected: as the airfoil angle α increases, also the pressure drop across the grille increases. As shown in Figure 10.28 and 10.29, the airfoil shape creates a pressure field around it which bends the flow not only downstream of it, but also upstream, modifying the effective angle of attack. The effect is more pronounced in the 30° airfoil case, bringing a more aggressive curvature of the flow, but also higher losses to be attributed to the higher pressure drag being formed.

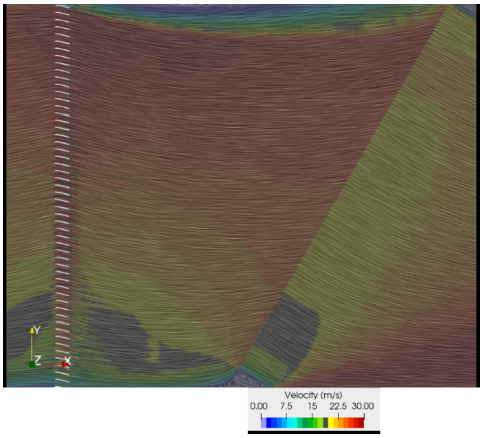

Figure 10.28: Streamlines 15° airfoil.

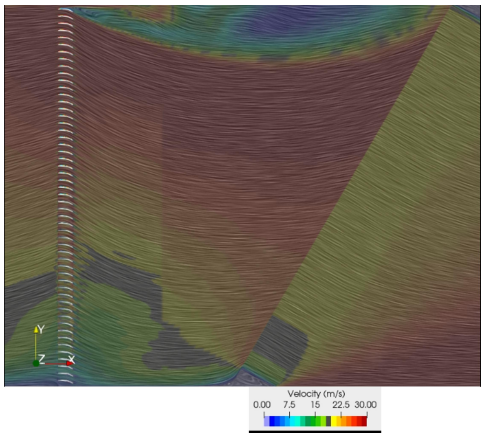

Figure 10.29: Streamlines 30° airfoil.

Given the large distance between the grille and the radiator, the flow has time to stretch out in between, partially losing the directionality given to it by the grille. For this reason, looking at Figure 10.31, there is a very little difference between the 15° to 30° case in terms of static pressure drop across the radiator. Instead, compared to the thin grille, the airfoil-shaped grilles bring roughly a 400Pa gain.

When summing the contributions from both the radiator and the grille, the overall static pressure difference between upstream of the grille and downstream of the radiator decreases significantly when airfoil-shaped grilles are used. This occurs because the performance loss at the grille level is relatively small compared to the gain achieved on the radiator side. The difference in total pressure loss between the 15° and 30° airfoil configurations is primarily due to the additional loss introduced at the grille level when the latter is employed.

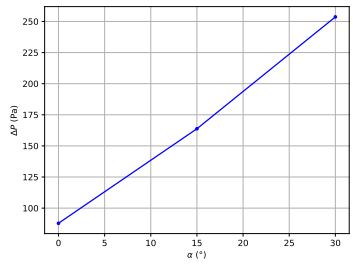

Figure 10.30: ΔP between 2 mm upstream of the grille and 1 mm upstream of the radiator.

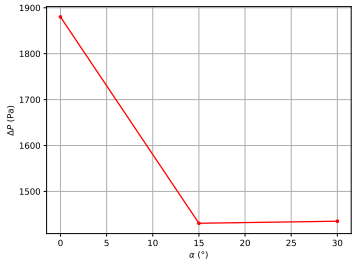

Figure 10.31: ΔP between 2 mm upstream of the grille and 246 mm downstream of the grille.

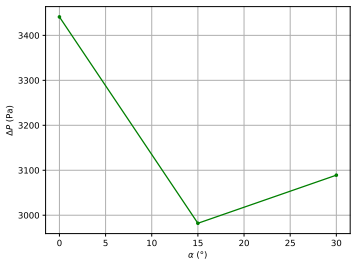

Figure 10.32: ΔP between 20 mm upstream of the grille and 360 mm downstream of the grille.

Producing these airfoil-shaped grilles is, in general, very expensive, as they cannot be bought off-the-shelf, and would require a specific ad-hoc production. Such grilles would also require a careful design, with multiple iterations to correctly shape the airfoil to maximize its performance, which once again increases the design costs. For these reasons, it was chosen not to further optimize the design of the shape of the airfoil.

The primary intent of this study was to assess the potential performance gain of this design idea. Better aligning the leading edge of the grille with the incoming flow would certainly help reduce the static pressure drop across the grille, while still obtaining the required flow deflection. Because the duct was kept the same, a large recirculation region was created in the top region, as can be seen in the more blue bubble in Figure 10.28 and 10.29. These would be easily avoided by shaping the duct in a way to follows the direction of the flow.

11

CFD Modeling of the Grille

To make the simulations computationally cheaper, the grille has to be modeled numerically in a simplified way. This chapter deals with the accuracy of the derived model for predicting the pressure drop of a given grille's geometry in section 11.1, the limitations of the porous medium modeling approach in section 11.2, and the actual gains in terms of computational time in section 11.3.

11.1. Modeled vs. CFD Results

This section presents a direct comparison of the static pressure curves predicted with the formula derived in section 8.2 and the actual data obtained from the CFD simulation, with the grille modeled geometrically.

In Figure 11.1 and 11.2, the predicted curves representing the loss of static pressure when increasing the opening size and the diameter of the wire of square grilles respectively, are plotted next to the same grille's geometries simulated numerically (dashed lines).

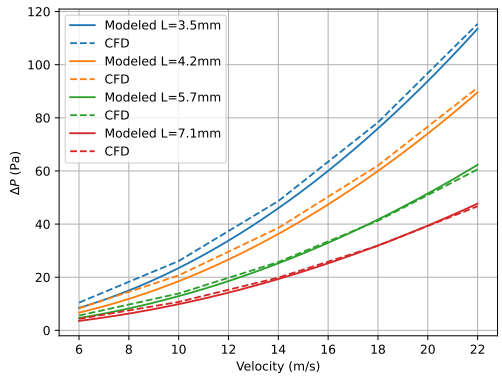

Figure 11.1: Predicted vs. actual static pressure curves for varying opening size

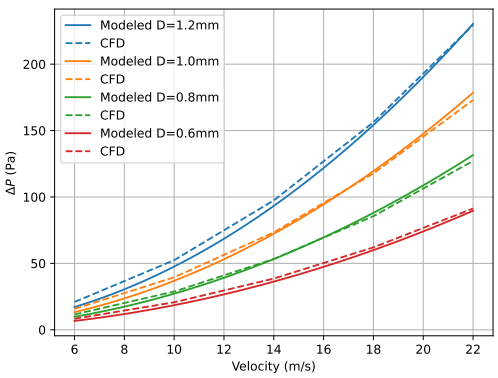

Figure 11.2: Predicted vs. actual static pressure curves for varying wire thickness

The prediction model was further evaluated by extending it to unit-cell geometries with different pattern shapes.

When predicting the static pressure curves for geometries sharing the same inscribed circumference (Figure 11.3), the model maintained a high level of accuracy. This behavior is expected, as these data were included in the coefficient fitting procedure.

A more stringent assessment of the model's robustness is provided by the predictions obtained when the longest diagonal of each unit-cell geometry is fixed (Figure 11.4). The corresponding data were not used during model calibration. Nevertheless, the predicted curves remain in close agreement with the numerical results, indicating that the proposed formulation is capable of accurately extrapolating across variations in pattern geometry.

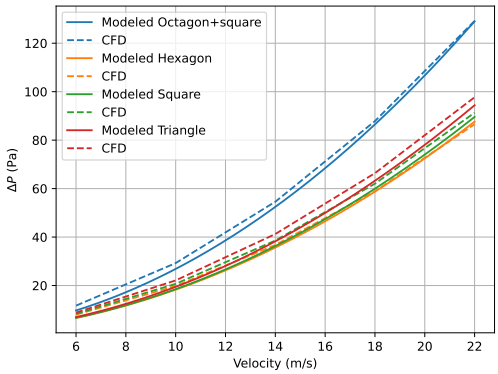

Figure 11.3: Predicted vs. actual static pressure curves for varying pattern shape, with the same inscribed circumference of diameter 4.2 mm.

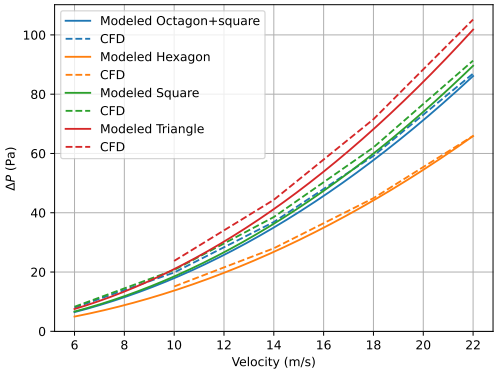

Figure 11.4: Predicted vs. actual static pressure curves for varying pattern shape, with the same longest diagonal of 6 mm.

A further assessment of the model's robustness is provided by the prediction of the pressure-drop curve for a grille composed of an octagon and a square sharing one side. As described in section 8.2, the shape factor S appearing in Equation 8.10 was derived exclusively from data corresponding to triangular, hexagonal, and square unit cells. This case constitutes a nontrivial validation of the model. The prediction involves not only the response of the octagonal geometry, which was not included in the derivation of the shape factor, but also the correct estimation of the relative contribution of the square. Since the overall pressure-drop curve is obtained as the superposition of the contributions from the two constituent geometries, the agreement with the numerical results demonstrates the model's ability to generalize to composite patterns composed of previously unseen shapes.

11.2. Grille Modeling: Porous Medium vs. Full Geometry

To check the accuracy of the developed model, a new square grille configuration was tested. The grille featured a side length of $6\mathrm{mm}$ and a wire diameter of $0.9\mathrm{mm}$ and was subjected to a freestream velocity of $16\mathrm{m\,s^{-1}}$. None of these parameters had been previously included in the dataset used for model calibration, ensuring that the assessment was free from bias related to the original fitting process. The results are shown in Table 11.1. Given the model over-predicts the numerical solution by under $2\mathrm{Pa}$, the model can be considered to be robust.

Case	CFD simulation	Model
ΔP_{grille}	49.13 Pa	50.97 Pa
Δ	-	+1.84 Pa
Δ	-	+3.8 %

Table 11.1: Comparison between the modeled and calculated pressure drop in CFD, from $20\mathrm{mm}$ upstream to $20\mathrm{mm}$ downstream of the grille.

One of the limitations of the porous medium approach is the inability to correctly simulate the effect of the misalignment between the flow and the fins used to dissipate the heat absorbed by the radiator from the coolant fluid by convection with the incoming air. Various motorsport applications make use of bent fins, aligned with the direction of the incoming flow; in such cases, modeling the physical radiator behaves more similarly to the one modeled numerically as a porous medium.

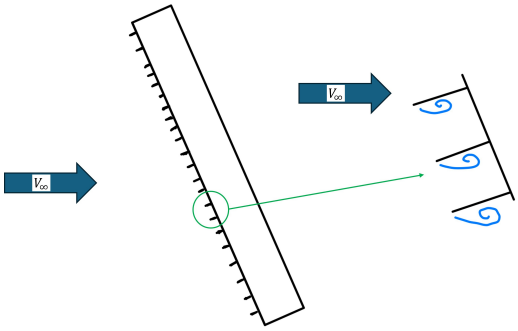

Figure 11.5: Flow behavior in the geometrically modeled radiator, when not aligned with the inlet face.

11.3. Effect of Volume Box Removal: Performance vs. Time Savings

The primary motivation for modeling the grille as a porous medium was to reduce the computational time and resources required to capture its aerodynamic impact. As a final step, it is therefore important to first check that the porous medium actually returns the same or similar pressure drop as the one predicted with Equation 8.10, To be able to judge whether the accuracy loss in the results can be justified by the reduced computational time and resources needed. The evaluation was done at 16 $\mathrm{m\,s^{-1}}$, employing the same grille geometry that was previously used to check the accuracy of the model in section 11.2.

The parametrization based on the Forchheimer equation (Equation 8.10) predicts a pressure drop of 50.97 Pa, which is 1.84 Pa higher than the value obtained from the simulation with the grille modeled explicitly (49.13 Pa). As shown in Table 11.2, the porous medium simulation using the finest volume refinement (minimum cell size of 1 mm) gives a pressure drop of 51.5 Pa, resulting in a deviation of about 0.6 Pa from the parametrized estimate. This confirms that the porous medium model, built from the coefficients extracted through the parametrization, reproduces the pressure loss of the fully resolved grille with good accuracy.

Parameter	**CFD Grille Modeled Geometrically**	**Porous Medium (smallest refinement 1 mm)**	**Porous Medium (smallest refinement 2 mm)**	**Porous Medium (smallest refinement 4 mm)**	**Porous Medium (smallest refinement 8 mm)**
ΔP_{grille}	49.13 Pa	51.55 Pa	51.65 Pa	51.55 Pa	51.72 Pa
Δ	-	+2.42 Pa	+2.52 Pa	+2.42 Pa	+2.59 Pa
Nr. volume cells [mln]	93.0	57.6 (-38.1%)	52.3 (-43.7%)	51.2 (-44.9%)	50.0 (-46.2%)
Simulation time	2:45:21	2:01:33 (-26.7%)	1:56:28 (-29.7%)	1:52:35 (-32.1%)	1:52:32 (-32.1%)

Table 11.2: Simulation time and result accuracy at varying the volume refinement.

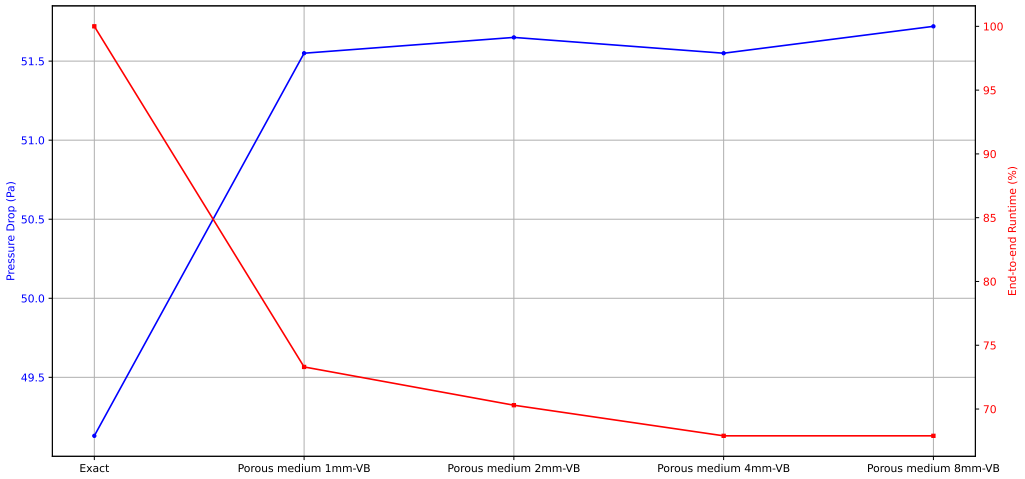

Figure 11.6: Simulation time and result accuracy at varying the volume box (VB) refinement.

As the outer volume refinement regions are removed, the total number of cells decreases and the computational time is reduced. Most cells, however, remain concentrated inside the smallest refinement region with a minimum cell size of 0.5 mm. For this reason, eliminating the coarser refinement boxes produces only a limited reduction in the overall cell count and therefore only a modest improvement in computational cost.
The accuracy of the results, does not seem to be every dependent on the volume mesh resolution around the porous medium. In part, this is because the flow in the CFD setup used is rather homogeneous, so the volume refinement does not have a big impact on the results. The small variations arise from differences in the cell-averaged velocity, which lead to slightly different local pressure drops and, consequently, to minor differences in their cumulative contribution.

Overall, the porous-medium representation reduces the end-to-end simulation time by approximately 30%, while the predicted pressure drop differs by just over 2 Pa compared to the explicitly modeled grille.

11.4. Grille+Radiator Modeling: Porous Medium vs Full Geometry

The grille modeling was tested in series with the radiator to check the accuracy of the whole model. The geometry of the tested grille was the same as in subsection 10.2.1, consisting of a square grille, with a side length of 4.2 mm, and a circular wire of diameter 0.6 mm. The assessment was carried out at an average freestream velocity of 22 $\mathrm{m\,s^{-1}}$ within the testing channel. The radiator was positioned 100 mm downstream of the grille. When the grille was represented as a porous medium, this distance was measured from the mid-plane of the porous block. Looking at Figure 11.7 and 11.8, the first noticeable difference between the grille modeled exactly and as a porous medium is the flow distribution upstream and downstream of the grille.

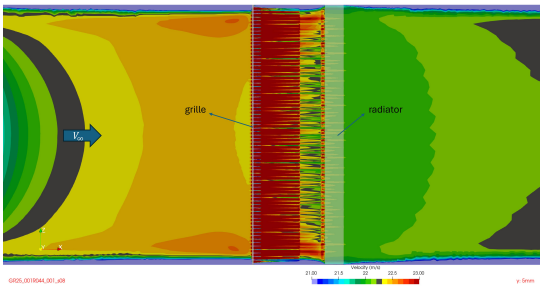

Figure 11.7: Velocity magnitude distribution across the grille modeled geometrically and the radiator modeled as a porous medium.

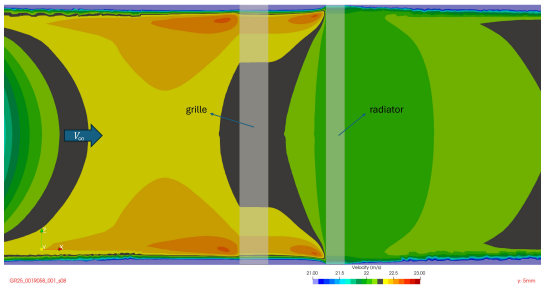

Figure 11.8: Velocity magnitude distribution across the grille and radiator, both modeled as porous media.

When the grille is modeled as a porous medium, the velocity at the core of the flow is slower compared to when the grille is modeled geometrically. As explained in section 2.5, the increased back-pressure present at the core, immediately upstream of the grille, generates streaks of higher velocity. In both cases, these seem to be similar in the vicinity of the walls. Downstream, the flow velocity profile is very different for the two cases, as when the wake is only present when the grille is modeled geometrically, with high velocities where the grille openings are located and very low velocities behind the struts.
Another interesting aspect to note is the modification of the boundary layer in correspondence with the two porous media. When the porous medium is a low porosity value (the radiator), the boundary layer gets ”reset”: the back-pressure cushion generated immediately upstream of the radiator acts as a favorable pressure gradient for the wall boundary layer, making it significantly thinner. Downstream of the porous medium, the boundary layer is free to grow back. In the case of the grille, which is highly porous, the back-pressure cushion effect is significantly reduced; hence, the thinning effect of the boundary layer is hardly noticeable.

Overall, the pressure loss predicted with the grille modeled as a porous medium is roughly 15 Pa (0.5%) higher than the simulation with the grille modeled geometrically, as shown in Table 11.3.

Grille Modeling	ΔP **Across Grille+Radiator**	**Difference**
Physically	2990.1 Pa	-
Porous medium	3005.2 Pa	+15.1 Pa (+0.5%)

Table 11.3: Pressure drop across the block grille+radiator, distanced 100mm apart.

The roughly 15 Pa increase in overall pressure drop all comes from an inaccuracy in predicting the pressure drop across the grille, as shown in Table 11.4. The difference is probably to be attributed to the very different flow velocity distribution upstream of the grille, which directly impacts the pressure losses registered locally.

Grille Modeling	ΔP **Across Grille**	ΔP **Across Radiator**
Physically	79.6 Pa	2910.5 Pa
Porous medium	94.9 Pa (+15.3 Pa)	2910.3 Pa (-0.2 Pa)

Table 11.4: Pressure drop across grille and radiator, distanced 100mm apart.

Given that the overall inaccuracy across the grille and radiator is limited to just 0.5%, and the pressure loss is conservatively over-predicted, providing a favorable safety margin, the grille can be confidently modeled in CFD with sufficient accuracy for motorsport applications.

12

Recommendations

This chapter serves as a collection of all the points that could not be addressed throughout the project, either due to time constraints or limited availability of resources.

One of the main points of improvement regards the experimental side of the research. All the different setups that were tested, especially when testing the grille alone, were unable to accurately measure the static pressure drop across the grille. The main issues encountered were the asymmetry in the readings, the limited repeatability, and the fact that the sensitivity of the pressure probes for this new test configuration had not yet been fully established.
The first and last points are likely related. Even when measuring the pressure drop across the grille, a slight increase compared to the empty tunnel test is observed, indicating that the probes do capture changes in pressure. However, the probes used have a resolution limit that is of the same order of magnitude as the pressure losses generated by the grille. Given the wide measurement range of the sensors, the apparent asymmetry observed in several readings can therefore be attributed to their limited resolution rather than to a physical effect.
The most straightforward way to address these two points, is to use high-resolution differential pressure transducer with a finer sensitivity, therefore able to measure the pressure more accurately. From the current results collected, it is hard to judge whether the issues seen are solely due to the instruments or whether there are other hidden issues.
All the considerations made here come from judgments based on the flow velocity profile observed in CFD, which appears uniform across the cross section of the test section when the grille is placed within the straight 900 mm duct setup, leaving no reason for justifying an asymmetry in the flow. Another useful test would be to measure the flow velocity profile in the test section, to double-check the correspondence with the numerical simulations. An attempt was made, using an omniprobe which allows for measuring both the flow velocity locally and its direction. The same instrument is regularly used in the wind tunnel, where a robotic arm ensures the probe remains fixed in space during data acquisition. Unfortunately, at the radiator test bench, no robotic arm or suitable fixture was available to hold the omniprobe steady in the flow, which prevented the verification of the flow velocity. Implementing such a setup in future tests would be highly beneficial.

The third point of improvement is the limited reproducibility of the tests. Each time a modification was made to the setup, the existing gaps between components (for example, between the converging duct and the wooden

plate where the grille or radiator was mounted) had to be manually re□taped. This inevitably introduced small variations between configurations. These gaps generated additional local losses of the same order of magnitude as the pressure differences being measured, thereby contributing to the variability observed in the results. The most significant influence on the results likely originated from the static pressure probes. To minimize any disturbance they could introduce, their position was altered as little as possible between consecutive setups. Their distance from the tested element was consistently targeted at 20 mm; however, because this measurement was performed manually, small positioning deviations may have occurred. Under normal operating conditions these deviations would be negligible, but in this case they become relevant because the pressure differences being measured were very small, making even minor variations in probe location comparatively significant. The probes should be oriented so that their tiny holes are perpendicular to the flow, ensuring they measure only the static component of the pressure. However, because the orientation was verified visually, it may not have been perfectly aligned in all cases. Some of the low-pressure differentials read could have been due to the hollow tubes not being tight enough, allowing for some air leakage. The use of smoke could also be implemented to easily visualize any air leakages that might be present.

Without a correlation study being performed, all the results obtained from the parametrization are solely based on the numerical results obtained. Although the exact offset from reality is unknown, the very fine volume mesh refinement and the y^+ value below one at the grille location suggest that any deviation from the experimental results should be minimal. When the smallest volume box size was reduced from 0.5 mm to 0.25 mm (Figure 6.22), the difference between the two simulations at 18 $\mathrm{m\,s^{-1}}$ was only 2.8 Pa, indicating a weak dependence on mesh refinement. Before confidently using the formulation derived from a real case scenario, this offset should be quantified.

One aspect that was not addressed in this study is the implementation of the setup within a full-vehicle aerodynamic simulation. The combined effect of the grille and radiator, both modeled as porous media, was only tested in the test bench setup, where these two are the only components present in the test section. Further investigation to validate the correct functioning of this approach in a complete car model should be done.

13

Conclusion

This research project aims to shed light on the parameters contributing to the static pressure drop across a protective grille in the context of motorsport applications. Little is known about the topic from the available literature, which mainly focuses on standard passenger vehicles, with very different performance requirements.
After having isolated the main drivers, understanding their relative impact on the aerodynamic efficiency of the grille allowed to parametrize the pressure drop, starting from its geometrical construction, and porosity. This step allowed to model the grille as a porous medium, in a more simplified and computationally cheaper way.
As a last step, the reciprocal effect the grille and radiator have on each other was analyzed, together with potential ideas on how to use the grille to deflect the flow towards the radiator, especially when inclined with respect to the incoming flow, enhancing its cooling efficiency and reducing the overall static pressure loss.

The main grille pressure drop drivers identified in order of importance are: the cross section of the wire, the geometrical shape, the opening size, the wire thickness, and lastly the passage length. The first two parameters have been considered to be the most influential ones, because they do not impact either the protective function of the grille or the structural resistance of the grille. The round wire resulted in almost half of the static pressure losses at $V_\infty = 22\ \mathrm{m\,s^{-1}}$ compared to the same grille with a square cross section, aided by the lack of sharp edges, allowing the flow to flow past the grille without abrupt separations.
Among all geometrical shapes tested at equal protection provided, the hexagon resulted in being the best performing one. The protective effect was studied both in a more conservative way, by setting the longest diagonal of the shape considered to be as wide as the debris size to be blocked, and by fixing the inscribed circumference, considering the debris as a spherical object. Although the latter case is less conservative, it allows for increasing the porosity of the grille, reducing the static pressure losses across the grille.
The opening size and wire thickness directly control the amount of duct cross-section blocked by the wire: a thinner wire and a wider opening size increase the porosity and decrease the static pressure drop. Halving the size of the square grille from 7.1 mm to 3.5 mm brought a 147% reduction in pressure drop, while doubling the wire diameter from 0.6 mm to 1.2 mm brought an increase of 151.4 %.
The last effect investigated was the passage length, which, although it leads to higher static pressure losses, could be used to deflect the flow towards the radiator, compensating, and even overcoming the losses at the grille level by the enhanced efficiency at the radiator level. Producing airfoil-shaped grilles is deemed to be expensive, so for most motorsport applications, the advantage brought in terms of performance is not sufficient to justify the

extra costs of production.

A model to derive the porosity coefficients required by the porous medium was developed, fully based on the geometrical parameters of the grille. The base used for the simulation was the square grille, as it was the easiest shape to mesh and simulate numerically. The formulation proposed by Calmidi [4] was used as the basis for the parametrization, as it is considered the most accurate for extrapolating results. By fitting only a subset of the data, this approach can reliably predict cases outside the original dataset. To account for different geometrical configurations, a multiplying factor called the shape factor (S) was developed from scratch, based entirely on geometrical considerations. The root mean square error of the predicted curves was consistently within 3 Pa of the numerical losses obtained simulating numerically the exact grille geometry. The grille modeled as a porous medium brought an end-to-end runtime reduction of about 30%.
The simulations of the grille modeled as a porous medium in series with a radiator confirmed the robustness of the research, showing high overall accuracy. The predicted static pressure loss differed by only 0.5% compared to the case where the grille was modeled geometrically.

As the radiator and grille are positioned closer together, the static pressure drop across both components decreases. Since the simulations were conducted under equal cooling performance conditions (with fixed mass flow flowing though the radiator), the configuration delivering the best performance was the one with the grille closest to the radiator. In this case, with the grille placed just 2.5 mm upstream of the radiator, the pressure drop across the radiator was reduced by nearly 100 Pa.
The overall pressure drop from upstream of the grille to downstream of the radiator resulted being independent of the distance between the two porous media.

References

[1] Ahmet Aydın et al. “Computational fluid dynamics analysis of a vehicle radiator using porous media approach”. In: *Heat Transfer Engineering* 42.11 (2021), pp. 904–916.

[2] WoD Baines et al. “An investigation of flow through screens”. In: *Transactions of the American Society of Mechanical Engineers* 73.5 (1951), pp. 467–477.

[3] Chiara Barontini. “Banco radiatori - Misura reti”. Slides presenting the performance loss of radiator protecting grilles. 2025.

[4] Varaprasad Venkata Calmidi. *Transport phenomena in high porosity fibrous metal foams*. University of Colorado at Boulder, 1998.

[5] Barbaros Çetin et al. “Computational modeling of vehicle radiators using porous medium approach”. In: *Des. Exp. Simul* 2.21 (2017), pp. 243–262.

[6] Emma Corfield et al. *A computational and experimental investigation into the effects of debris on an inverted double wing in ground effect*. Tech. rep. SAE Technical Paper, 2018.

[7] Prieur Du Plessis et al. “Pressure drop prediction for flow through high porosity metallic foams”. In: *Chemical Engineering Science* 49.21 (1994), pp. 3545–3553. ISSN: 0009-2509. DOI: https://doi.org/10.1016/0009-2509(94)00170-7. URL: https://www.sciencedirect.com/science/article/pii/0009250994001707.

[8] Nahid Dukhan. “Correlations for the pressure drop for flow through metal foam”. In: *Experiments in fluids* 41.4 (2006), pp. 665–672.

[9] Nihad Dukhan et al. “Air flow through compressed and uncompressed aluminum foam: measurements and correlations”. In: (2006).

[10] Sabri Ergun. “Fluid flow through packed columns”. In: *Chemical engineering progress* 48.2 (1952), p. 89.

[11] Iman Hansra. *Tech Explained | F1 Aerodynamic Cooling*. Accessed: 2025-06-09. Racecar Engineering. 2025. URL: https://www.racecar-engineering.com/tech-explained/f1-tech-explained/tech-explained-f1-aerodynamic-cooling/.

[12] Teddy Hobeika et al. “Experimental and numerical investigations of cooling drag”. In: *Proceedings of the Institution of Mechanical Engineers, Part D: Journal of Automobile Engineering* 231.9 (2017), pp. 1203–1210.

[13] SF Hoerner. “Fluid-dynamic drag: Theoretical”. In: *Experimental and Statistical Information* (1965).

[14] CT Hsieh et al. “3-D thermal-hydraulic analysis for airflow over a radiator and engine room”. In: *International journal of automotive technology* 8.5 (2007), pp. 659–666.

[15] Ali Abdul Jabbar Ibrahim et al. “CFD Analysis of the Thermal Performance of the Cooling System Car (Radiator) for Different Tube Arrangements”. In: (2025).

[16] Dastan Igali et al. “Comparative analysis of turbulence models for automotive aerodynamic simulation and design”. In: *International Journal of Automotive Technology* 20 (2019), pp. 1145–1152.

[17] J. M. Kim et al. “A numerical analysis study on the effect of grille shape on the aerodynamic performance of a small passenger vehicle”. In: *International Journal of Automotive Technology* 23.1 (2015), pp. 74–87.

[18] JM Kim et al. “Grille design for passenger car to improve aerodynamic and cooling performance using CFD technique”. In: *International Journal of Automotive Technology* 17 (2016), pp. 967–976.

[19] Taig Young Kim. “Analytical solution for laminar entrance flow in circular pipes”. In: *Journal of Fluid Mechanics* 979 (2024), A51.

[20] Doruk Koçal et al. “Experimental Investigation of Hybrid Nanofluid Use in Automobile Cooling System and the Effect of New Front Grille Design on Cooling Load”. In: *International Journal of Thermophysics* 45.11 (2024), p. 160.

[21] Takashi Kubokura et al. *Study of cooling drag reduction method by controlling cooling flow*. Tech. rep. SAE Technical Paper, 2014.

[22] J Gordon Leishman. *Introduction to aerospace flight vehicles*. Embry-Riddle Aeronautical University, 2023.

[23] Lin Li et al. “Unsteady effects of wake on downstream rotor at low Reynolds numbers”. In: *Energies* 15.18 (2022), p. 6692.

[24] Longwei Liu et al. “Numerical Simulation of the Influence of Intake Grille Shape on the Aerodynamic Performance of a Passenger Car”. In: *2015 International Power, Electronics and Materials Engineering Conference*. Atlantis Press. 2015, pp. 489–494.

[25] AO Mahgoub et al. *Numerical and experimental investigation of utilizing the porous media model for windbreaks CFD simulation, Sustain. Cities Soc.(2021)*. 2020.

[26] Isabel Malico et al. “Direct numerical simulation of the pressure drop through structured porous media”. In: *Defect and Diffusion Forum*. Vol. 364. Trans Tech Publ. 2015, pp. 192–200.

[27] NN Mansour et al. “Near-wall k-epsilon turbulence modeling”. In: *AIAA journal* 27.8 (1989), pp. 1068–1073.

[28] Pegasus Auto Racing Supplies. *Stainless Steel Wire Mesh for Radiator Protection*. Accessed: 2025-09-24. 2025. URL: https://www.pegasusautoracing.com/productselection.asp?Product=3641.

[29] Rajashekhar Pendyala et al. “CFD analysis of heat transfer performance in a car radiator with nanofluids as coolants”. In: (2015).

[30] Bo N. J. Persson et al. “The effect of surface roughness on the adhesion of elastic solids”. In: *Journal of Chemical Physics* 115 (2001), pp. 5597–5610. DOI: 10.1063/1.1398300.

[31] A.P. Petrov. “The role of the radiator grille in the organization of air supply to the engine cooling system”. In: (2016).

[32] *Pseudo Time Method Under-Relaxation*. Accessed: 2026-01-19. Ansys Inc. 2024. URL: https://ansyshelp.ansys.com/public/Views/Secured/corp/v242/en/flu_th/flu_th_sec_underrelax_pseudo.html.

[33] Miao Qi et al. “Influence analysis of front grille shape on flow field in front cabin of series hybrid electric truck based on large eddy simulation”. In: *International Journal of Vehicle Design* 92.2-4 (2023), pp. 403–416.

[34] JT Richardson et al. “Properties of ceramic foam catalyst supports: pressure drop”. In: *Applied Catalysis A: General* 204.1 (2000), pp. 19–32.

[35] Vinicius Maron Sauer. “Flow Development in the Entrance Region of Slender Converging Pipes”. In: *arXiv preprint arXiv:2510.05313* (2025).

[36] LC Thijs et al. “Honeycomb-generated Reynolds-number-dependent wake turbulence”. In: *Journal of Turbulence* 22.9 (2021), pp. 535–561.

[37] Jie Tian et al. “Experimental and numerical study on aerodynamic noise of outdoor unit of room air conditioner with different grilles”. In: *International journal of refrigeration* 32.5 (2009), pp. 1112–1122.

[38] A. Tiwari et al. “The effect of surface roughness and viscoelasticity on rubber adhesion.” In: *Soft matter* 13 19 (2017), pp. 3602–3621. DOI: 10.1039/c7sm00177k.

[39] Adnan Topuz et al. “Experimental investigation of pressure drop and cooling performance of an automobile radiator using Al 2 O 3-water+ ethylene glycol nanofluid”. In: *Heat and Mass Transfer* 56 (2020), pp. 2923–2937.

[40] Simon Tupin et al. “Assessing porous media permeability in non-darcy flow: a re-evaluation based on the forchheimer equation”. In: *Materials* 13.11 (2020), p. 2535.

[41] Dongwei Wang et al. “The effect of Reynolds number on the unsteady wake of a high-speed train”. In: *Journal of Wind Engineering and Industrial Aerodynamics* 204 (2020), p. 104223.

[42] Huizhu Yang et al. “Review and a theoretical approach on pressure drop correlations of flow through open-cell metal foam”. In: *Materials* 14.12 (2021), p. 3153.

[43] Xiaohu Yang et al. “An analytical model for permeability of isotropic porous media”. In: *Physics Letters A* 378.30-31 (2014), pp. 2308–2311.

[44] A. Yıldız et al. “Investigation of effect of vehicle grilles on aerodynamic energy loss and drag coefficient”. In: *Journal of Energy Systems* (2018). DOI: 10.30521/JES.461133.

[45] Chao Yu et al. “Comparative study on CFD turbulence models for the flow field in air cooled radiator”. In: *Processes* 8.12 (2020), p. 1687.

[46] Chunhui Zhang et al. “Full vehicle CFD investigations on the influence of front-end configuration on radiator performance and cooling drag”. In: *Applied Thermal Engineering* 130 (2018), pp. 1328–1340. ISSN: 1359-4311. DOI: https://doi.org/10.1016/j.applthermaleng.2017.11.086. URL: https://www.sciencedirect.com/science/article/pii/S1359431117352985.

[47] Chunhui Zhang et al. “Turbulence modeling effects on the CFD predictions of flow over a detailed full-scale sedan vehicle”. In: *Fluids* 4.3 (2019), p. 148.

[48] Tengfei Tim Zhang et al. “A simplified approach to describe complex diffusers in displacement ventilation for CFD simulations.” In: *Indoor air* 19.3 (2009).

[49] Yingchao Zhang et al. “Research on vehicle aerodynamics and thermal management based on 1D and 3D coupling simulation”. In: *Energies* 15.18 (2022), p. 6783.

[50] Runpu Zhao et al. “The influence of the gap on the air intake grille on the downforce of a car”. In: *Applied and Computational Engineering* 98 (2024), pp. 186–196.

[51] Sicheng Zhao et al. “A reduced radiator model for simplification of ONAN transformer CFD simulation”. In: *IEEE Transactions on Power Delivery* 37.5 (2022), pp. 4007–4018.